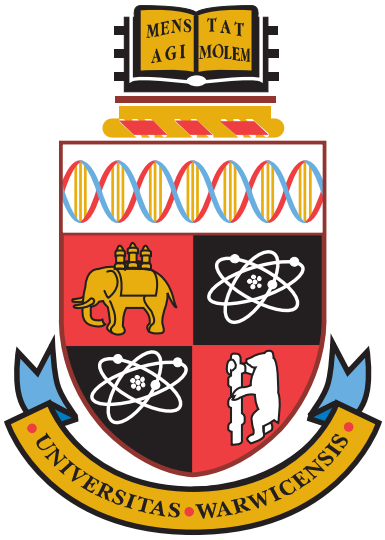

Structural Studies of Novel Bismuth containing Piezoelectric Ceramics

by

Kaustuv Datta

Thesis

Submitted to the University of Warwick

for the degree of

Doctor of Philosophy

Department of Physics

September 2010

THE UNIVERSITY OF WARWICK

Contents

List of Tables

List of Figures

Acknowledgments

First of all, I am truly grateful to my vibrant supervisor Pam Thomas who has been tremendously cooperative during the last three and a half years. I have been extremely lucky to be a part of her group. During my time at Warwick I have received plenty of help and fantastic company which I will not be able to forget. It is very difficult for me to name each and every person at this moment, and in fact a PhD student in the department is practically associated with the whole bunch of people who work there. However, it is obvious that group members come first: Dan Baker, Iain Dunn, Steven Hubard, Semen Gorfman, Aoife O'Brien, Dean Keeble, David Walker and David Woodward. In particular, David Walker is the person who took care of me from the very beginning and he never waited to be asked for help. Also, I enjoyed his company on several occasions including an international conference in Rome. During my 3rd year of the course, Sem joined the group and he contributed a lot towards my understanding of the study of single crystals. I am truly grateful to him for his time and his enthusiasm to discuss results with me. Bonus thanks to David Woodward for going through my thesis and providing a detailed feedback.

It is my great pleasure to know Prof Krystian Roleder from University of Silesia and I am thankful to him for the very useful discussions on the dielectric experiments.

I am grateful to my fellow office mates from the Glass group, particularly, a young talented fellow named Meng, who offered his expertise in drawing and brilliantly drew some of the diagrams presented in this thesis.

Let me take this opportunity to acknowledge some of my other friends; Alberto, Ben, Paul, Prof. Eduard Vives and my house-mates Dan and William for their pleasant company on different occasions.

I must mention the huge encouragement I received from my family on a regular basis, which has been a constant source of energy for me. Without their emotional support I could not imagine writing this thesis.

Finally, Haimantee, for your enormous patience, constant support and endless love during these years.

Declaration and published work

I declare that the work presented in this thesis is my own except where stated otherwise, and was carried out entirely at the University of Warwick, during the period of December 2006 to March 2010, under the supervision of Prof. P. A. Thomas. The research reported here has not been submitted, either wholly or in part, in this or any other academic institution for admission to a higher degree.

Some parts of the work reported and other work not reported in this thesis have been published or submitted for publication, as listed below. It is anticipated that further parts of this work will be submitted for publication in due course.

[1] K. Datta, K. Roleder and P. A. Thomas, "Enhanced tetragonality in lead-free piezoelectric (1-x)$BaTiO_3$−x$Na_{1/2}Bi_{1/2}TiO_3$ solid solutions where x=0.05 to 0.40.", *J. Appl. Phys.* **106**, (2009), 123512.

[2] K.Datta, S. Gorfman and P. A. Thomas, "On the symmetry of the morphotropic phase boundary in ferroelectric $BiScO_3$−$PbTiO_3$ system.", *Appl. Phys. Lett.* **95**, (2009), 251901.

[3] K. Datta and P. A. Thomas, "Structural Investigation of a novel perovskite-based lead-free ceramics: $x$$BiScO_3$-(1-$x$)$BaTiO_3$", *J. Appl. Phys.* **107**, (2010), 043516.

[4] K.Datta, E. Suard and P. A. Thomas, "Compositionally driven ferroelectric phase transition in x$BiInO_3$-(1-x)$BaTiO_3$: a lead-free perovskite-based piezoelectric material", *Appl. Phys. Lett.* **96**, (2010), 221902.

[5] K. Datta, D. Walker and P. A. Thomas, "Structural properties of solid solutions of bismuth scandate-lead titanate.", *Accepted for publication in Phys. Rev. B* .

Kaustuv Datta

August 2010

Abstract

Perovskite-based materials are in the focus of research not only because of their excellent physical properties, but also because their relatively simple structure facilitates the understanding of structure-property relationships, which is crucial for developing novel materials with improved qualities. Recent research in the field of ferroelectric and piezoelectric materials is concerned with the development of eco-friendly lead-free materials. To achieve this goal, it is important to understand the fundamental correlation between the 'Structure' and the 'Property'. In this work, the primary focus has been to elucidate the structural changes occurring as a function of doping in three different systems: (1) $BiScO_3$–$PbTiO_3$ (BS-PT), a recently developed system which has already attracted much interest because of its superior physical properties near the morphotropic phase boundary (MPB); (2) $BiScO_3$–$BaTiO_3$ (BS-BT), which can be considered as a lead-free analogue of the BS-PT family and lastly, (3) $Na_{0.5}Bi_{0.5}TiO_3$–$BaTiO_3$ (NBT-BT), which is a well-known lead-free material at the NBT-rich side of the phase diagram.

Powder samples with a range of compositions for each system were prepared following the solid-state synthesis route and were investigated utilizing both neutron and x-ray powder diffraction and dielectric measurements. Detailed crystallographic information was obtained by Rietveld refinement against the neutron powder diffraction data. Structural phase transitions as a function of temperature were determined by non-ambient x-ray powder diffraction and compared with the physical properties of the ceramics using high-temperature dielectric measurements. The significant outcomes are :

1. The best model to represent the so-called MPB of xBS-(1-x)PT system is found to be a mixture of a tetragonal and a monoclinic phases from the powder diffraction data. The structure beyond the MPB compositions is in better agreement for a single monoclinic model with the space group Cm than the accepted space group $R3m$. By contrast, single crystals with compositions around the MPB provide evidence for a model consisting of two primitive monoclinic cells.

2. The lead-free BS-BT system exhibits an extended phase boundary between tetragonal and pseudocubic phases, which can be modelled by a combination of tetragonal and rhombohedral phases. The incorporation of BS into BT also results in the suppression of the two low-temperature phase transitions of BT.

3. Samples with new compositions synthesized in the xNBT-(1-x)BT system demonstrate a rare enhancement in the tetragonality of the unit cell and an increase in the Curie temperature for compositions where $x \leq 0.40$.

Chapter 1

Introduction

1.1 Piezoelectricity and crystal symmetry

Piezoelectricity is a phenomenon that was discovered by Jacques Curie and Pierre Curie in 1880. The term refers to the generation of an electric moment in response to mechanical stress and vice versa. Mathematically, it can be written as

$$P_i = d_{ijk}\,\sigma_{jk} \tag{1-1}$$

$$\epsilon_{ij} = d_{ijk}\,E_k \tag{1-2}$$

Equation (1-1) describes direct piezoelectricity, where P gives the magnitude of the electric moment per unit volume or polarization charge per unit area, σ is the applied stress and d is called the piezoelectric constant. Equation (1-2) refers to reverse piezoelectricity, where ϵ is the induced strain in response to the external electric field E.

The class of materials that exhibit such properties are called piezoeletric materials and because of their unique ability to couple electrical and mechanical displacements they are widely used as sensors and actuators. The structure and symmetry of a material plays a decisive role in piezoelectricity. The necessary crystallographic requirement for a material to show piezoelectricity is that it should not have a center of symmetry. As shown in fig 1-1, of the 32 crystallographic point groups, only 21 are non-centrosymmetric and can demonstrate piezoelectricity (the exception being the 432 point group). Examples of materials having non-centrosymmetric structures and used in many piezoelectric devices include aluminum nitride and quartz.

In many piezoelectric materials, however, a spontaneous polarization exists as a result of a separation between positive and negative charge centers in the crystallographic unit cell. A typical example of a structure which exhibits a spontaneous polarization is the perovskite structure of $BaTiO_3$ (description is given in the following section). If the spontaneous polarization is reversible by an external electric field then the material

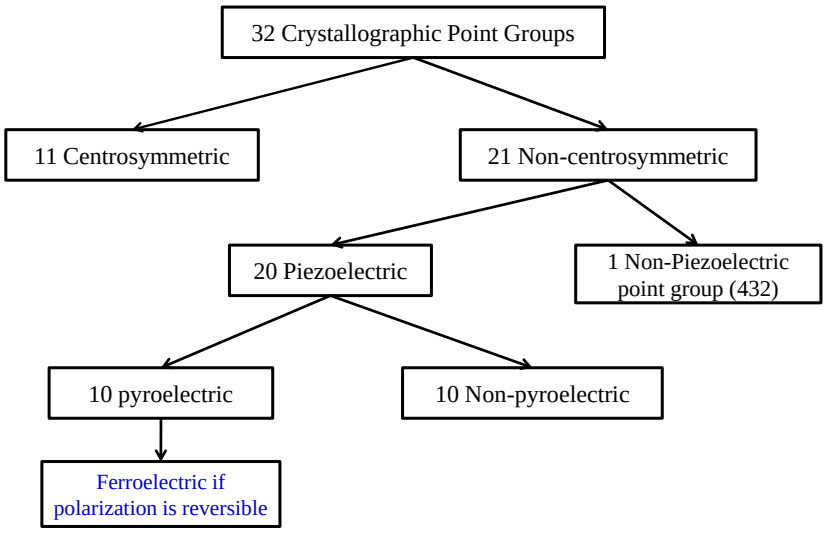

Figure 1-1 Symmetry hierarchy for piezoelectricity.

is called ferroelectric. 10 out of 21 non-centrosymmetric point groups, known as polar groups, can show a spontaneous polarization and can potentially demonstrate ferroelectricity. Ferroelectric materials are commonly characterized by polarization hysteresis under external electric field (fig 1-2). The hysteresis disappears beyond a certain temperature, which is known as the Curie temperature (T_c). This involves a structural phase transition from a polar to a non-polar structure. Ferroelectric materials are used for a large number of applications including high-permittivity capacitors, memory devices and electric-optic devices. Another important phenomenon which is related to the polar crystal group is pyroelectricity. This refers to the temperature dependence of the spontaneous polarization (fig 1-3). All ferroelectric crystals are pyroelectric but not all pyroelectrics show ferroelectricity.

Piezoelectric materials can be used as single crystals or polycrystalline ceramics and the materials are characterized by the following parameters :

1. Piezoelectric constant (d).

2. Piezolectric voltage constant g : If the induced electric field is E, in response to an external stress X, then E = g X.

3. Electromechanical coupling factor k : k^2 = (Stored mechanical energy/ Input electrical energy) or (Stored electrical energy/ Input mechanical energy).

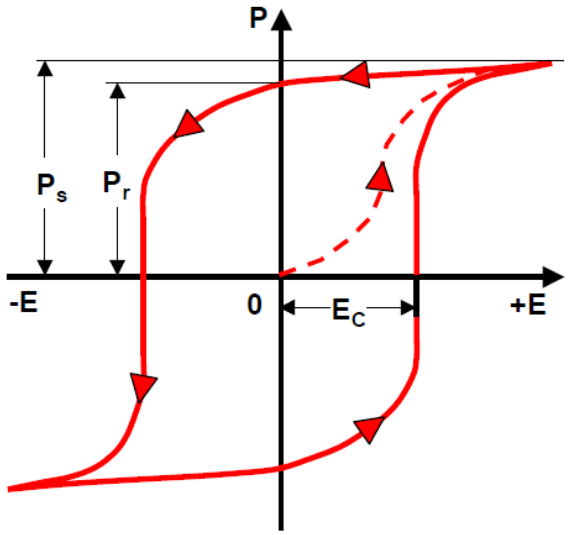

Figure 1-2 Schematic diagram of a typical ferroelectric hysteresis loop. P_s refers to the saturation polarization, P_r is the remanent polarization which is the value of the polarization at zero field and E_c is the coercive field which is defined as the required field to bring the polarization to zero.

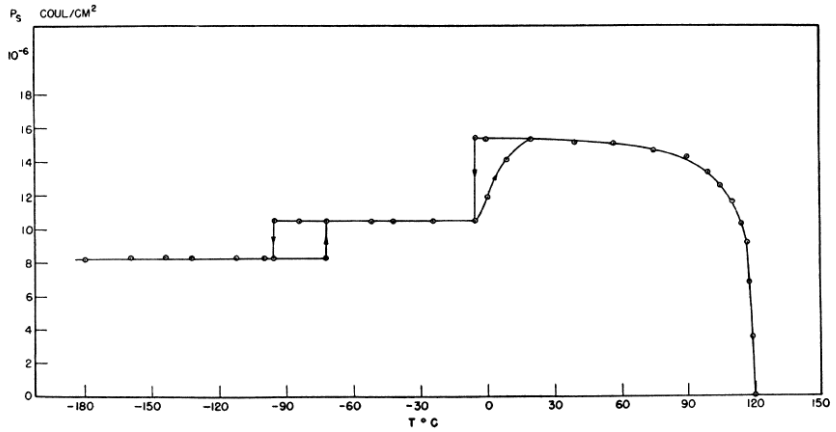

Figure 1-3 Spontaneous polarization (P_s) of $BaTiO_3$, measured along the [100] direction as a function of temperature [1].

Table 1-1 Physical properties of major piezoelectric materials together with their symmetries. The data are taken from the book by K. Uchino [2]

Parameter	Quartz	BaTiO3	PbTiO3 : Sm	PZT 5H	LF4T	PZN - 8%PT [001]
Symmetry	32	4mm	4mm	3m/4mm	mm2/4mm	3m/4mm
d_{33}(pC/N)	2.3	190	65	593	410	2500
d_{31}(pC/N)	0.09	0.38	0	-274	-154	-1400
ε_T^{33}	5	1700	175	3400	2300	7000
T_c(°C)		120	355	193	253	160

4. Mechanical quality factor Q_M : This defines the sharpness of the electromechanical resonance spectrum.

These parameters are also known as piezoelectric figures of merit. Other important parameters are the complex permittivity ($\varepsilon = \varepsilon' + i\varepsilon''$) and loss tangent. The real part is related to how much electrical potential energy can be stored in a given volume of the material under the influence of an electric field and the imaginary part refers to the energy loss. The loss tangent is defined as ($\varepsilon''/\varepsilon'$). Physically it can be defined as (energy loss / energy stored) per cycle and provides a parameter to quantify the lossy materials. Table 1-1 provides the values of piezoelectric figures of merit for a few common piezoelectric systems.

1.2 An introduction to the Perovskite structure

1.2.1 Prototype cubic perovskite

The term 'perovskite' refers to a large family of crystals with structures based on that of the mineral $CaTiO_3$, which is known as perovskite. This was named after the Russian minerologist Count Lev Aleksevich von Perovski (1792-1856). The structure, represented as ABX_3, consists of corner-linked octahedra of X anions with B cations at their centers and A cations in the interstices formed by the anion octahedra (fig 1-4). In general, 'A' has 12-fold cuboctahedral coordination with the anions whereas 'B' is octahedrally coordinated by the X anions. The choices of A & B are very broad. Examples of common A-site cations are: Ca^{+2}, Sr^{+2}, Na^{+}, K^{+}, Pb^{+2}, Ba^{+2}, La^{+3} and Bi^{+3}; examples of common B-site cations are : Zr^{+2}, Mg^{+2}, Zn^{+2}, Sc^{+3}, Fe^{+3}, Ti^{+4}, Ta^{+5} and Nb^{+5} and X is typically either an oxygen or a fluorine ion.

Not all compounds with the formula ABX_3 have a perovskite structure. According

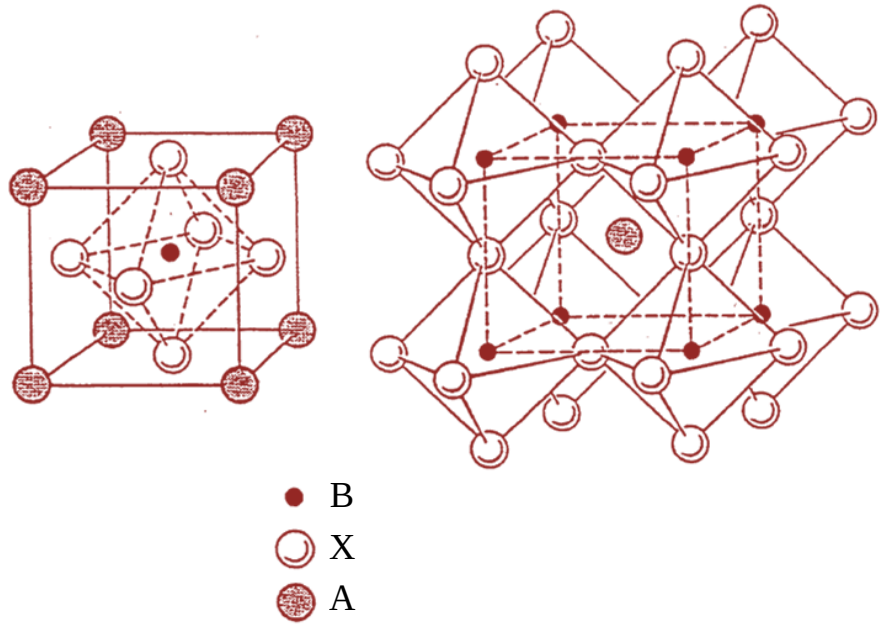

Figure 1-4 Schematic view of the cubic prototype perovskite-type structure with the formula ABX_3. The space group is $Pm\bar{3}m$ with lattice constant ~ 4 Å, however, in the case of a mixed B-cation site with cation ordering, a doubling of the unit cell occurs and the space group becomes $Fm\bar{3}m$.

to Goldschmidt (1926), the geometrical requirement for the formation of the perovskite structure is that the ionic radii r_A, r_B and r_X of the A,B and the X ions must satisfy the following relationship:

$$t = (r_A + r_X)/\sqrt{2}(r_B + r_X) \tag{1-3}$$

where 't' is called the tolerance factor. The relationship phenomenologically describes the range of relative sizes of A and B cations for which the perovskite structure is stable. A perovskite structure is said to be stable if 't' lies in the range $0.80 < t < 1.1$. It has been seen that $t > 1.0$ normally favors tetragonal distortions whereas $t < 1.0$ favors orthorhombic or monoclinic symmetries . The ideal perovskite structure ($t = 1.0$) is cubic with the space group $Pm\bar{3}m$. $SrTiO_3$ is an example of material having a cubic perovskite structure at room temperature.

1.2.2 Structural variations in perovskite

The flexibility of the perovskite structure given by the geometric condition of ionic radii allows a number of variations in the structure through small distortions of the unit cell or displacements of the atoms. As a result of these variations, many structural phase transitions occur either because of doping or changes in the physical conditions (temperature, pressure, electric field). In the case of a complex perovskite where the A- and B-site are occupied by more than one element, 't' can be estimated by replacing r_A and r_B by $\bar{r_A}$ and $\bar{r_B}$, respectively:

$$\bar{r_A} = \sum_{i=1}^{m} x_{A_i} r_{A_i} \tag{1-4}$$

$$\bar{r_B} = \sum_{i=1}^{m} x_{B_i} r_{B_i} \tag{1-5}$$

where x_{A_i} is the proportion of the A_i^{th} element. Since r_O remains unchanged, the following conditions have been found experimentally in practice [3]:

$$\begin{aligned} \bar{r_A} &\geq 0.90 \times 10^{-10} m \\ 0.51 \times 10^{-10} m < \bar{r_B} &< 1.1 \times 10^{-10} m \\ \bar{r_A} &\geq \bar{r_B}. \end{aligned} \tag{1-6}$$

The modifications or deformations in the perovskite structure occur mainly through the combination of the following effects :

1. Displacements (parallel or anti-parallel) of cations from their high-symmetry positions within the polyhedra (fig 1-5);

2. Rotation or tilting of the octahedra (fig 1-6);

3. Ordering of the cations in the case of complex perovskites.

Although structural changes in perovskites can be subtle, their influence on the physical properties of the system are frequently significant. It is because of the large number of structural variants that perovskites exhibit many interesting properties such as colossal magneto-resistance, ferroelectricity, superconductivity, charge ordering and spin-dependent transport. There are several reports available that provide the details of

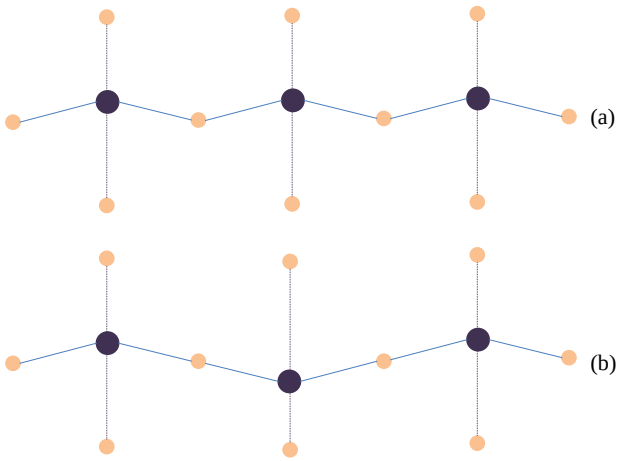

Figure 1-5 (a) Parallel and (b) anti-parallel displacement of cations. Parallel displacements correspond to ferroelectric behaviour whereas anti-parallel displacements correspond to anti-ferroelectric behaviour.

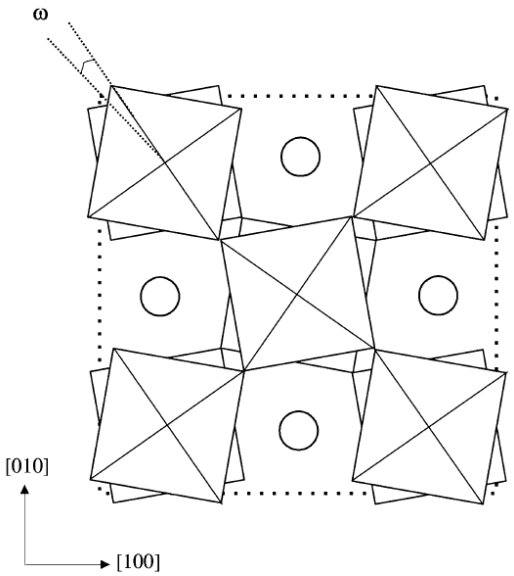

Figure 1-6 Example of octahedral tilting in perovskite structure. This figure is taken from the article by Jones and Thomas [4] and shows the projection of the rhombohedral structure of NBT down [001], open circles represent Na/Bi sites.

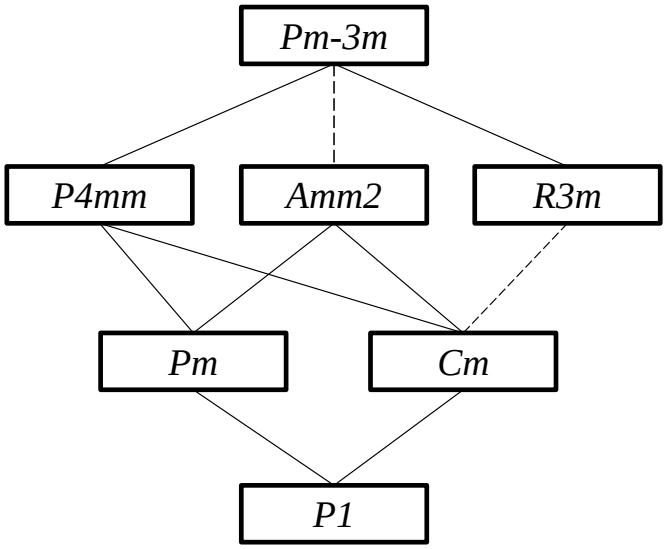

Figure 1-7 A schematic diagram showing the group-subgroup relationships for perovskites with B-site cation displacements without octahedral tilts. The dashed line indicates that, according to Landau theory, the corresponding phase transition cannot be continuous [10].

the structural variations seen in perovskites and their mutual relationships. For example, Thomas [5, 6] provided a scheme to classify the perovskite systems based on the polyhedral volume of A and B cations. Magaw and Darlington [7] published a comprehensive description of the distortions and tilts that occur in rhombohedral perovskites and Glazer [8, 9] first reported the details of the majority of the possible octahedral tilts in perovskites and their crystallographic representations. Recently Howard [10] published the crystallographic relations among the various structure changes occuring in the perovskites by applying group-theoretical methods. Figure 1-7 shows the group-sub group relationships for phase transitions in ferroelectric perovskites where phase transitions involve only displacements of the B-site cation.

1.3 Current status of piezoeletric materials

1.3.1 Open issues

Over the past couple of decades there has been a major advancement in the research and development of potential piezoelectrics because of the development of Microelectrome-

chanical systems (MEMS), which are the heart of next-generation ultra-high speed performance devices. However, the electromechanical industry is facing some fundamental challenges to the advancement of its technologies because of the limitations of the core materials employed. Applications across a great range of user areas require future devices with significantly reduced size and power consumption, ultra-high speed, and high levels of functionality. To meet these challenges, we need to develop novel materials with improved qualities. For example, the general requirements for fast ferroelectric DRAM capacitor thin films are high dielectric constant, low leakage current, micro-machinability, low diffusion into the semiconductor substrate and low contamination during the fabrication process; whereas, for piezoelectric sensors/actuators high piezoelectric response with a low temperature dependence is necessary. For the past few decades the solid solution $PbZrO_3$–$PbTiO_3$, commonly known as PZT, has dominated commercially because of its superior dielectric and piezoelectric properties. In particular, its large piezoelectric response has made PZT one of the most widely used materials for electromechanical applications. However, PZT is becoming increasingly unacceptable because of global concerns regarding its toxicity as it contains more than 60 weight per cent of lead. The use of volatile starting materials (PbO or Pb_3O_4) during processing causes an accumulation of lead in the environment. Very low concentrations of lead or lead derivatives can cause serious hazards to the brain, nervous system, kidney and blood. Therefore, the European Union (EU) in 2003 included PZT in its legislature to be substituted by lead-free materials [11, 12]. Apart from this, PZT also suffers from limited temperature range of applicability (highest Curie temperature $\sim$ 350 °C), low elastic moduli and the so-called fatigue problem (degradation of response with increasing hysteresis cycles), all of which restrict its overall usefulness. Therefore an extensive search for potential alternatives to PZT is on-going.

Piezoelectric materials with the perovskite structure have attracted much interest for a number of reasons. This particular class of materials has been the focus of current research because its simple basic crystal structure facilitates in understanding the interplay between structural changes and physical properties. In addition, perovskite-based piezoelectric materials are frequently ferroelectric which ensures efficient electromechanical transformation of energy and signal with high piezoelectric effect. Most importantly, unlike other crystal structures, perovskites do not have a close-packed oxygen

framework, and this provides great flexibility for chemical substitution. As a result of the variable chemical compositions and crystal symmetries, many physical properties can be tailored according to the specific needs of the various applications [13, 14].

1.3.2 Lead-based materials and Morphotropic Phase boundary (MPB)

The discovery of lead zirconium titanate $Pb(Zr_{1-x}Ti_x)O_3$ (PZT) solid solutions by Jaffe et al. [15] is considered to be a major breakthrough on the research of piezoelectrics. This finding initiated rapid developments and led to an enormous field of applications based on piezoelectrics. Nowadays, PZT is the most widely used material. The first room-temperature phase diagram of this system was published by Sawaguchi [16] which revealed the compositionally-driven structural transformation from the tetragonal (T) to the rhombohedral (R) phase at around $x = 0.47$. This work was soon followed by the discovery of a large piezoelectric response in compositions close to this phase boundary by Jaffe et al. [15]. An updated phase-diagram as a function of composition and temperature of the system was published and the phase boundary between tetragonal and rhombohedral phases was named as the 'morphotropic phase boundary' or MPB. The term 'morphotropic' refers to the boundary between two forms. In this context, the MPB represents a crossover from one crystal system to a different crystal system driven by the composition but nearly temperature-independent.

The most important modification of Jaffe et al.'s phase diagram came from Noheda et al. [19] who discovered a monoclinic phase intervening between the rhombohedral and tetragonal phases around the MPB (fig 1-8b). This also provided a new explanation of the origin of the enhanced physical properties of PZT at the morpohotropic phase boundary, i.e. the monoclinic phase has more degrees of freedom for polarization (the polarization vector can lie anywhere in the (101) plane, unlike in the T or R phase where it is confined to a particular crystallographic direction) to respond according to the applied electric field and in consequence, a maximum piezoelectric response around the MPB composition is observed. Since Noheda's work in 1999 the topic of the MPB in PZT has gained interest and there are different opinions about its nature. For example, some workers [20] claim that the monoclinic phase extends much further into the rhombohedral side of the phase diagram than previously believed, whereas others [21] have ascribed the apparently monoclinic symmetry to the effect of nano-twinning

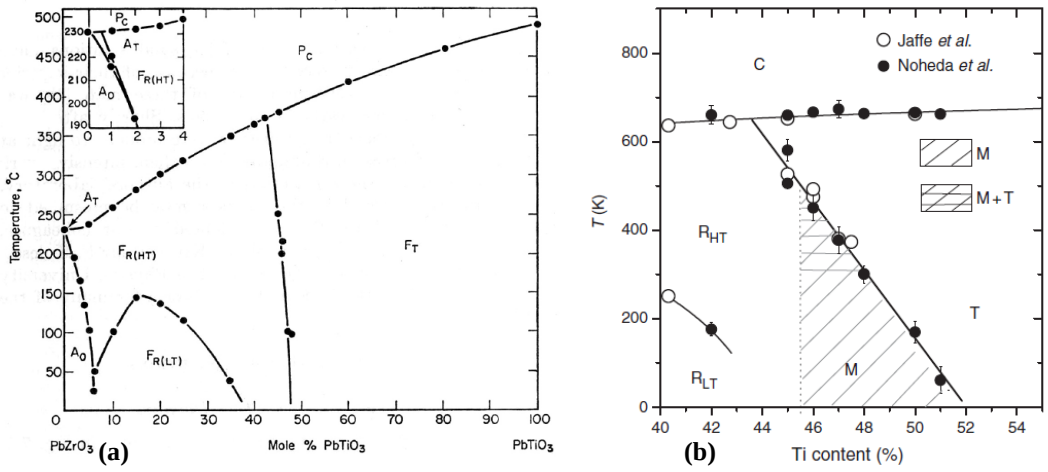

Figure 1-8 (a). The first detailed phase diagram of PZT published by Jaffe et al. [17]. (b). The phase diagram of PZT near the MPB published by Noheda et al. [18]. M refers to the monoclinic phase, whereas T, R and C refer to the tetragonal, rhombohedral and cubic phases, respectively.

and complex domain formations. It has also been suggested that either tetragonal or rhombohedral phases can be considered as a monoclinic on a suitably small length scale (at the local level) and there need not be any distinct phase boundaries across the MPB [22]. A review of the structural investigations carried out on PZT can be found in a recent article by Frantti [23].

Regardless of whether it is a true crystallographic phase of monoclinic symmetry or a nano-twinned tetragonal phase that mimics a monoclinic diffraction pattern, it is now well established that, near the MPB, PZT demonstrates enhanced physical properties. In general, at the boundary some of the elastic stiffness constants become very small and as a result, piezoelectric systems exhibit large strains in response to an external electric field and vice versa. Figure 1-9 shows the values of some piezoelectric parameters such as d_{33}, k_p and ε_{33}^T as a function of composition and it is evident that the physical properties are remarkably enhanced around the MPB.

It is important to note that a small amount of doping in PZT can cause significant changes to the structure and properties of the system. Therefore, it is possible to tailor the physical properties of the ceramic according to the need of specific applications by adding different dopants. Depending on the nature of the doping, the PZT ceramics are broadly classified as 'soft PZT' and 'hard PZT'. In the case of soft PZT, substitutions (for example, Nb^{+5} on B-site or La^{+3} on A-site) produce A-site vacancies which lead

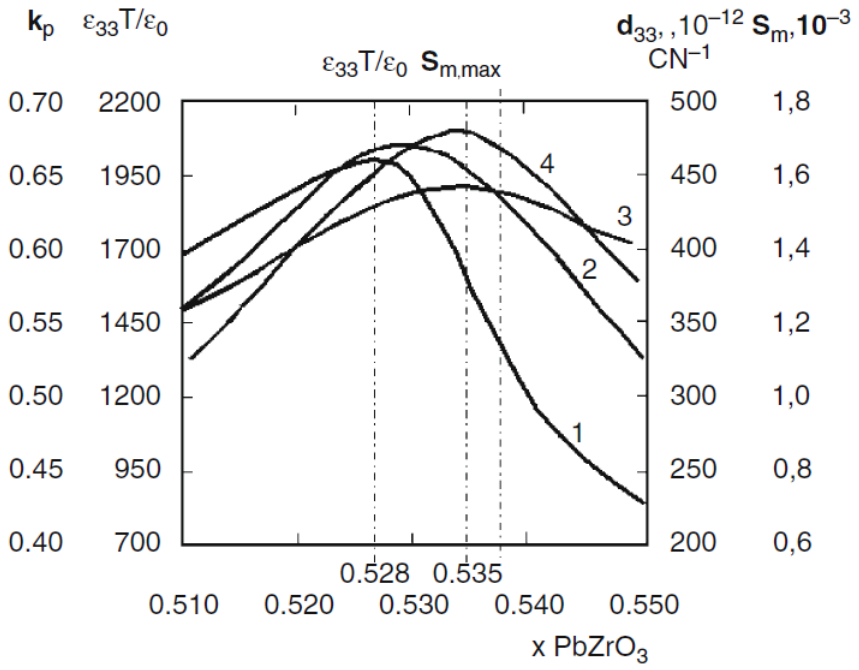

Figure 1-9 Comparison of the (1) dielectric permittivity ε_{33}^T, (2) the piezoelectric coefficient d_{33}, (3) the electromechanical coupling coefficient k_p, and (4) the large signal unidirectional strain S_m for poled PZT ceramics as a function of composition close to the MPB around $x_{PbZrO_3} = 0.53$ [24].

Table 1-2 Properties of modified PZT ceramics by donor and acceptor ions [24].

	Dopant	T_c (°C)	$\varepsilon_{33}^T/\varepsilon_0$	tanδ, 10^{-3}	k_p	d_{33} pC/N	Q_m
	soft						
(1)	Nb^{5+}	365	1700	15	0.60	374	85
(2)	Sb^{5+}	>350	1510	15	0.46	410	95
(3)	Nd^{3+}	330	1600	20	0.60	355	100
	hard						
(4)	Fe^{3+}	300	820	4	0.59	240	500
(5)	Ni^{3+}	330	1000	8	0.50	200	350

(1)$Pb_{0.98}Nb_{0.02}(Zr_{0.52}Ti_{0.48})O_3$
(2)$Pb_{0.95}Sr_{0.05}(Zr_{0.52}Ti_{0.46}Sb_{0.02})O_3$
(3)$Pb_{0.97}Nd_{0.03}(Zr_{0.54}Ti_{0.46})O_3$
(4)$Pb(Zr_{0.525}Ti_{0.472}Fe_{0.003})O_3$
(5)$Pb_{0.95}Sr_{0.05}(Zr_{0.52}Ti_{0.44}Ni_{0.04})O_3$

to materials with improved resistivity and higher piezoelectric coefficients but higher losses and lower mechanical quality factor. Whereas in hard PZT, substitutions such as, Fe^{+3} on B-site or K^+ on the A-site produce oxygen vacancies and lead to materials with a lower permittivity, lower dielectric loss, lower resistivity and higher mechanical quality factor.

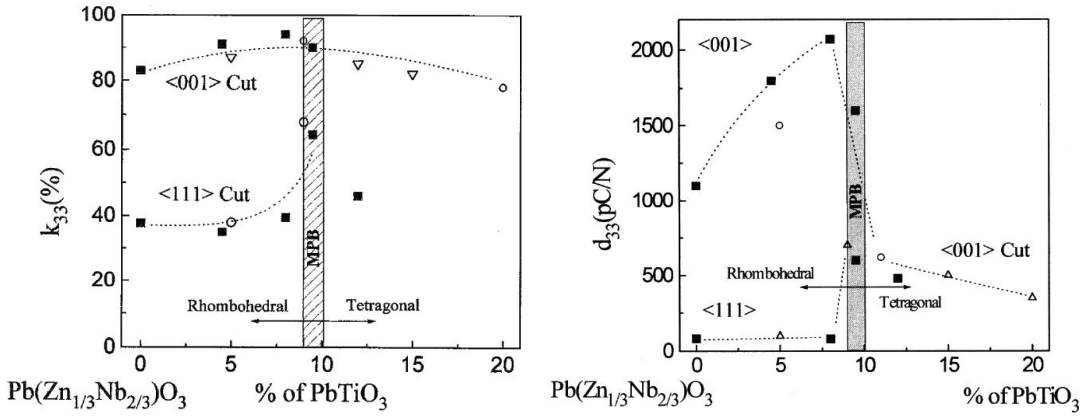

Figure 1-10 Electromechanical coupling factor (k_{33}) and piezoeletric strain constant (d_{33}) for PZN-PT system as a function of composition [25, 26].

Following the development of PZT, many other lead-based systems with general formula $Pb(B'B'')O_3-PbTiO_3$ have been investigated and found to be attractive candidates for industrial use [27]. A few important examples are (1-x)$Pb(Zn_{1/3}Nb_{2/3})O_3$-$x$$PbTiO_3$ (PZN-PT) [28], (1-x)$Pb(Mg_{1/3}Nb_{2/3})O_3$-$x$$PbTiO_3$ (PMN-PT) [29, 30], (1-x)$Pb(Sc_{1/2}Nb_{1/2})O_3$ -$x$$PbTiO_3$ (PSN-PT) [31]. These systems were found to have phase boundaries and the physical properties (permittivity, electromechanical coupling and piezoelectric coefficients) are exceptionally enhanced at compositions close to the MPB (fig 1-10). For example, at a particular composition and crystal orientation, the piezoelectric coefficient can reach 2500 pC/N and the thickness coupling coefficient 97% for single crystals [32]. The MPB in PZN-PT was reported at approximately 9−10% PT and at about 35% PT in PMN-PT.

1.3.3 Reduced-lead materials

In 2001, Eitel et al. [33] suggested a correlation between the tolerance factor and the Curie temperatures for PT-based solid solutions with a perovskite structure. Figure 1-11 shows the full list of the proposed systems, including three novel Bi-containing compounds: $BiScO_3$, $BiInO_3$, $BiYbO_3$. Among these three systems, the solid solutions of $BiScO_3$-$PbTiO_3$ were first verified as an attractive piezoeletric series with the potential to replace PZT or PZT-based materials for high-temperature applications. Comprehensive details of the investigations of this particular system are given in the 3rd chapter of

this thesis. The solid solution of xBiInO$_3$-(1-x)PbTiO$_3$ (BI-PT) was later developed and characterized by Duan et al. [34] and Zhang et al. [35]. The material demonstrated a highly distorted perovskite structure with a high Curie temperature between 580-590 °C depending on the composition(x). However, a solubility limit of BI in PT was found from the x-ray diffraction results, which was approximately x = 0.25. Recently, attempts have been made to produce solid solutions of xBiYbO$_3$-(1-x)PbTiO$_3$ under ambient pressure [36]. It was found that, it is difficult to form a single phase material even with a low concentration of BiYbO$_3$ (x = 0.05). The samples always contained some pyrochlore phases, such as Yb$_2$Ti$_2$O$_7$, which degraded the physical properties. From dielectric measurements, high Curie temperatures (~ 500 - 550 °C) were noted for ceramics with compositions between x = 0.05 and 0.20. To increase the stability of this solid solution, BaTiO$_3$ (BT) was added [37] but pyrochlore phases still existed, although the quantity of such phases was reduced with increasing BT concentration.

The exhibition of good physical properties in Bi-based compounds has been reasoned as a consequence of the presence of Bi's stereo-chemically active lone-pair of electrons [38]. Further evidence for this came from Grinberg et al. [39] who verified the proposed empirical correlation between tolerance factor and MPB through density-functional-theory calculations. The author also predicted a few new Bi-based compound such as Bi(Zn$_{1/2}$Zr$_{1/2}$)O$_3$−PT and Bi(Cd$_{1/2}$Ti$_{1/2}$)O$_3$-PT as promising piezoelectric candidates. Another theoretical study on perovskites BiMO$_3$ (M = Al,Ga,In, and Sc) [40] also argued that the ferroelectric properties in these materials come from the 6s^2 lone pair of the Bi ion and described these as promising ferroelectric, piezoelectric, multiferroic and photocatalytic materials. Table 1-3 shows a series of novel Bi-based compound and their maximum Curie temperatures reported by Stringer et al. [41].

1.3.4 Lead-free materials

The quest for lead-free alternatives to PZT has seen a number of solid-solutions targeted in the search for MPB-behaviour since piezoelectric coefficients are often greatly enhanced in the vicinity of an abrupt change in crystal symmetry with composition. At present, tungsten bronze-type (e.g. K$_2$BiNb$_5$O$_{15}$), bismuth layer-structured-type (e.g. Bi$_3$TiNbO$_9$), and perovskite-type (e.g. BaTiO$_3$ based solid solutions, Na$_{1/2}$Bi$_{1/2}$TiO$_3$, Na$_{1/2}$K$_{1/2}$NbO$_3$) ferroelectrics are believed to be promising candidates for lead-free

Abbreviation	S.S end member $(1-x)ABO_3 + xPbTiO_3$	End member tolerance factor (t)	MPB Curie temp. (°C)
PMW	$Pb(Mg,W)O_3$	0.993	60
PMT	$Pb(Mg,Ta)O_3$	0.989	80
PNN	$Pb(Ni,Nb)O_3$	0.994	130
PFN	$Pb(Fe,Nb)O_3$	1.001	140
PMN	$Pb(Mg,Nb)O_3$	0.989	160
PMnN	$Pb(Mn,Nb)O_3$	0.973	187
PZnN	$Pb(Zn,Nb)O_3$	0.986	190
PST	$Pb(Sc,Ta)O_3$	0.977	205
PSn	$PbSnO_3$	0.978	220
PCN	$Pb(Co,Nb)O_3$	0.985	250
PSN	$Pb(Sc,Nb)O_3$	0.977	260
PCW	$Pb(Co,W)O_3$	0.987	310
PIN	$Pb(In,Nb)O_3$	0.965	320
PH	$PbHfO_3$	0.969	340
NBT	$(Na,Bi)TiO_3$	0.977	350
PYN	$Pb(Yb,Nb)O_3$	0.951	360
PZ	$PZrO_3$	0.964	385
BS	$BiScCO_3$	0.907	450
BI	$BiInO_3$	0.884	~550*
BY	$BiYbO_3$	0.857	~650*

*projected.

(a)

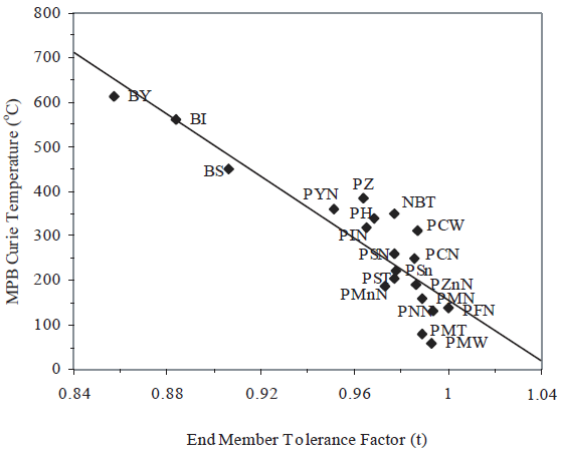

(b)

Figure 1-11 Tolerance factors and Curie temperatures of PT-based solid solutions with MPB compositions [33].

Table 1-3 Bi-based solid solutions with $PbTiO_3$ and their Curie temperatures. The data have been taken from the article by Stringer et al. [41]

Sample	Maximum T_c (°C)
$BiFeO_3$-PT	825
$Bi(Zn_{1/2}Ti_{1/2})O_3$-PT	715
$BiInO_3$-PT	562
$Bi(Zn_{2/3}Nb_{1/3})O_3$-PT	543
$BiMg_{1/2}Ti_{1/2}O_3$-PT	525
$Bi(Ni_{1/2}Ti_{1/2})O_3$-PT	503
$Bi(Mg_{2/3}Nb_{1/3})O_3$-PT	495
$Bi(Mg_{3/4}W_{1/4})O_3$-PT	495
$Bi(Co_{1/2}Ti_{1/2})O_3$-PT	514

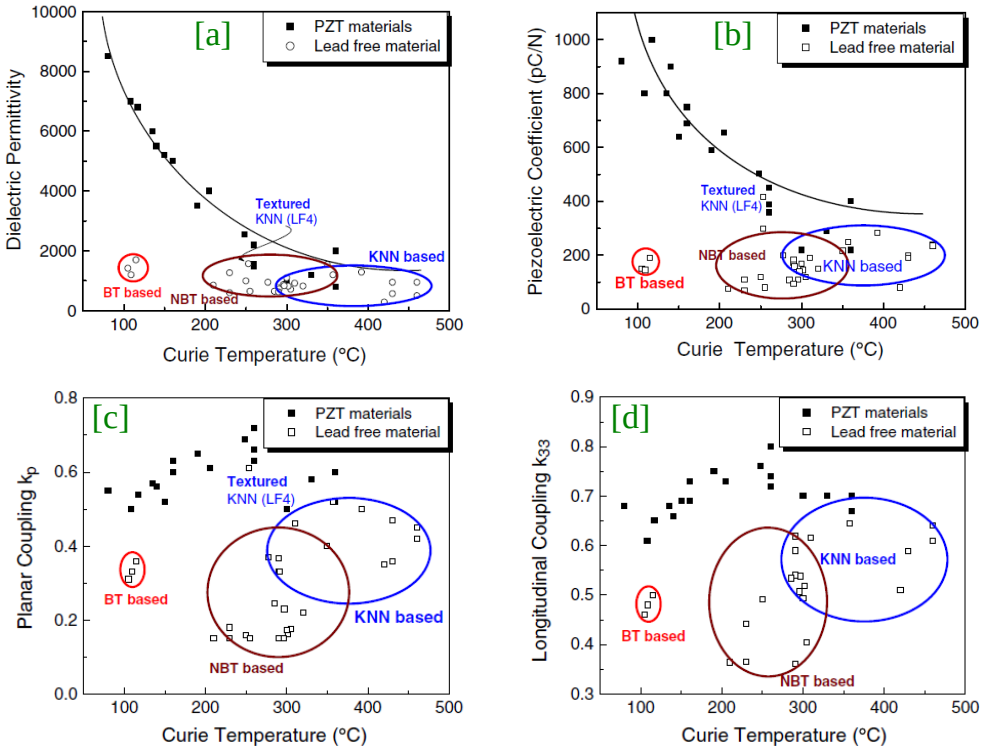

Figure 1-12 Comparison of various physical properties between lead-based and lead-free materials [44].

piezoelectrics [42, 43]. But, the ferroelectric or piezoelectric properties of these materials are not yet suitable to replace the lead-based compounds, such as PZT straightaway. A comparison of different piezoelectric properties between the common lead-free materials and the PZT-based materials is shown in fig 1-12.

Among the perovskite-based lead-free systems, $BaTiO_3$-based (BT), $Na_{1/2}Bi_{1/2}TiO_3$-based (NBT) and $K_xNa_{1-x}NbO_3$-based (KNN) materials have been investigated extensively in order to develop novel systems with improved qualities. BT was developed during 1940-1950 [45] and is used commonly in high permittivity dielectrics for capacitors. BT itself does not show very high piezoelectric properties (d_{33} for ceramics ~ 191 pC/N) and it has a low Curie temperature (~ 120°C), but in solid solutions with other compounds, properties can be significantly enhanced. BT has been studied in numerous solid solutions, but a few important examples with a phase boundary between two different structures are BT-NBT (discussed in chapter 5), BT-$K_{1/2}Bi_{1/2}TiO_3$ (fig 1-13), BT-KNN [46, 47] (example of an orthorhombic-tetragonal phase boundary) and BT-$BiFeO_3$[48] (tetragonal-rhombohedral phase boundary). In addition to these attempts

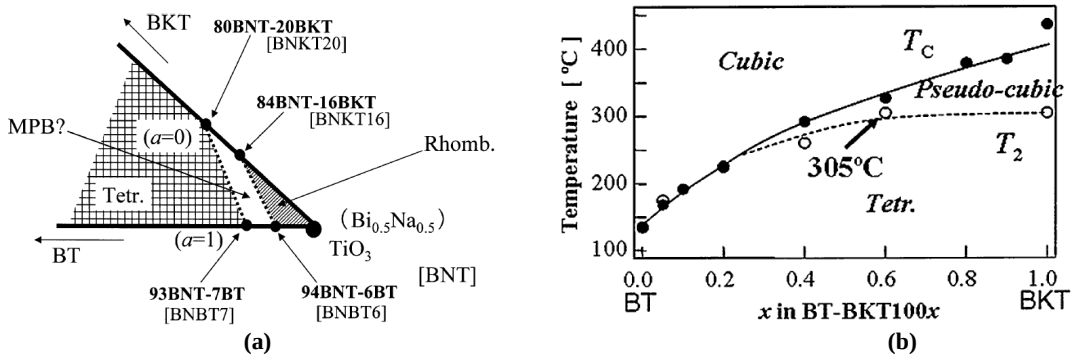

Figure 1-13 (a). Quasi-ternary phase diagram between KBT-NBT and BT-NBT. (b). Phase transition temperature of KBT-BT ceramics as a function of composition [54].

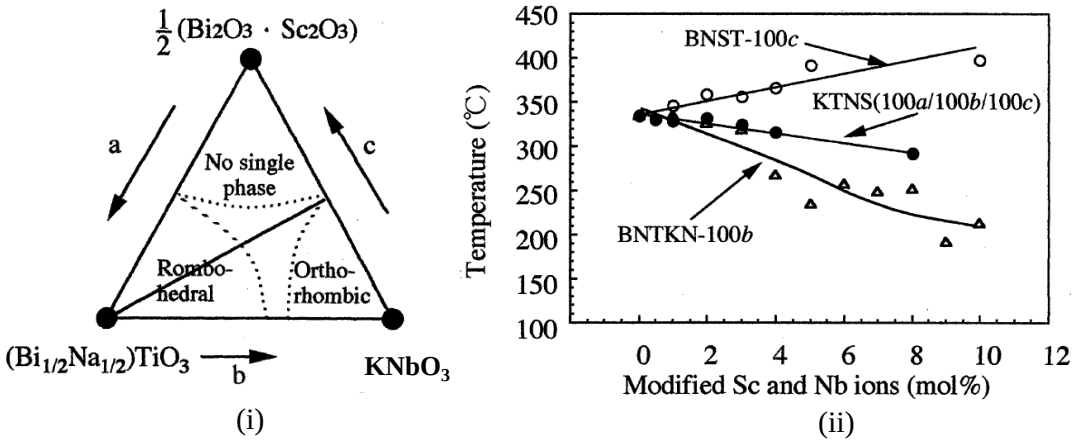

Figure 1-14 (i). Ternary phase diagram for NBT, $KNbO_3$ and $1/2(Bi_2O_3\text{-}Sc_2O_3)$. (ii). Curie temperatures of the ceramics for different comopositions [55].

to improve the piezoelectric properties of BT, recent investigations have showed some exceptional non-piezoelectric properties including piezoresistivity [49], colossal permittivity ($\sim 10^6$) for nano-crystalline ceramics [50] and very large reversible strain ($\sim$ 8%) due to defect-mediating domain switching [51]. Nevertheless, BT still continues to serve as a model system for fundamental investigations [52, 53].

Similar to BT, NBT is also a well-studied perovskite with relatively high phase transition temperature (at $\sim$ 325°C) in the lead-free community. This is considered as a good lead-free piezoelectric because of its large remanent polarization ($P_r \sim 38$ mC/cm^2) at room temperature [42]. Although developed in the 1960s [56], this material did not receive much attention until the recent surge in developments of lead-free

Table 1-4 Examples of NBT-based solid solutions with phase boundaries.

Binary Systems	Comments
xKNbO$_3$-NBT	Rhombohedral - tetragonal phase boundary $x \sim 0.08$ [57]
xBi$_{1/2}$Li$_{1/2}$TiO$_3$-NBT	Rhombohedral - pseudocubic phase boundary $x \sim 0.20$ [58]
xBa(Al$_{1/2}$Sb$_{1/2}$)O$_3$-NBT	Rhombohedral - pseudocubic phase boundary $x \sim 0.045$ [59]
xNaNbO$_3$-NBT	Rhombohedral - orthorhombic phase boundary $x \sim 0.91$ [60]
xBiCu$_{1/2}$W$_{1/2}$O$_3$-NBT	Rhombohedral - tetragonal phase boundary [61]
xKNN-NBT	Rhombohedral - tetragonal phase boundary $x \sim 0.07$ [62, 63]
Ternary systems	
NBT-KNbO$_3$-1/2(Bi$_2$O$_3$-Sc$_2$O$_3$)	Figure 1-14
NBT-KBT-BT	Figure 1-13a

materials. In 2002 Jones and Thomas [4] reported a detailed structural investigation on NBT, which suggested a rhombohedral ($R3c$) - tetragonal ($P4bm$) - cubic ($Pm\bar{3}m$) sequence of phase transformations with the increase of temperature. Pure NBT suffers from a high coercive field (7.3kV/mm) and high conductivity because of the loss of Bi during processing. Therefore to improve these physical properties and to discover potential MPB behaviour, NBT has been investigated in various solid solutions. Table 1-4 presents some important NBT-based solutions.

Another important lead-free system is KNN which is a solid solution between KNbO$_3$ (ferroelectric) and NaNbO$_3$ (antiferroelectric). This system has more than one phase-boundary as a function of composition (fig 1-15). The important physical constants of undoped KNN are not very high ($d_{33} \sim 90$ pC/N, $k_p \sim 25$ [64]) and the difficulties in making this solid solution have made this particular system unattractive in terms of industrial applications. But the recent publication by Saito et al. [12] has promoted much interest which reported the existence of a MPB between tetragonal and orthorhombic phases in a complex solid solution {(K$_{0.5}$Na$_{0.5}$)$_{1-x}$-Li$_x$}-(Nb$_{1-y}$Ta$_y$)O$_3$ with enhanced piezoelectric properties and a high Curie temperature of the order of 250 °C (fig 1-16).

1.4 Scope of this thesis

In recent years, there has been a considerable and renewed interest in the study of the structural changes occurring in ferroelectric solid-solutions as a function of composition and this has been further stimulated by the quest for lead-free alternatives to lead-based systems with equally high piezoelectric effects. In this context, detailed

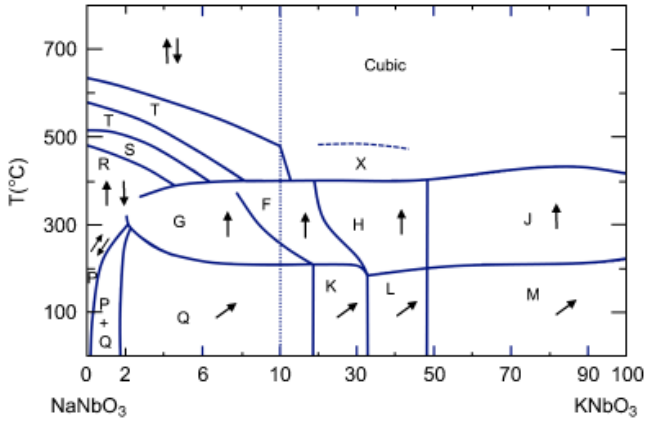

Figure 1-15 The phase diagram of $K_xNa_{1-x}NbO_3$. Regions labeled with Q, K, and L are monoclinic, although angular distortions are such that they are commonly regarded as orthorhombic ferroelectric; M and G are orthorhombic ferroelectric; F, H, and J are tetragonal ferroelectric. Region P is orthorhombic antiferroelectric [65, 66]. This figure is taken from the article by Rodel et al. [43]

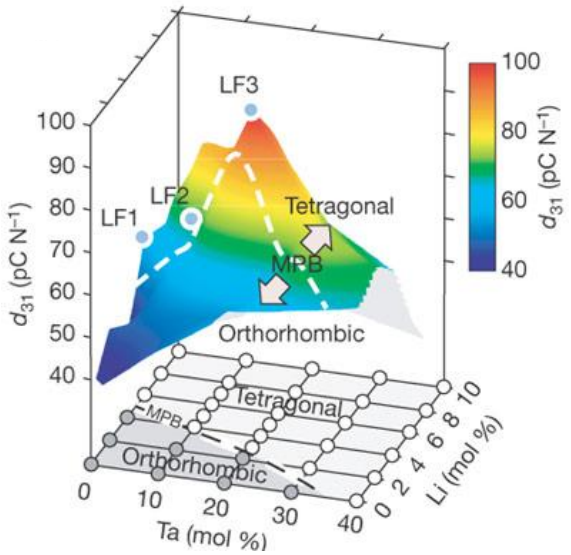

Figure 1-16 The phase diagram of $\{(K_{0.5}Na_{0.5})_{1-x}\text{-}Li_x\}\text{-}(Nb_{1-y}Ta_y)O_3$ reported by Saito et al. [12]

and high-quality crystallographic studies have an important role to play both in understanding structural changes at the MPB and the subsequent enhancement of physical properties. Therefore, the aim of this thesis is to demonstrate the importance of structural investigations of novel piezoelectric materials and to facilitate the understanding of structure-property relationships in these systems. In so-doing we have performed detailed structural studies of three different solid solutions : (1) $BiScO_3$−$PbTiO_3$ (BS-PT), (2) $BiScO_3$−$BaTiO_3$ (BS-BT) and (3) $Na_{1/2}Bi_{1/2})TiO_3$−$BaTiO_3$ (NBT-BT). Each system has been studied over a range of compositions and compositionally-driven structural phase transitions have been studied through diffraction experiments. A further aim of this work is to improve the understanding of the role of the Bi^{+3} ion in promoting ferroelectricty in a range of coordination environments. Finally, phase transitions as a function of temperature and physical properties of the ceramics have been studied through dielectric measurements as a complementary aid to understanding these complex systems.

References

[1] W. J. Merz, Phys. Rev. **76**, 1221 (1949).

[2] K. Uchino, *Ferroelectric Devices* (CRC Press, 2000).

[3] E. Fesenko, *Perovskite Family and Ferroelectricity* (Atomizdat, Moscow, 1972).

[4] G. O. Jones and P. A. Thomas, Acta Cryst. B **58**, 168 (2002).

[5] N. W. Thomas, Acta Cryst. B **45**, 337 (1989).

[6] N. W. Thomas, Acta Cryst. B **52**, 16 (1996).

[7] H. D. Magaw and C. N. Darlington, Acta Cryst. A **31**, 756 (1974).

[8] A. M. Glazer, Acta Cryst. B **28**, 3384 (1972).

[9] A. M. Glazer, Acta Cryst. A **31**, 756 (1975).

[10] J. A. K. Howard, ed., *Crystallographic Instrumentation* (Oxford University Press, 1998).

[11] E. Cross, Nature **432**, 24 (2004).

[12] Y. Saito, H. Takao, T. Tani, T. Nonoyama, K. Takatori, T. Homma, T. Nagaya, and M. Nakamura, Nature **432**, 84 (2004).

[13] A. Bhalla, R. Guo, and R. Roy, Mat. Res. Innovat. **4**, 3 (2000).

[14] D. M. Smyth, Ferroelectric **380**, 1 (2009).

[15] B. Jaffe, R. Roth, and S. Marzullo, J. Appl. Phys. **25**, 809 (1954).

[16] E. Sawaguchi, J. Phys. Soc. Japan **8**, 615 (1953).

[17] B. Jaffe, W. R. Cook, and H. Jaffe, *Piezoelectric Ceramics* (Academic Press, London, 1971).

[18] B. Noheda, J. Gonzalo, L. Cross, R. Guo, S. E. Park, D. Cox, and G. Shirane, Phys. Rev. B **61**, 8687 (2000).

[19] B. Noheda, D. E. Cox, G. Shirane, J. A. Gonzalo, L. E. Cross, and S. E. Park, Appl. Phys. Lett. **74**, 2059 (1999).

[20] D. Pandey, A. K. Singh, and S. Baik, Acta Crystallogr., Sect. A: Found. Crystallogr **64**, 192 (2008).

[21] K. A. Schonau, L. A. Schmitt, H. F. M. Knapp and, R. A. Eichel, H. Kungl, and M. J. Hoffmann, Phys. Rev. B **75**, 184117 (2007).

[22] A. M. Glazer, P. A. Thomas, K. Z. Baba-Kishi, G. K. H. Pang, and C. W. Tai, Phys. Rev. B **70**, 184123 (2004).

[23] J. Frantti, J. Phys. Chem. **112**, 6521 (2008).

[24] W. Heywang, K. Lubitz, and W. Wersing, eds., *Piezoelectricity: Evolution and Future of a Technology* (Springer, 2008).

[25] S.-E. Park and T. R. Shrout, Mat. Res. Innovat. **1**, 20 (1997).

[26] S.-E. Park and T. R. Shrout, IEEE Transactions on Ultrasonics, Ferroelectrics and Frequency Control **44**, 1140 (1997).

[27] F. Jona and G. Shirane, *Ferroelectric Crystals* (Oxford Pergamon Press, 1962).

[28] J. Kuwata, K. Uchino, and S. Nomura, Ferroelectrics **37**, 579 (1981).

[29] S. Choi, T. Shrout, S. Jang, and A. Bhalla, Mater. Lett. **8**, 253 (1989).

[30] T. R. Shrout, Z. P. Chang, N. Kim, and S. Markgraf, Ferroelectr. Lett. Sect. **12**, 63 (1990).

[31] Y. Yamashita, Jpn. J. Appl. Phys. **33**, 5328 (1994).

[32] S.-E. Park and T. R. Shrout, J. Appl. Phys. **82**, 1804 (1997).

[33] R. E. Eitel, C. A. Randall, T. R. Shrout, P. W. Rehrig, W. Hackenberger, and S. E. Park, Jpn. J. Appl. Phys. **40**, 5999 (2001).

[34] R. Duan, R. F. Speyer, E. Alberta, and T. R. Shrout, J. Mater. Res. **19**, 2185 (2004).

[35] S. Zhang, R. Xia, C. A. Randall, T. R. Shrout, R. Duan, and R. F. Speyer, J. Mater. Res. **20**, 2067 (2005).

[36] G. Feng, H. Rongzi, L. Jiaji, L. Zhen, C. Lihong, and T. Changsheng, J. Eur. Ceram. Soc. **29**, 1687 (2009).

[37] G. Feng, H. Rongzi, L. Jiaji, L. Zhen, C. Lihong, and T. Changsheng, J. Alloys Compd. **475**, 619 (2009).

[38] P. Baettig, C. F. Schelle, R. LeSar, U. V. Waghmare, and N. A. Spaldin, Chem. Mater. **17**, 1376 (2005).

[39] I. Grinberg, M. R. Sochomel, P. K. Davies, and A. M. Rappe, J. Appl. Phys. **98**, 094111 (2005).

[40] H. Wang, B. Wang, Q. Li, Z. Zhu, R. Wang, and C. H. Woo, Phys. Rev. B **75**, 245209 (2007).

[41] C. J. Stringer, T. R. Shrout, C. A. Randall, and I. M. Reaney, J. Appl. Phys. **99**, 024106 (2006).

[42] T. Takenaka, K. Maruyama, and K. Sakata, Jpn. J. Appl. Phys. **30**, 2236 (1991).

[43] J. Rodel, W. Jo, K. T. P. Seifert, E. M. Anton, T. Granzow, and D. Damjanovic, J. Am. Ceram. Soc. **92**, 1153 (2009).

[44] T. R. Shrout and S. J. Zhang, J Electroceram **19**, 111 (2007).

[45] A. von Hippel, Reviews of Modern Physics **22**, 221 (1950).

[46] Y. P. Guo, K. Kakimoto, and H. Ohsato, Jpn. J. Appl. Phys. **43**, 6662 (2004).

[47] C. W. Ahn, H. C. Song, S. Nahm, S. H. Park, K. Uchino, S. Priya, H. G. Lee, and N. K. Kang, Jpn. J. Appl. Phys. **44**, L1361 (2005).

[48] M. M. Kumar, A. Srinivas, and S. V. Suryanarayana, J. Appl. Phys. **87**, 855 (2000).

[49] J. S. Capurso and W. A. Schulze, J. Amer. Ceram. Soc. **81**, 337 (1998).

[50] S. Guillemet-Fritsch, Z. Valdez-Nava, C. Tenailleau, T. Lebey, B. Durand, and J. Y. Chane-Ching, Advan. Mater. **20**, 551 (2008).

[51] X. B. Ren, Nat. Mater. **3**, 91 (2004).

[52] R. C. Rogan, N. Tamura, G. A. Swift, and E. Ustundag, Nat. Mater. **2**, 379 (2003).

[53] L. Zhang, E. Erdem, X. Ren, and R. A. Eichel, Appl. Phys. Lett. **93**, 202901 (2008).

[54] T. Takenaka, H. Nagata, and Y. Hiruma, Jpn. J. Appl. Phys. **47**, 3787 (2008).

[55] H. Nagata and T. Takenaka, Appl. Phys. Lett. **37**, 5311 (1998).

[56] G. A. Smolenskii, V. A. Isupov, A. I. Agranovskaya, and N. N. Krainik, Sov.Phys.Solid State (Eng.Transl.) **2**, 2651 (1961).

[57] Y. Hiruma, H. Nagata, and T. Takenaka, J. Appl. Phys. **104**, 124106 (2009).

[58] Y. Hiruma, K. Yoshii, H. Nagata, and T. Takenaka, J. Appl. Phys. **103**, 084121 (2008).

[59] Y. Hiruma, H. Nagata, and T. Takenaka, Appl. Phys. Lett. **95**, 052903 (2009).

[60] T. Takenaka, T. Okuda, and K. Takegahara, Ferroelectrics **196**, 175 (1997).

[61] X. X. Wang, H. L. W. Chan, and C. L. Choy, J. Am. Ceram. Soc. **86**, 1809 (2003).

[62] A. B. Kounga, S.-T. Zhang, W. Jo, T. Granzow, and J. Rodel, Appl. Phys. Lett. **92**, 222902 (2008).

[63] R. Zuo, X. Fang, and C. Ye, Appl. Phys. Lett. **90**, 092904 (2007).

[64] M. D. Maeder, D. Damjanovic, and N. Setter, J. Electroceram. **13**, 385 (2004).

[65] M. Ahtee and A. M. Glazer, Acta Crystallogr., Sect. A: Found. Crystallogr. **32**, 434 (1976).

[66] M. Ahtee and A. W. Hewat, Acta Crystallogr., Sect. A: Found. Crystallogr. **34**, 309 (1978).

Chapter 2

Background to Experimental Methods

2.1 Preparation of powder samples

Ceramic samples of the different systems investigated were prepared following the standard solid-state synthesis route. Conventional solid-state synthesis techniques involve heating mixtures of two or more starting compounds to form a solid-state product. The term 'solid-state' is used to describe interactions which are neither in a solvent medium nor a controlled vapor-phase interactions. The mechanism responsible for the solid-solid reaction is mainly diffusion which is governed by the Fick's law :

$$J = -D\frac{dc}{dx} \tag{2-1}$$

where J = Flux of diffusing species ($cm^{-2}s^{-1}$) , D = Diffusion coefficient (cm^2/s) and (dc/dx) = Concentration gradient (cm^{-4}) [1].

For a typical rate of reaction the diffusion coefficient is of the order of 10^{-12} cm^2s^{-1}. To achieve a good rate of diffusion, the temperature should be close to the melting point of the starting materials. This is known as Tammann's Rule [2] which states that for an effective rate of the reaction the temperature has to be between 70 and 80 % of the melting point of the constituents. However, this depends on the nature of the bonds in the starting materials. There are also other ways to influence the rate of the reaction, such as, the reaction rate can increase with an increase in the contact area. This is normally achieved by pressing pellets from the powder samples.

In this thesis, three different solid solutions (1) $BiScO_3$-$PbTiO_3$, (2) $BiScO_3$-$BaTiO_3$, (3) $Na_{1/2}Bi_{1/2}TiO_3$-$BaTiO_3$ were prepared following the conventional solid-state synthesis route. Starting materials were the oxides or carbonates of the elements with purity approximately 99.9%. The procedure involved the following steps:

1. Calculation of the stoichiometric quantities of oxides or carbonates required from the fundamental reaction-equation.

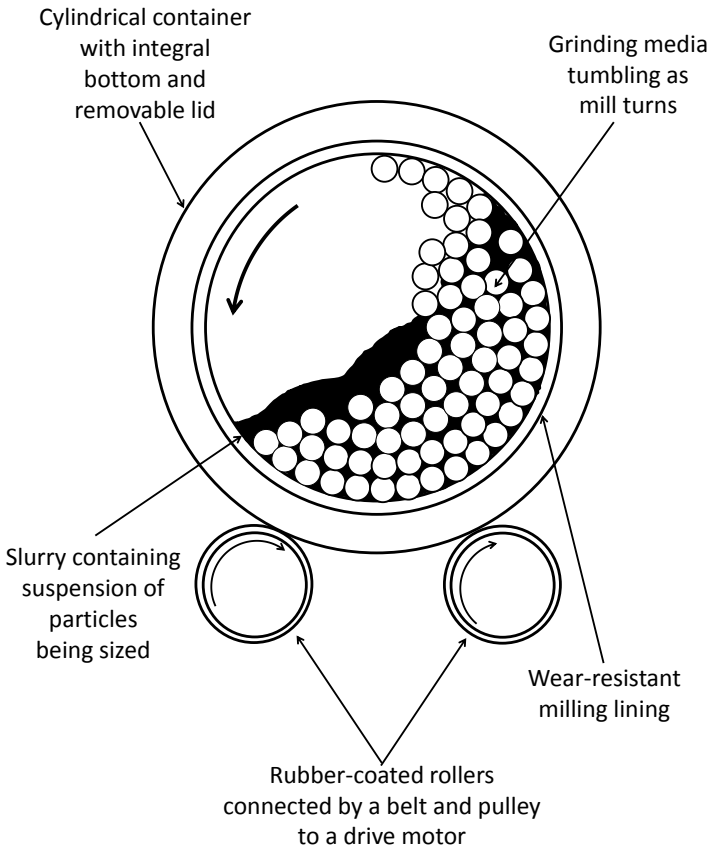

Figure 2-1 A schematic diagram of a typical laboratory ball-milling set-up (Courtesy : Nattapol Laorodphan).

2. Mixing thoroughly for about 24 h in an ethanol medium with zirconia balls (diameter ~ 0.3 mm). Figure 2-1 shows the laboratory milling set-up.

3. Drying the slurry in an oven at a temperature ~ 75 °C.

4. Grinding the dried mixture by mortar and pestle.

5. Calcination in a sealed platinum crucible for about 6 - 10 h at ~ 1000 °C.

6. Grinding.

7. Sintering for 4 - 6 h between 1100 °C and 1200 °C.

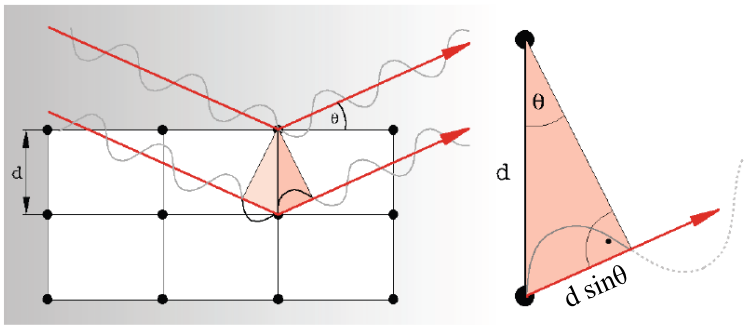

Bragg's Law : $2d_{hkl}\sin\theta = n\lambda$, for constructive interference.

Figure 2-2 Schematic diagram to illustrate Bragg's law for diffraction.

2.2 X-ray and neutron powder diffraction

Powder diffraction is a convenient, non-destructive way to characterize crystalline materials and powder diffractometers have become an indispensable part of any modern Physics, Chemistry, Material science and Engineering laboratory. A powder sample typically represents a cluster of randomly oriented single crystals and when exposed to electromagnetic radiation of a suitable wavelength ($\sim$ 1 Å), each phase present in the sample produces a distinctive diffraction pattern following Bragg's law (fig 2-2). This pattern can be used to investigate crystal structure, atomic substitution, phase transformation and chemical reaction. In addition, it is also possible to perform quantitative phase analysis for a multi-phase system. Finally, subtle features of diffraction patterns can also provide details of the microstructure of the sample, such as particle size, strain distribution and defects [3–5].

2.2.1 X-ray powder diffraction

2.2.1.1 X-ray scattering

X-rays are electromagnetic waves with wavelengths in the region of an angstrom ($10^{-10}m$) and interact primarily with the electrons. For an incident beam with intensity I_0, the scattered radiation from a single electron at a distance r can be computed from Thomson's equation:

$$I_e = I_0\left(\frac{e^4}{r^2m^2c^4}\right)\left(\frac{1+\cos^2 2\theta}{2}\right) \tag{2-2}$$

The angular factor in the above equation is known as the polarization factor, which accounts for the unpolarized incident beam.

When an x-ray beam is incident upon an atom with atomic number Z, each of its electrons will scatter the x-ray photons according to the Thomson equation. However, the coherent scattering intensity is obtained from the atomic form factor (f) for a given angle θ and wavelength λ. Physically it represents the ratio of the amplitude scattered by the entire atom to the amplitude scattered in the same direction by a single electron. The values of atomic scattering factors are given in the International Tables for Crystallography [6]. The scattering of x-rays from a complete unit cell can be computed by taking into account the relative positions (x, y, z) of all the atoms in the unit cell. The quantity that describes scattering from a unit cell is known as the structure factor which can be written as:

$$F_{hkl} = \sum_{j=1}^{N} f_j e^{i\phi} = \sum_{j=1}^{N} f_j e^{2\pi i(hx+ky+lz)} \tag{2-3}$$

$$f_j = f_0 e^{-B(\sin^2\theta/\lambda^2)} \tag{2-4}$$

where N is the number of atoms in the unit cell, f_0 is the atomic scattering factor for atoms at rest and B is a correction factor for the thermal motion of the atoms. The intensity in the diffracted beam from the planes (hkl) is proportional to the modulus square of the structure factor:

$$I_{hkl} \approx |F_{hkl}|^2 \tag{2-5}$$

However, in a typical x-ray powder diffraction experiment, the measured intensity represents a time average of a fraction of the total scattered intensity, which is further affected by various geometrical and physical factors such as the Lorentz factor, absorption, multiplicity, scale factor and preffered orientation.

2.2.1.2 Experimental setup

For diffraction experiments x-rays are used with wavelengths in the range 0.1-5 Å. In a standard laboratory instrument x-rays are produced in a sealed vacuum tube, where electrons are accelerated by a large potential difference (up to ~ 60kV) to hit a metal anode. For routine powder diffraction experiments, a Cu tube is the most common choice which provide the wavelength ≈ 1.5406 Å.

Table 2-1 Details of the experimental set-up in x-ray diffractometer.

Diffractometer	PANalytical MPD
Wavelength	1.540598 Å
X-ray tube:	
Anode material	Cu
Voltage	45 kV
Current	40 mA
Focus type	Line
Length	12 mm
width	0.4 mm
Take-off angle	6.0°
Monochromator Crystal	Ge
Reflection (*hkl*)	(111)
Beam Mask width	10 mm
Divergence slit:	
Distance to sample	140 mm
Fixed Angle	0.25°
Sample revolution time	4 sec
Anti-scatter slit:	
Distance to sample	240 mm
Angle	0.25°
Soller slit	
Opening	0.02
Detector Name	PIXcel

X-ray powder diffraction has been utilized in this work mainly to identify different phases and to monitor phase formations at different stages of sample preparation. Data were collected using a PANalytical X'Pert Pro Multi-purpose diffractometer (MPD) which is a high-resolution powder diffractometer based on typical Bragg-Brentano geometry in $\theta - 2\theta$ arrangement. This geometry is also known as flat-plate reflection geometry where a divergent incident beam is reflected from the surface of the sample and converges at a fixed radius from the sample position. In $\theta-2\theta$ arrangement the x-ray tube is stationary while the specimen stage and the detector synchronously move in the angular ratio 1:2. To get a good powder average, the sample is usually spun about an axis normal to the flat plate. The beam divergence is controlled by a slit after the source and the axial divergence is reduced by using the soller collimators. Figure 2-3 shows the Bragg-Brentano geometry of the high-resolution diffractometer which employs a perfect-crystal pre-sample monochromator to achieve focused pure CuKα_1 radiation. The details of our laboratory is given in table 2-1.

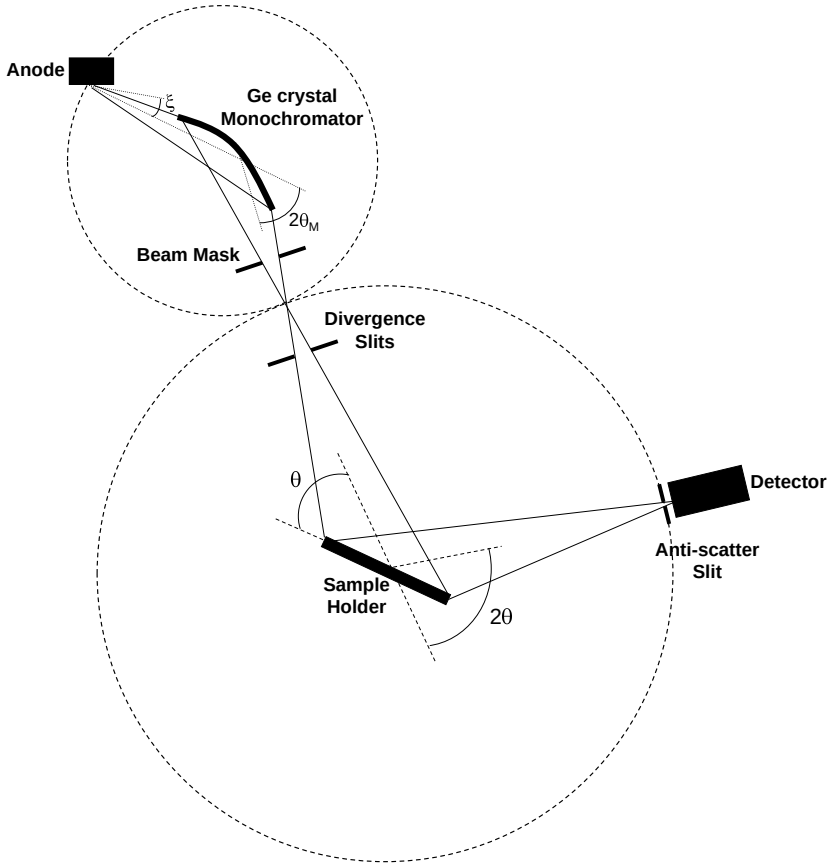

Figure 2-3 Schematic diagram of Bragg-Brentano geometry in laboratory x-ray diffractometer (Couretsy : Nattapol Laorodphan).

2.2.2 Neutron powder diffraction

2.2.2.1 Neutron scattering

The geometrical aspects of x-ray and neutron diffraction are the same, but the interaction between the neutron and the material is different. Neutrons scatter primarily from the nuclei of atoms via short range interactions. A total neutron scattering cross-section, σ_T is expressed as :

$$\sigma_T = 4\pi\bar{b^2} \tag{2-6}$$

where b is called the scattering length whose value depends on the neutron-nucleus interaction. Unlike x-ray scattering factors, which monotonically increase with atomic number and vanish at large Q ($4\pi \sin\theta/\ \lambda$), neutron scattering lengths vary erratically with atomic number, nearly independent of Q and show distinct variations for different isotopes (fig 2-4, 2-5).

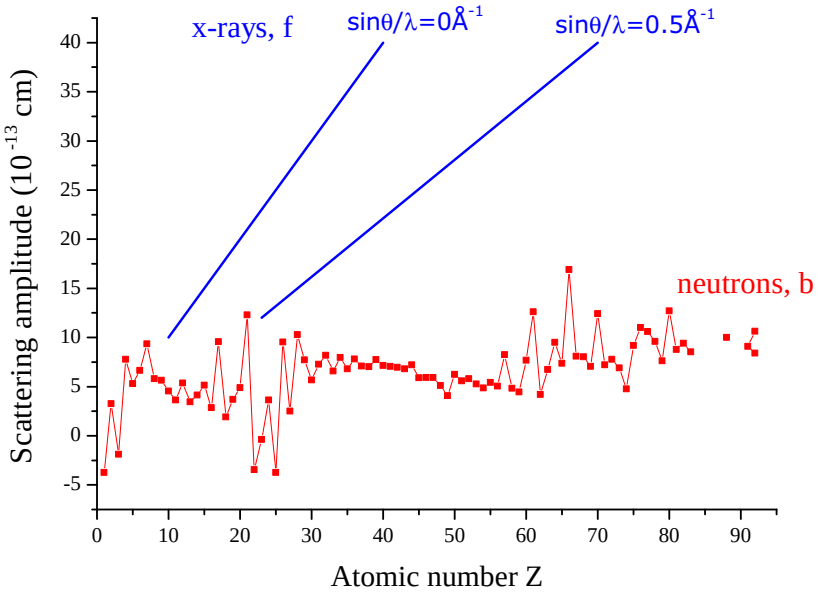

Figure 2-4 Variation of neutron scattering length (b) as a function of atomic number Z. The blue lines describe the dependence of the atomic form factor (x-ray) on atomic number Z for a specific Q ($= 4\pi \sin\theta/\lambda$).

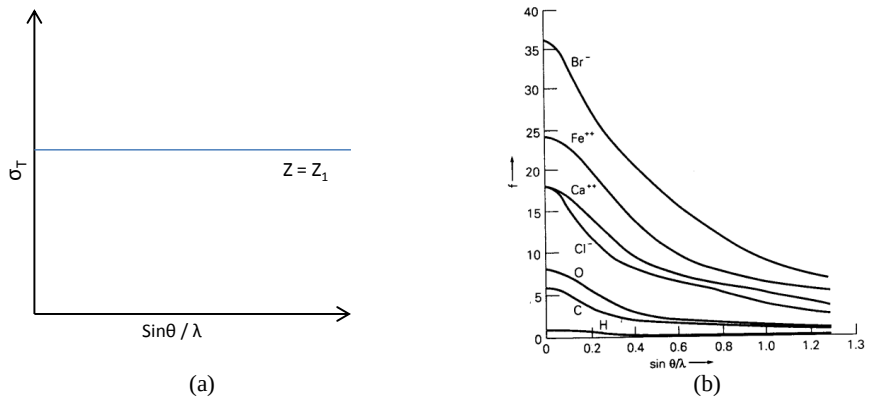

Figure 2-5 Variation of (a) neutron scattering cross section (b) x-ray atomic form factor as a function of Q ($= 4\pi \sin\theta/\lambda$) for a specific Z.

Neutron diffraction techniques are used predominantly for refining or obtaining additional information on structures studied by x-ray diffraction. In the absence of magnetic scattering, diffraction peaks give the time-averaged distribution of the nuclei because of the thermal motion. This gives a better possibility (compared to x-ray analysis) for determining the position of light atoms in the presence of heavy ones, structure containing atoms with close Z or even isotopes and is also good for studying phenomena requiring data over a large range of *d*-spacings, for example to determine anisotropic thermal displacement parameters.

2.2.2.2 Time of flight technique

Time of flight (TOF) techniques use a polychromatic beam and a pulsed source of neutrons, and exploit the fact that the wavelength of a neutron is inversely proportional to its velocity (v) following the de Broglie equation. Therefore, neutrons with long wavelengths are slower than the neutrons with short wavelengths. By recording the arrival time (t) of each neutron of a particular pulse in the detector , its wavelength (λ) and the corresponding *d*-spacing of the Bragg planes can be calculated from the following relation:

$$\lambda = h/m_n v = ht/m_n L = 2d \sin\theta \tag{2-7}$$

where 'L' refers to the length of the flight path.

The relative uncertainty in *d*-spacing can be estimated from the equation:

$$\left(\frac{\delta d}{d}\right)^2 = \left(\frac{\delta t}{t}\right)^2 + \left(\frac{\delta L}{L}\right)^2 + (\cot\theta\delta\theta)^2 \tag{2-8}$$

where δt, δL and $\delta\theta$ are the uncertainties in the time of flight , path length and scattering angle, respectively.

Figure 2-6 shows a schematic of the high-resolution powder diffractometer HRPD [7] at ISIS, which has a very long flight path of around 100m with detectors at low angle ($28° < 2\theta < 32°$), 90°, and at back-scattering ($160° < 2\theta < 176°$) positions. The

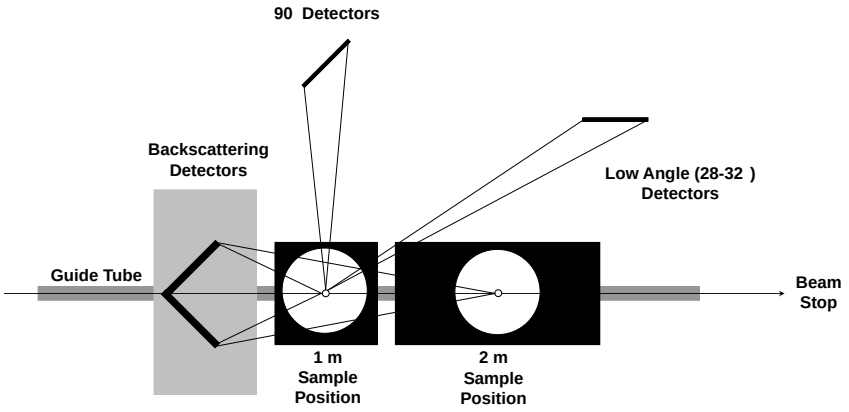

Figure 2-6 Schematics of the HRPD TOF diffractometer at ISIS (Courtesy: Nattapol Laorodphan).

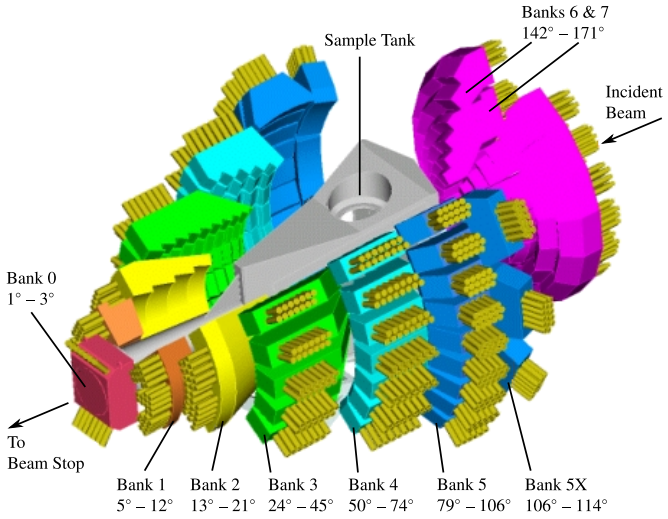

Figure 2-7 A schematic presentation of the General Materials Diffractometer (GEM) at ISIS. GEM is designed to be a high intensity, high resolution neutron diffractometer for structural studies of both disordered materials and crystalline powders. GEM has an incident flight path L1 = 17 metres. GEM has zinc sulphide scintillator detectors which cover a very wide range in scattering angle from 1.1° to 169.3°. Data were collected for BS-PT system using this diffractometer [8].

three banks have approximate resolution ($\delta d/d$) of 2×10^{-2}, 2×10^{-3} and 4×10^{-4}, respectively.

2.3 Rietveld Method

Hugo M. Rietveld, a Dutch physicist, demonstrated that accurate determination of crystal and magnetic structures is possible using neutron diffraction data from powders [9]. His approach was later extended to x-rays and named as the 'Rietveld Method'. The technique allows a large amount of structural information to be extracted from the intensities of overlapping reflections, whether they are partially or completely overlapped, by treating each point in the pattern as an individually observed intensity and then comparing a simulated pattern with the experimentally obtained pattern. It is important to note that the Rietveld method is a 'structure refinement method' not a 'structure solution method' - a prior knowledge of the crystal structure is essential to begin the refinement. The structural model is then improved by refinement, which involves altering the parameters of the model until the diffraction pattern calculated from the model gives the best agreement with the observed diffraction intensities within physical and chemical reason. A least-squares algorithm allows many parameters to be varied simultaneously and there are many automated programs available for this. Usually a refinement will involve varying the positional (x, y, z) and thermal parameters (U_{ij}) of each atom individually, along with other parameters such as overall scale factor(s), absorption and extinction corrections [10]. The essence of Rietveld's approach is that experimental powder diffraction data are utilized without extracting the individual integrated intensities or the individual structure factors, and all structural and instrumental parameters are refined by fitting a calculated profile to the observed data.

During refinement using the Rietveld method, the following system of equations is solved by means of a non-linear least squares minimization:

$$\begin{aligned} Y_1^{Obs} &= kY_1^{Calc} \\ Y_2^{Obs} &= kY_2^{Calc} \\ &\dots \\ &\dots \\ Y_n^{Obs} &= kY_n^{Calc} \end{aligned} \tag{2-9}$$

and the following function is minimized:

$$\Phi = \sum_{i=1}^{n} w_i (Y_i^{obs} - Y_i^{calc})^2 \tag{2-10}$$

Finally, the quality of the refinement using the Rietveld method is quantified by a number of figures of merit, defined as follows :

1. Profile residual, R_{p} :

$$R_{\mathrm{p}} = \left[\frac{\sum_{i=1}^{n} \left| Y_i^{obs} - Y_i^{calc} \right|}{\sum_{i=1}^{n} Y_i^{obs}} \right] \times 100\% \tag{2-11}$$

2. The weighted profile residual, R_{wp} :

$$R_{\mathrm{wp}} = \left[\frac{\sum_{i=1}^{n} w_i (Y_i^{obs} - Y_i^{calc})^2}{\sum_{i=1}^{n} w_i (Y_i^{obs})^2} \right]^{1/2} \times 100\% \tag{2-12}$$

3. The Bragg residual, R_{B} :

$$R_{\mathrm{B}} = \left[\frac{\sum_{j=1}^{m} \left| I_j^{obs} - I_j^{calc} \right|}{\sum_{j=1}^{m} I_j^{obs}} \right] \times 100\% \tag{2-13}$$

4. The expected profile residual, R_{exp} :

$$R_{\mathrm{exp}} = \left[\frac{n - p}{\sum_{i=1}^{n} w_i (Y_i^{obs})^2} \right]^{1/2} \times 100\% \tag{2-14}$$

5. The goodness of fit, χ^2 (also referred to chi-squared):

$$\chi^2 = \left[\frac{\sum_{i=1}^{n} w_i (Y_i^{obs} - Y_i^{calc})^2}{n - p} \right]^{1/2} = \frac{R_{wp}}{R_{exp}} \tag{2-15}$$

where, n is the total number of points measured in the experimental powder diffraction pattern;

Y_i^{obs} is the observed intensity of the i^{th} data point;

Y_i^{calc} is the calculated intensity of the i^{th} data point;

k is the scale factor;

w_i is the weight of the i^th data point, which is usually taken as $w_i = 1/\sigma_i^2 = 1/ Y_i^{obs}$;

m is the number of independent Bragg reflections;
I_j^{obs} the observed integrated intensity of the j^{th} Bragg peak;
I_j^{calc} is the calculated integrated intensity of the j^th Bragg peak; and
p is the number of free least squares parameters.

R values are useful to evaluate a refinement. Of the several R-factors, R_{wp} is statistically the most meaningful quantity since the numerator in the equation 2-14 is minimized during the refinement. Ideally the final R_{wp} should approach the statistically expected R value, R_{exp} and therefore, χ^2 should approach 1.0. The so-called Bragg R factor provides a comparison between the observed intensity and the calculated intensity. However the final quality of a Rietveld refinement should be judged by the fit of the calculated pattern to the observed data and the chemical sense of the structural model.

2.4 Dielectric properties

2.4.0.3 Theory

When an insulating dielectric material is placed under an electric electric field, there is no long-range charge transport but only a local re-arrangement of charge such that the material acquires a dipole moment. This phenomenon is known as polarization. Under an external electric field (**E**) the electric displacement vector **D** can be written as :

$$\mathbf{D} = \varepsilon\mathbf{E} = \varepsilon_0\mathbf{E} + \mathbf{P} \tag{2-16}$$

where ε is the dielectric permittivity and **P** is called the polarization (dipole moment per unit volume) which can be expressed as :

$$\mathbf{P} = \chi_e\varepsilon_0\mathbf{E} \tag{2-17}$$

where χ_e is the electric susceptibility and ε_0 is the free space permittivity (8.85×10^{12} C^2 N-m^2).

It follows from the above two equations that :

$$\mathbf{D} = \varepsilon_0\mathbf{E} + \chi_e\varepsilon_0\mathbf{E} = \varepsilon_0(1 + \chi_e)\mathbf{E} \tag{2-18}$$

$$\varepsilon = \varepsilon_0(1 + \chi_e) \tag{2-19}$$

$$\frac{\varepsilon}{\varepsilon_0} = (1 + \chi_e) = \varepsilon_r \tag{2-20}$$

where ε_r is called the relative permittivity.

In an alternating electric field the dielectric permittivity or relative permittivity is a complex quantity and it is written as:

$$\varepsilon_r = \varepsilon' + i\varepsilon'' \tag{2-21}$$

where the real part ε' is known as real permittivity or dielectric constant and the imaginary part (ε'') is related to the energy loss in the system. The dielectric response function of a system highly depends on the frequency and temperature because of the various polarization mechanisms and as a consequence resonance and relaxation effects occur as a function of frequency. The following four major polarization mechanisms are usually seen [11] :

1. Electronic polarization : This occurs as a result of the distorted electron cloud in response to an electric field and the atom temporarily acts as a dipole. The atomic polarization response time is very short and this contributes at high frequencies (fig 2-8).

2. Ionic polarization : In ionic polarization the constituent cations and anions of a crystal are physically displaced by the external field. The polarization has an average response time of $\sim$ 1ps because of the mass of the ions and therefore has no contribution above $\sim 10^{12}$ Hz.

3. Molecular polarization : This polarization involves rotation of molecules. It is a relatively slow process and contributes only at lower frequencies ($< 10^8$ Hz).

4. Space charge polarization: This is a result of the accumulation of charges in multiphase or inhomogeneous dielectrics. This contributes at even lower frequencies ($< 10^4$ Hz).

2.4.0.4 Dielectric response of ferroelectrics

Ferroelectric materials exhibit high dielectric constants (up to $\sim 10^5$ under certain conditions) because of the large spontaneous polarization. The polarization occurs either because of the ordering of the ions (order-disorder type ferroelectrics) or because of the small displacement of the cations with respect to the anions (displacive type

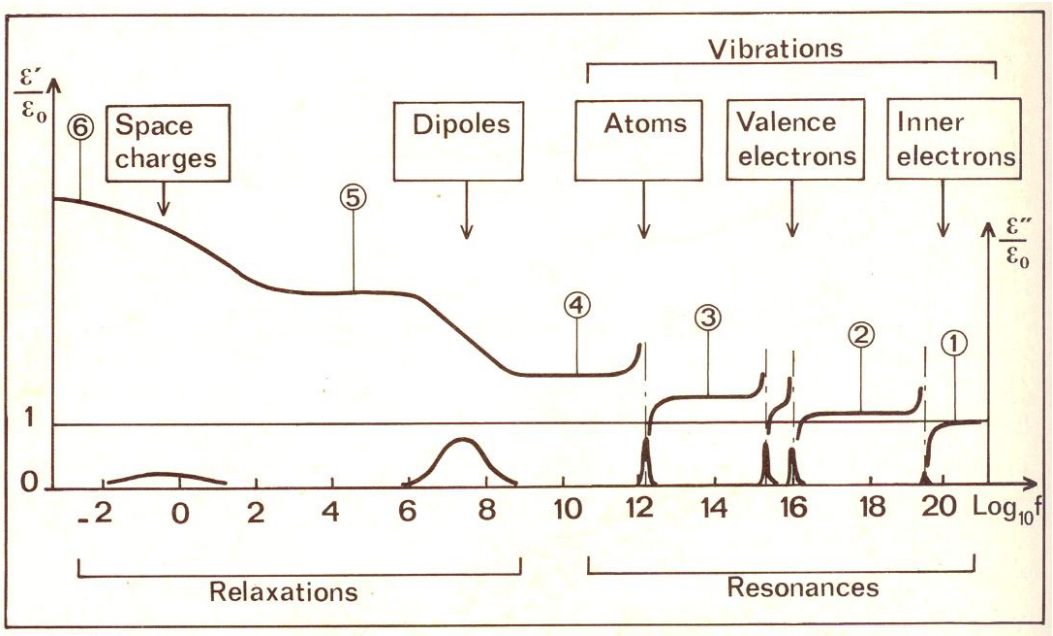

Figure 2-8 Variations of ε' and ε'' with frequency. Space charge and dipolar polarizations are strongly temperature-dependent. Ionic and electronic polarizations are resonance processes and temperature independent. Over critical frequency ranges energy dissipation is a maximum as shown by peaks in ε'' [11].

ferroelectrics). Crystals containing H-bonds are usually order-disorder type, such as KH_2PO_4, and ionic crystals, such as $BaTiO_3$, are generally displacive type ferroelectrics. The spontaneous polarization disappears above a certain temperature which is called the Curie point. The dielectric constant increases rapidly with the temperature and reaches the maximum near the Curie point. The high-temperature phase is called the paraelectric phase and the dielectric constant normally follows the Curie-Weiss equation above the phase transition temperature:

$$\varepsilon' = \frac{C}{T - T_o} \tag{2-22}$$

where C is known as the Curie constant and T_0 is a characteristic temperature which is equal to the the Curie temperature for 2nd-order phase transitions.

Figure 2-9 shows typical temperature-dependent dielectric constants for ferroelectric materials. Based on their response as a function of temperature and frequency it is possible to classify the ferroelectric materials into three major categories: classical ferroelectrics ($BaTiO_3$, $PbTiO_3$), relaxors ($PbSc_{1/2}Nb_{1/2}O_3$, $PbMg_{1/3}Nb_{2/3}O_3$) and diffuse phase transition type materials ($BaTi_xSn_{1-x}O_3$) [12, 13].

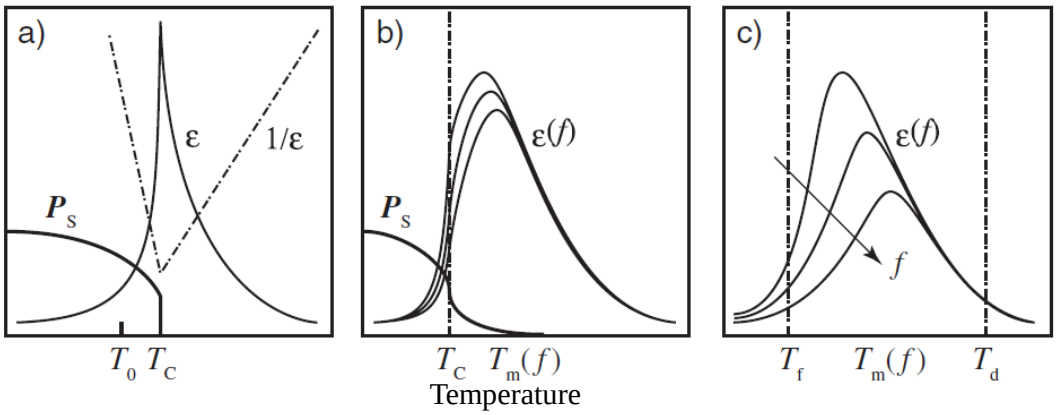

Figure 2-9 Schematic temperature dependence of the real dielectric permittivity and spontaneous polarization (P_S) for (a) first-order ferroelectrics, (b) ferroelectrics with a diffuse phase transition and (c) typical relaxors. This figure is taken from the article by Hirota et al. [14].

2.4.0.5 Experimental set-up

In this thesis, dielectric measurements are used mainly to determine the temperature-dependent structural phase transitions for different solid solutions and their variations as a function of composition. In addition, the height and the sharpness of the weak-field relative dielectric permittivity peak provided quantitative measure of the quality and homogeneity of the samples [15]. The dielectric constant (ε') and the loss (ε'') were obtained from the measurement of capacitance and conductance of the unpoled disc-shaped powders samples. The data were collected using a HP4291A impedance analyzer. Figure 2-10 shows the custom-made set-up for the temperature dependent measurement. Temperature-dependent data for different values of the frequency were recorded via a Labview reference interface. Data were collected in the temperature range 30 - 600 °C during both heating and cooling with a temperature interval of 1 °C between measurements.

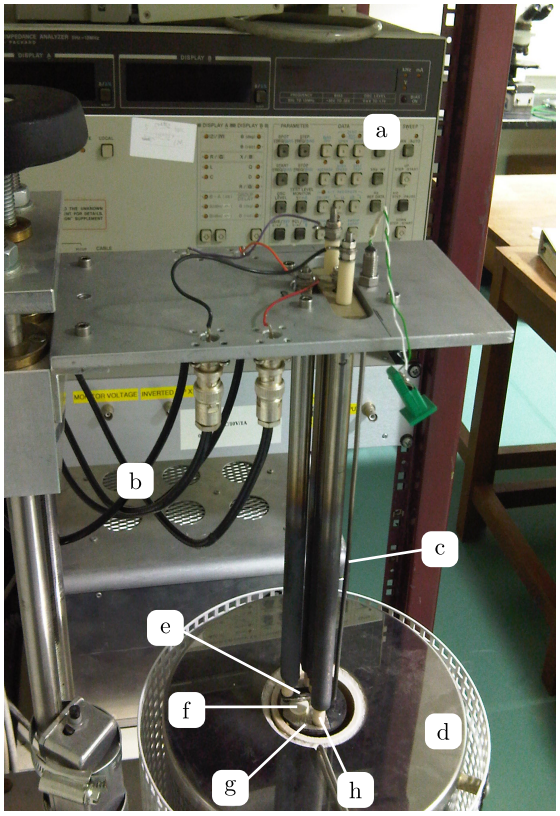

Figure 2-10 Experimental set-up for measurement of dielectric properties. The labels identify the various parts of the total arrangement consisting (a) the HP 4291 low-frequency (100Hz-13MHz) impedance analyzer; (b) four 1 meter long BNC cables (c) thermocouple (d) furnace (e) top platinum electrode (f) sample in the form of a thin pellet, (g) bottom platinum electrode, (h) ceramic tubes to prevent short circuit (Courtesy: D. Keeble).

References

[1] C. N. R. Rao and J. Gopalakrishnan, *New directions in the solid state chemistry* (Cambridge University Press, 1986).

[2] R. E. Newnham, *Properties of materials* (Oxford University Press, 2005).

[3] A. Clearfield, J. Reibenspies, and N. Bhuvanesh, eds., *Principles and Applications of Powder Diffraction* (Wiley, 2008).

[4] R. E. Dinnerbier and S. J. L. Billinge, eds., *Powder Diffraction: Theory and Practice* (RSC Publications, 2008).

[5] E. H. Kisi and C. J. Howard, *Applications of Neutron Powder Diffraction* (Oxford University Press, 2008).

[6] E. Prince, ed., *International Tables for Crystallography: Vol C* (Kluwer Academic Publishers, 2004).

[7] `http://www.isis.stfc.ac.uk/instruments/hrpd/hrpd.html`.

[8] `http://wwwisis2.isis.rl.ac.uk/disordered/gem/gem_home.htm`.

[9] H. M. Rietveld, J. Appl. Cryst. **2**, 65 (1969).

[10] R. A. Young, *The Rietveld Method* (Oxford Science Publications, 1996).

[11] R. Cohelo, *Physics of Dielectrics* (Elsevier, 1979).

[12] A. A. Bokov and Z. G. Ye, J. Mater. Sci. **41**, 31 (2006).

[13] G. A. Samara, J. Phys.: Condens. Matter **15**, R367 (2003).

[14] K. Hirota, S. Wakimoto, and D. E. Cox, J. Phys. Soc. Jpn. **75**, 111006 (2006).

[15] M. E. Lines and A. M. Glass, *Principles and Applications of Ferroelectrics and Related Materials* (Clarendon Press, Oxford, 1979).

Chapter 3

Structural Investigations of xBiScO$_3$-(1-x)PbTiO$_3$

3.1 Introduction

Although $PbTiO_3$ (PT) itself is not a commercially popular piezoelectric material, PT-based materials, mainly as solid solutions, are used extensively as piezoelectric materials because of their superior physical properties. The primary aim of adding dopants to PT is to increase its mechanical strength and to enhance electrical resistivity. The most interesting dopant discovered so far is $PbZrO_3$, which is however not piezoeletric itself. But it has been seen that the solid solution of $Pb(Zr_{1-x}Ti_x)O_3$ (PZT) exhibits excellent piezoeletric properties, especially for the composition about $x = 0.48$. Following the development of PZT, many Pb-based materials with general formulas $Pb(B'B'')O_3$ and $Pb(B'B'')O_3$–$PbTiO_3$ [1] have been investigated and found to be attractive candidates for industrial use. The hunt for novel materials also gave rise to so-called relaxor ferroelectrics such as (1-x)$Pb(Zn_{1/3}Nb_{2/3})O_3$-$x$$PbTiO_3$ [2], (1-x)$Pb(Mg_{1/3}Nb_{2/3})O_3$-$x$$PbTiO_3$ [3] and (1-x)$Pb(Sc_{1/2}Nb_{1/2})O_3$-$x$$PbTiO_3$ [4]. However, recent environmental concern over the toxicity of lead has increased the need to look for reduced-lead or lead-free materials with properties approaching that of PZT. In this context, Eitel et al. [5] first developed the reduced-lead solid solutions of $x$$BiScO_3$-(1-$x$)$PbTiO_3$ (BS-PT) which exhibited excellent piezoelectric properties near the phase boundary [6] compared to PZT.

Several studies have so far been made on BS-PT ceramics [5–12], single crystals [13–17] as well as thin films [18–22] revealing its excellent ferroelectric and piezoelectric properties. The ceramics were first characterized by Eitel et al. [5, 6] who reported a phase boundary at $x = 0.64$ with an unusually favourable combination of physical properties (T_c= 450 °C, d_{33} = 460pC/N, $\kappa_p = 0.56$). Additionally, at some specific composi-

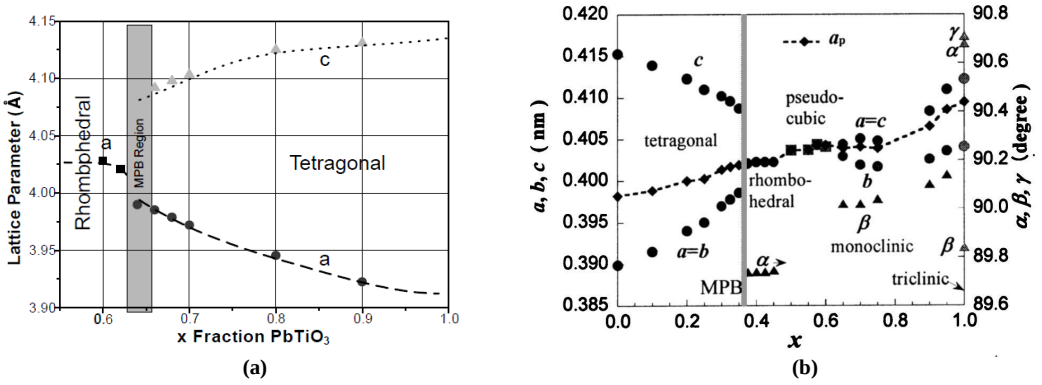

Figure 3-1 Phase diagrams reported earlier for BS-PT systems (a) by Eitel et al. [5] and (b) by Inaguma et al. [10]

tions BS-PT exhibited a higher ferroelectric to paraelectric transition temperature (T_c) than the end member $PbTiO_3$ and in general the T_c is at least 100°C higher than the PZT. Shimojo et al. [7] published the phase diagram of the same system with a tetragonal to rhombohedral phase boundary located at x = 0.375 and from studying the dielectric properties, it was suggested that the percolation of ScO_6 octahedra plays an important role in the dielectric response of the materials. Later on the phase diagram near the symmetry change was revised by Eitel et al. [9] using variable-temperature electron diffraction, which came to two principal conclusions: (1) the existence of octahedral-tilt phase transitions for x = 0.60 as a function of temperature leading to a curvature of the phase boundary above 300 °C and (2) a plausible suggestion for the existence of a lower symmetry phase along with the tetragonal or rhombohedral phase near the phase boundary.

The solid solution of BS-PT is notable for two reasons. Firstly, unlike most $PbTiO_3$-based solid solutions both the A and B sites of the perovskite are randomly occupied in the average long-ranged crystal structure and secondly, although this system has a composition-dependent structural phase transformation from tetragonal (pure $PbTiO_3$) to rhombohedral, the structure of $BiScO_3$ itself is of a completely different symmetry. $BiScO_3$ has been studied independently [23] and reported to be a centro-symmetric monoclinic system . However, when the complete phase diagram of xBiScO$_3$-(1-x)PbTiO$_3$ was reported by Inaguma et al. [10] through the high pressure synthesis of the ceramics for $x > 0.55$, the structure of $BiScO_3$ was suggested to be of triclinic symmetry.

Investigations have also been carried out [24–31] in order to improve the piezoelec-

tric properties of BS-PT by combining it with other compounds or by B-site substitutions and it has been found that the mechanical quality factor of this solid solution is substantially improved when combined with $PbMn_{1/3}Nb_{2/3}O_3$ [25] . As mentioned before, in addition to polycrystalline ceramics, BS-PT single crystals of tetragonal phase [13, 16], rhombohedral phase [14, 15] and with the MPB composition [17] have been investigated and found to be promising candidates for high temperature actuators and sensors applications. In particular, Zhang et al. [17] reported high piezoelectric properties ($d_{33} \sim 900$pC/N) of BS-PT single crystals at the MPB ($x = 0.64$) and also suggested monoclinic symmetry for the unit cell ($a = 4.0751$ Å, $b = 3.9765$ Å, $c = 3.9893$ Å and $\beta = 90.166°$) with space group Pm on the basis of indexing the diffraction pattern recorded at room temperature. A recent study carried out by Chaigneau et al. [12] claimed that the most efficient route of synthesis of BS-PT ceramics is the freeze-drying processing rather than the traditional mixed oxide route and also revealed evidence of phase coexistence at the MPB.

The focus of this work is to examine the details of structures of BS-PT using neutron and x-ray diffraction and thus to elucidate how the doping influences the structure and properties. It will be shown that Rietveld refinement of the diffraction profile indicates that the phase boundary of this solid solution is a mixture of two phases (tetragonal+monoclinic structure). High-temperature dielectric measurements will evidence the quality of the ceramics and establish the variation of the Curie temperature as a function of doping.

3.2 Experimental

3.2.1 Synthesis and physical characterization

Solid-state ceramic synthesis was used to prepare the BS-PT solid solutions. The starting materials were commercial reagent grade PbO (Alfa Aesar), TiO_2 (Alfa Aesar), Bi_2O_3 (Alfa Aesar), and Sc_2O_3 (Metall Rare Earth Ltd., China) having $\sim 99.9\%$ purity. The amount of starting materials for different stoichiometric ratio of the samples were

calculated from the following equations :

$$Bi_2O_3 + Sc_2O_3 = 2BiScO_3 \quad (3\text{-}1)$$

$$PbO + TiO_2 = PbTiO_3 \quad (3\text{-}2)$$

Stoichiometric quantities of oxides were mixed by wet ball milling for about 24 hrs to ensure homogeneous mixing of the reactants at the atomic level. The mixture was then dried out and calcined at 1000 °C for 4hrs in a sealed platinum crucible to achieve the desired perovskite phase. The resulting powders were uniaxially pressed into pellets of diameter ~ 1.4 cm and were sintered at 1100 °C for 2hrs to achieve maximum density while minimizing the weight loss [6]. Since the starting materials consist of two highly volatile oxides (PbO, Bi_2O_3), it was found that instead of two steps of calcination [7], which incur a substantial amount of weight loss as well as change in the compositional ratio of the constituents in the solid solution, a single stage of calcination with a slow heating and cooling rate (approximately 1-2 °C per minute) provided the most favourable conditions for synthesis of high-quality ceramics with the desired compositions. For electrical characterization, the smooth parallel faces of the pellets were painted using silver paste and left at 200 °C for several hours to dry. High-temperature dielectric measurements were carried out in a furnace between room temperature and 650 °C using a HP4192A impedance analyzer. The micro-structures of the BS-PT ceramics were investigated by scanning electron microscope (ZEISS SUPRA 55-VP) and their compositions were verified by energy dispersive x-ray analysis (EDX).

3.2.2 X-ray powder diffraction

High resolution x-ray powder diffraction on BS-PT ceramics was performed utilizing a PANalytical X'Pert Pro MPD equipped with a curved Johansson monochromator giving focussed pure Cu$K_{\alpha 1}$ radiation, axial divergence controlled by a 0.02rad soller slit in the diffracted beam. Data were collected using pixcel detector (active length = 3.347° in 2θ) with step size of 0.013° in the 2θ range of 20° - 90° in Bragg-Brentano geometry.

3.2.3 Neutron powder diffraction

Neutron powder diffraction scans (time of flight data) were collected at the ISIS facility using the GEM diffractometer. Approximately 16 g of powder were loaded into a

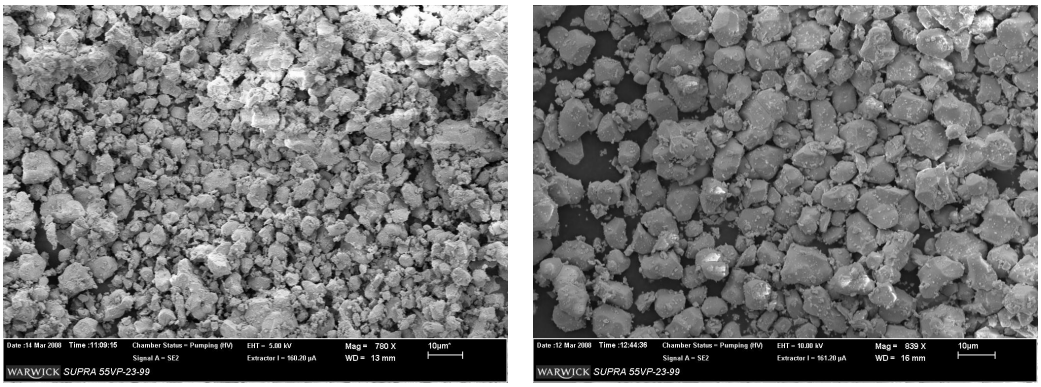

Figure 3-2 Morphology of the BS-PT ceramics with compositions x =0.30 (left) and x = 0.34 (right).

cylindrical vanadium can and data collected for a total count of 200 μA of current. Data from all six banks were used for Rietveld refinement.

3.3 Results and discussions

3.3.1 Structural investigation

3.3.1.1 Ambient x-ray powder diffraction

Room temperature x-ray diffraction patterns were collected for 14 different compositions of BS-PT ceramics between x = 0.05 and 0.40. The compositionally-driven structural phase transition is evident from figure 3-3 which shows the x-ray patterns for BS-PT ceramics as a function of composition in the 2θ range of 20° to 85°. Figure 3-4 demonstrates precisely the development of {200} and {210} Bragg reflections as a function of x. A gradual structural phase transition is evident and the occurrence of phase-mixing can be seen in the region $0.36 \leq x \leq 0.38$. A single perovskite phase was confirmed for all compositions from the x-ray scans, however, the presence of a small percentage of Bi and Pb-based pyrocholore phases was identified for the samples with $x \geq 0.36$ (fig 3-5).

3.3.1.2 Ambient neutron powder diffraction

Both x-ray and neutron diffraction data in the tetragonal region ($x \leq 0.35$) showed only peaks that could be indexed using a pseudocubic unit cell of side ~ 4 Å. There was

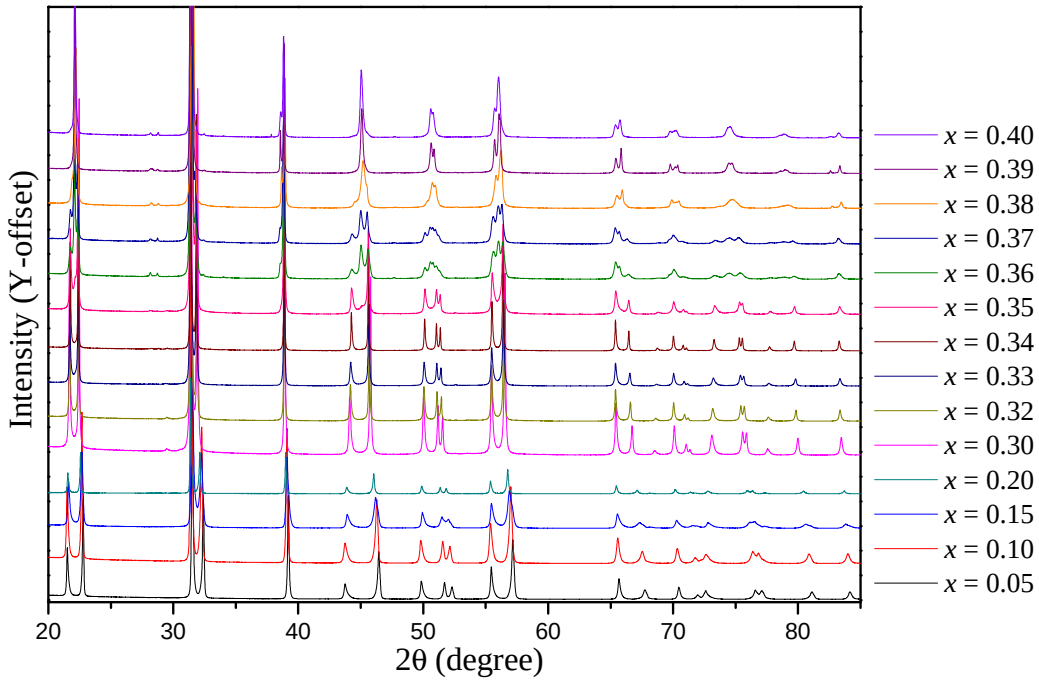

Figure 3-3 Room temperature x-ray diffraction patterns for xBS-(1-x)PT ceramics as a function of composition.

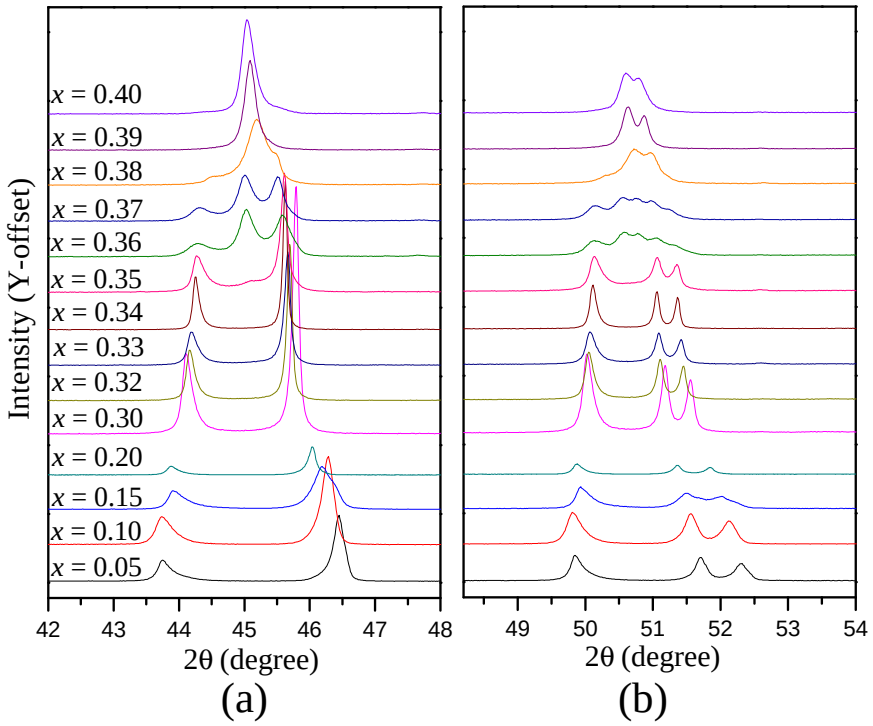

Figure 3-4 Transformation of (a) {200} and (b) {210} Bragg peaks suggesting a structural phase transition driven by composition.

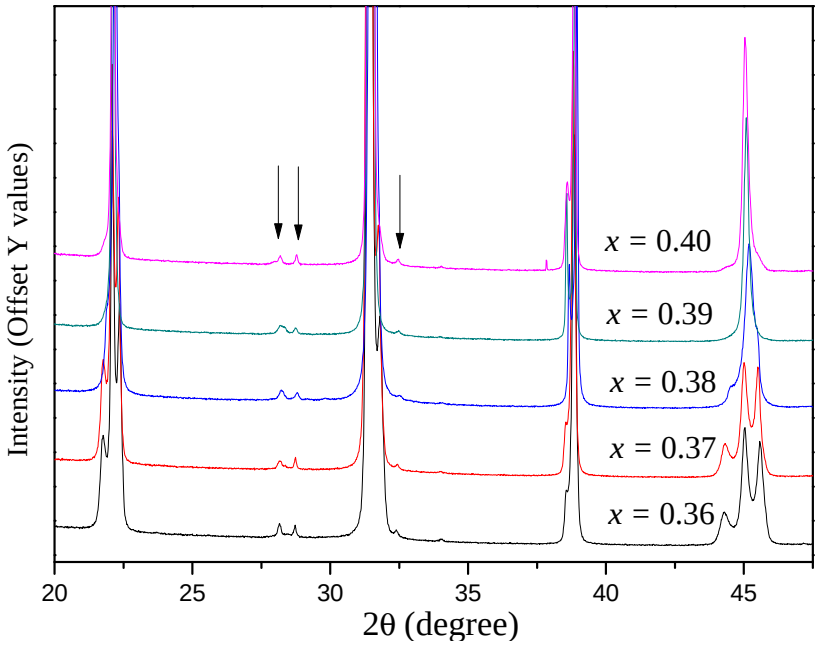

Figure 3-5 Evidence of undesired phases for the samples with compositions $x \geq 0.36$. The arrows indicate the peaks which are not from the primary perovskite.

no evidence of cell doubling either because of oxygen-octahedral tilting or cation ordering. Therefore it is seen that the tetragonal phase of the BS-PT solid solution is untilted. The phases were assumed to be polar and the starting structure was taken to be that of $PbTiO_3$ [32] with Bi and Sc added proportionally to the composition on the A and B sites, respectively. The refinements were carried out using the GSAS package. Various crystallographic parameters along with the background function, an 8th-order Chevishev polynomial, were refined while the instrumental parameters obtained from a standard Y_2O_3 scan were kept fixed. To model the peak shape TOF profile function 2 (as defined by the GSAS manual) was used and the starting values were obtained from the standard Y_2O_3 scan. Data from all six banks of the GEM detector were refined together.

For the compositions $0.10 \leq x \leq 0.35$, a single tetragonal phase was used to model the structure. The coordinates of the ions in the tetragonal phase were described in the following way, assuming the Pb and Bi ions are at the origin : Pb/Bi (0, 0, 0), Ti/Sc (1/2, 1/2, 1/2+δz_1), O1 (1/2, 1/2, δz_2), O2 (1/2, 0, 1/2+δz_3) and (0, 1/2, 1/2+δz_4). The δz's are refinable quantities which give the shifts of the ions from the special positions in an ideal cubic structure. Refinements were started with isotropic values of thermal

displacement parameters, however in later refinements, anisotropic values (ADP) were assumed which provided better values of the goodness of fit (GOF). Since Bi and Sc were constrained to the same values of coordinates as Pb and Ti, respectively, they were also constrained with same values of thermal displacement parameters. It should be mentioned that the ADP's for Ti/Sc ions were sometimes refined to negative values. To recover from this problem the Sc and Ti sites were allowed to refine independently, but no improvement to the fit was gained and finally, these ions were assigned with equivalent isotropic displacement parameters. The site occupancies for different compositions of samples were also refined and these were consistent with the known compositions. The changes in the lattice parameters because of the doping resulted in a decrease of the tetragonal axial ratio with increasing x (fig 3-6). However, it is evident from the Ti-O1 bond lengths that the for composition $x = 0.20$ the Ti shift from its ideal position (which is half of the difference between two Ti-O1 bond lengths) reaches a maximum and after that it drops with the increase of x. This non-linear displacement also suggests the existence of non-linear values of the spontaneous polarization in the unit cell. This is crucial because from the dielectric measurements it will be shown that there exists a non-linear dependence of the ferroelectric Curie-temperature on the composition and the maximum occurs between $x = 0.10$ and 0.20. Therefore it can be anticipated that there is linear coupling between these parameters but, since we do not have structural data at points between x =0.10 and 0.20, the exact correlation cannot be confirmed. Table 3-1 shows the details of the refined crystallographic parameters obtained from the refinements for all seven compositions with a tetragonal model.

Phase coexistence was evident for the compositions $x = 0.36$, 0.37 and 0.38. This is the region which has been described as a MPB between the tetragonal and the rhombohedral phases similar to PZT. Initially, the pattern for $x = 0.37$ was subjected to indexing which provided monoclinic solutions with both primitive and c-centered unit cells. However, the refinement assuming a single monoclinic phase was unsuccessful. It was seen there are two different two-phase models which can give refinement for the phases in this compositional range : (1) $P4mm + R3m$ and (2) $P4mm + Cm$. This agrees with the results published by Chaigneau et al. [12]. However, based on the observation of various refined parameters as well as values of R-factors, it was understood that the best model to represent the structure in the MPB region is $P4mm + Cm$.

Needless to say, it is very difficult to assign the space groups absolutely based on the one dimensional powder diffraction data. A comprehensive single crystal investigation could provide better insight and unequivocal solutions. Table 3-2 provides the details of the refinement results obtained for the samples with x = 0.36, 0.37 and 0.38 assuming a two-phase model consisting of $P4mm + Cm$. Isotropic thermal displacement parameters had to be used because anisotropic refinements were not stable.

The structure for $x \geq 0.39$ is considered to be the composition beyond the MPB and the accepted symmetry in this region is rhombohedral. The space group was determined to be $R3m$ since there was no evidence of octahedral tilting in either the x-ray or neutron diffraction patterns which, however, is in contradiction with the electron diffraction study by Eitel et al. [9] where the space group $R3c$ was suggested for the rhombohedral phase with tilting. The refinements assuming a $R3m$ model converged to a reasonable fit with sensible values of different R-factors. However the ADP's of the Pb and Bi atoms were highly anisotropic and are in the form of discs with the smallest parameter being in the [111] pseudocubic direction.

This exactly mimics the findings of Corker et al. [33] for PZT, where refinement of neutron diffraction data gave disk-like ADP's for Pb in the rhombohedral side of the MPB. Corker et al. modelled this by disordering the Pb atoms perpendicular to the [111] axis, thus refining the Pb site as effectively monoclinic within a structure of average rhombohedral symmetry. Subsequently Noheda et al. [34] have identified a phase of long-range monoclinic symmetry and Pandey et al. [35] refined compositions far into the 'rhombohedral' side of the phase diagram as monoclinic. Therefore a monoclinic model with space group Cm was employed to refine structures of two samples with x = 0.39 and 0.40. Interestingly, better values of R-factors with stable and sensible values of ADP's were achieved for both the compositions. Table 3-3 presents all the crystallographic parameters obtained from both the refinements assuming a rhombohedral and a monoclinic structure for comparison.

3.3.1.3 High temperature x-ray powder diffraction

High temperature x-ray powder diffraction experiments were performed for BS-PT ceramics to demonstrate the temperature-driven structural phase transition as a function of composition. Powder scans were recorded in the temperature range between 25 and

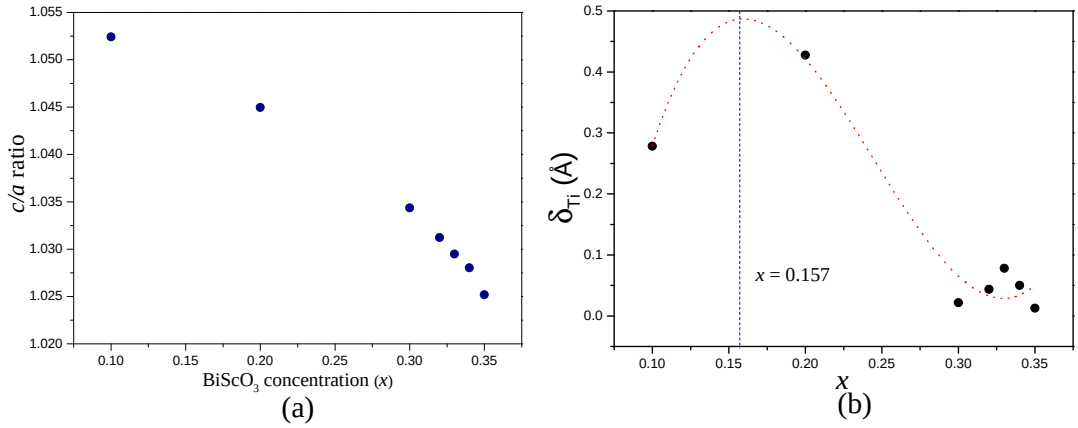

Figure 3-6 (a)Variation of tetragonal axial ratio BS-PT samples for $x \leq 0.35$. Error bars are too small to be visible on the given scale. (b) This shows the Ti-displacement as a function of composition in the tetragonal regime of the phase diagram. A 3rd-order polynomial has been fitted in order to visualize the possible non-linear relationship between them, which provided an apparent maximum at $x \sim 0.16$.

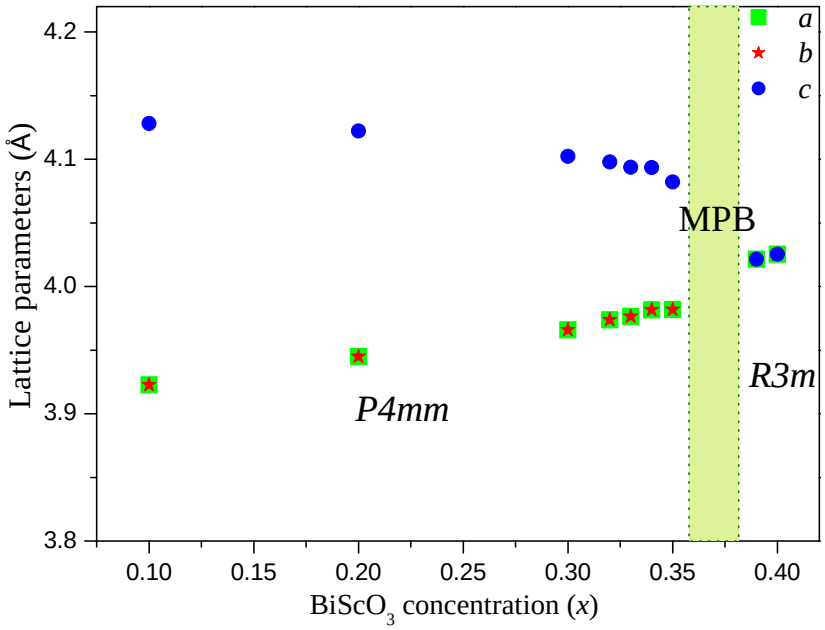

Figure 3-7 The lattice parameters obtained from the refinements of the BS-PT system as a function of composition. The MPB has been shown in the region of composition between $x = 0.36$ and 0.38. Rhombohedral lattice parameters are shown for compositions $x = 0.39$ and 0.40, however these phases can also be well refined by a single monoclinic model (*Cm*).

Table 3-1 Refined crystallographic data for $x\mathrm{BiScO_3}(1-x)\mathrm{PbTiO_3}$ ceramics for $0.10 \leq x \leq 0.35$ at room temperature.

$BiScO_3$ content	$x = 0.10$	$x = 0.20$	$x = 0.30$	$x = 0.32$	$x = 0.33$	$x = 0.34$	$x = 0.35$
Space group				*P4mm*			
$a = b$ (Å)	3.92252(4)	3.94493(3)	3.96594(3)	3.97379(4)	3.97646(7)	3.98173(3)	3.98177(8)
c (Å)	4.12810(6)	4.12228(5)	4.10223(6)	4.09788(6)	4.0937(1)	4.09336(5)	4.0820(1)
Cell volume	63.516(2)	64.153(1)	64.523(1)	64.710(2)	64.730(3)	64.897(1)	64.719(4)
Pb/Bi (0,0,0)							
U11=U22 (Å^2)	0.01081	0.01654	0.02227	0.02483	0.0263(5)	0.0265(0)	0.02236
U33 (Å^2)	0.01082	0.01654	0.02227	0.02483	0.0263(5)	0.0264(0)	0.02236
Sc/Ti(0.5,0.5,z)	0.536(0)	0.499(0)	0.590(0)	0.583(0)	0.579(1)	0.5801(0)	0.5863(0)
U (isotropic) (Å^2)	-0.00178	-0.00825	0.02177	0.0159	0.01642(1)	0.01311	0.01696
O1 (0.5,0.5,z)	0.103(0)	0.103(0)	0.096(0)	0.095(0)	0.0984(6)	0.0923(0)	0.0832(0)
U11=U22 (Å^2)	0.0104	0.01458	0.02128	0.02519	0.023(1)	0.03005(1)	0.03312
U33 (Å^2)	0.0153	0.01337	0.01219	0.01185	0.017(1)	0.01(0)	0.01885
O2 (0.5,0,z)	0.613(0)	0.617(0)	0.6142(0)	0.6137(0)	0.6135(4)	0.6126(0)	0.6034(0)
U11 (Å^2)	0.00906	0.01563	0.02534	0.02775	0.034(1)	0.03227	0.03373
U22 (Å^2)	0.00328	0.00377	0.00561	0.00517	0.0046(8)	0.00571	0.00802
U33 (Å^2)	0.0176	0.01574	0.01908	0.0196	0.0153(7)	0.02047	0.02859
Sc/TiO1a (Å)	1.78594(3)	1.63348(2)	2.02944(3)	2.00514(3)	1.969(5)	1.99675(2)	2.05371(6)
Sc/TiO1b (Å)	2.34216(3)	2.48880(3)	2.07280(3)	2.09274(3)	2.125(5)	2.09661(3)	2.02833(6)
Sc/TiO2 (Å)	1.98707(2)	2.03196(2)	1.98531(2)	1.99063(2)	1.9931(3)	1.99529(2)	1.99211(4)
R_{wp}	5.25	4.28	4.18	4.19	6.68	3.80	6.42
GOF	5.80	4.94	5.25	5.18	8.22	5.34	7.45

Table 3-2 Refined crystallographic data for xBiScO$_3$(1 − x)PbTiO$_3$ ceramics for $0.36 \leq x \leq 0.38$ at room temperature.

BiScO$_3$ content		x = 0.36		x = 0.37		x = 0.38	
Space group		*P*4*mm*	*Cm*	*P*4*mm*	*Cm*	*P*4*mm*	*Cm*
Phase fraction (%)		50.6	49.4	50.5	49.5	34.7	65.3
a (Å)		3.97816(9)	5.6957(4)	3.98454(9)	5.6969(3)	3.9955(2)	5.6887(2)
b (Å)		3.97816(9)	5.6674(4)	3.98454(9)	5.6703(4)	3.9955(2)	5.6627(2)
c (Å)		4.0873(2)	4.0400(2)	4.0826(2)	4.0398(2)	4.0632(4)	4.0312(1)
β (°)		90.0	90.410(5)	90.0	90.428(4)	90.0	90.466(3)
Bi/Pb	U_{iso} (Å^2)	0.04296(0)	0.04191(0)	0.04654(1)	0.04775(0)	0.0632(0)	0.03435(0)
Sc/Ti	x	0.5	0.5346(0)	0.5	0.5347(0)	0.5	0.5395(0)
	y	0.5	0.0	0.5	0.0	0.5	0.0
	z	0.4585(0)	0.4438(0)	0.4651(0)	0.4365(0)	0.46134(0)	0.4464(0)
	U_{iso} (Å^2)	0.0789(0)	-0.0068(0)	0.0426(0)	-0.0038(3)	0.07513(0)	0.00246(0)
O1	x	0.5	0.5579(0)	0.5	0.55461(0)	0.5	0.5504(0)
	y	0.5	0.0	0.5	0.0	0.5	0.0
	z	-0.1032(0)	-0.0523(0)	-0.1006(0)	-0.04098(0)	-0.0909(0)	-0.06752(0)
	U_{iso} (Å^2)	0.0789(0)	0.0190(0)	0.01798(0)	0.0154(0)	0.00937(0)	0.01455(0)
O2	x	0.5	0.3153(0)	0.5	0.3192(0)	0.5	0.30536(0)
	y	0.0	0.2676(0)	0.0	0.2677(0)	0.0	0.26548(0)
	z	0.5190(0)	0.4253(0)	0.5262(0)	0.4262(0)	0.5351(0)	0.42075(0)
	U_{iso} (Å^2)	0.01646(0)	0.0202(0)	0.0173(0)	0.0231(0)	0.02434(0)	0.02342(0)
Sc/TiO1a (Å)		2.29597(9)	2.00972(8)	2.30963(8)	1.93312(8)	2.2439(2)	2.07343(6)
Sc/TiO1b (Å)		1.79131(7)	2.03904(9)	1.77299(7)	2.11306(8)	1.8193(2)	1.95971(6)
Sc/TiO2a (Å)		2.00441(5)	1.9658(1)	2.00783(5)	1.95270(9)	2.0201(1)	2.01092(5)
Sc/TiO2b (Å)			2.0732(1)		2.08901(9)		2.01566(5)
R_{wp}		4.30		3.85		3.87	
GOF		5.74		5.10		5.26	

Table 3-3 Refined crystallographic data for xBiScO$_3$(1 − x)PbTiO$_3$ ceramics for x = 0.39 and 0.40 at room temperature.

BiScO$_3$ content		x = 0.39		x = 0.40	
Space group		*R*3*m*	*Cm*	*R*3*m*	*Cm*
a (Å)		4.02142(5)	5.6936(2)	4.02534(8)	5.6965(3)
b (Å)		4.02142(5)	5.6666(2)	4.02534(8)	5.6732(2)
c (Å)		4.02142(5)	4.0321(1)	4.02534(8)	4.0370(1)
β (°)		89.7011(8)	90.448(2)	89.747(2)	90.379(2)
Bi/Pb	x	0.5	0.0	0.5	0.0
	y	0.5	0.0	0.5	0.0
	z	0.5	0.0	0.5	0.0
	U11 (Å^2)	0.0265(1)	0.0372(0)	0.0286(0)	0.0391(0)
	U12 (Å^2)	-0.0029(1)	0.0	-0.0057(0)	0.0
	U13 (Å^2)	-0.0029(1)	0.0042(0)	-0.0057(0)	0.0038(0)
	U22 (Å^2)	0.0265(1)	0.0372(0)	0.0286(0)	0.0391(0)
	U23 (Å^2)	-0.0029(1)	0.0	-0.0057(0)	0.0
	U33 (Å^2)	0.0265(1)	0.0372(0)	0.0286(0)	0.0391(0)
Sc/Ti	x	0.0467(0)	0.55197(0)	0.0519(3)	0.5446(0)
	y	0.0467(0)	0.0	0.0519(3)	0.0
	z	0.0467(0)	0.46149(0)	0.0519(3)	0.4549(0)
	U11 (Å^2)	0.0129(3)	0.0048(0)	0.00481(0)	0.0014(0))
	U12 (Å^2)	0.0003(3)	0.0	0.0	0.0
	U13 (Å^2)	0.0003(3)	0.0	0.0	0.00074(0)
	U21 (Å^2)	0.0129(3)	0.0048(0)	0.00481(0)	0.0014(0)
	U23 (Å^2)	0.0003(3)	0.0	0.0	0.0
	U33 (Å^2)	0.0129(3)	0.0048(0)	0.00481(0)	0.0014(0)
O1	x	0.5512(0)	0.5412(0)	0.5435(3)	0.55461(0)
	y	0.0665(0)	0.0	0.0554(2)	0.0
	z	0.0665(0)	-0.0617(0)	0.0554(2)	-0.04098(0)
	U11 (Å^2)	0.0129(4)	0.0627(0)	0.01056(0)	0.07298(0)
	U12 (Å^2)	-0.0014(3)	0.0	0.00632(0)	0.0
	U13 (Å^2)	-0.0014(3)	-0.0036(0)	0.00632(0)	0.00839(0)
	U21 (Å^2)	0.0283(3)	0.0269(0)	0.03963(0)	0.02756(0)
	U23 (Å^2)	0.0005(4)	0.0	0.00928(0)	0.0(3)
	U33 (Å^2)	0.0283(3)	0.0205(0)	0.03963(0)	0.00727(0)
O2	x		0.3015(0)		0.2983(0)
	y		0.2586(0)		0.2577(0)
	z		0.4118(0)		0.4080(0)
	U11 (Å^2)		0.0095(0)		0.02323(0)
	U12 (Å^2)		0.00038(0)		0.00464(0)
	U21 (Å^2)		0.00841(0)		0.00079(0)
	U22 (Å^2)		0.01204(0)		0.01467(0)
	U31 (Å^2)		0.00033(0)		0.00623(0)
	U33 (Å^2)		0.03086(0)		0.03096(0)
R_{wp}		4.12	4.03	6.29	5.12
GOF		5.61	5.52	8.50	6.92

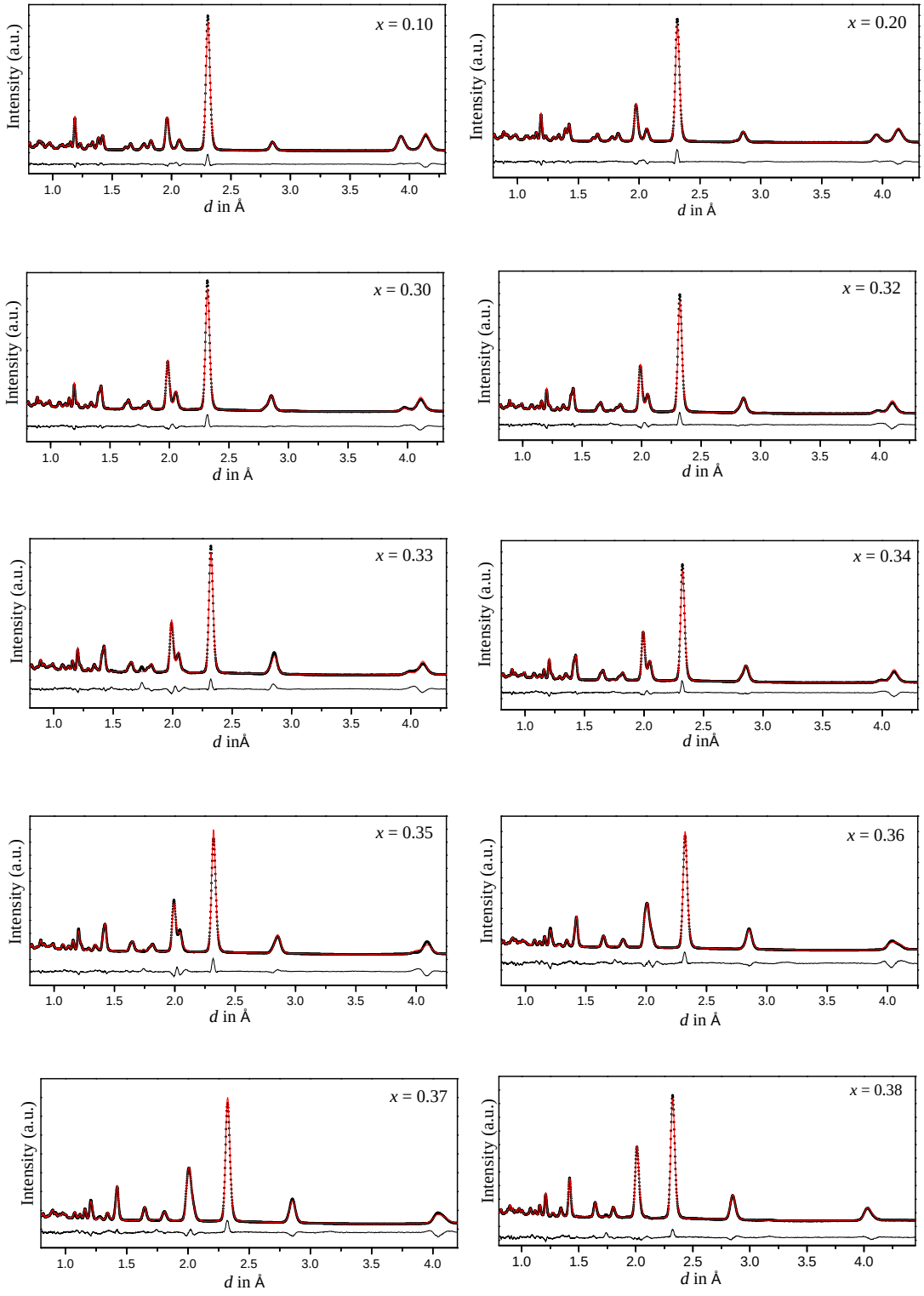

Figure 3-8 Observed (•), calculated (-) and difference (-) plots for room-temperature neutron diffraction patterns of BS-PT samples as a function of composition. The data are from the 90° bank of the GEM detector.

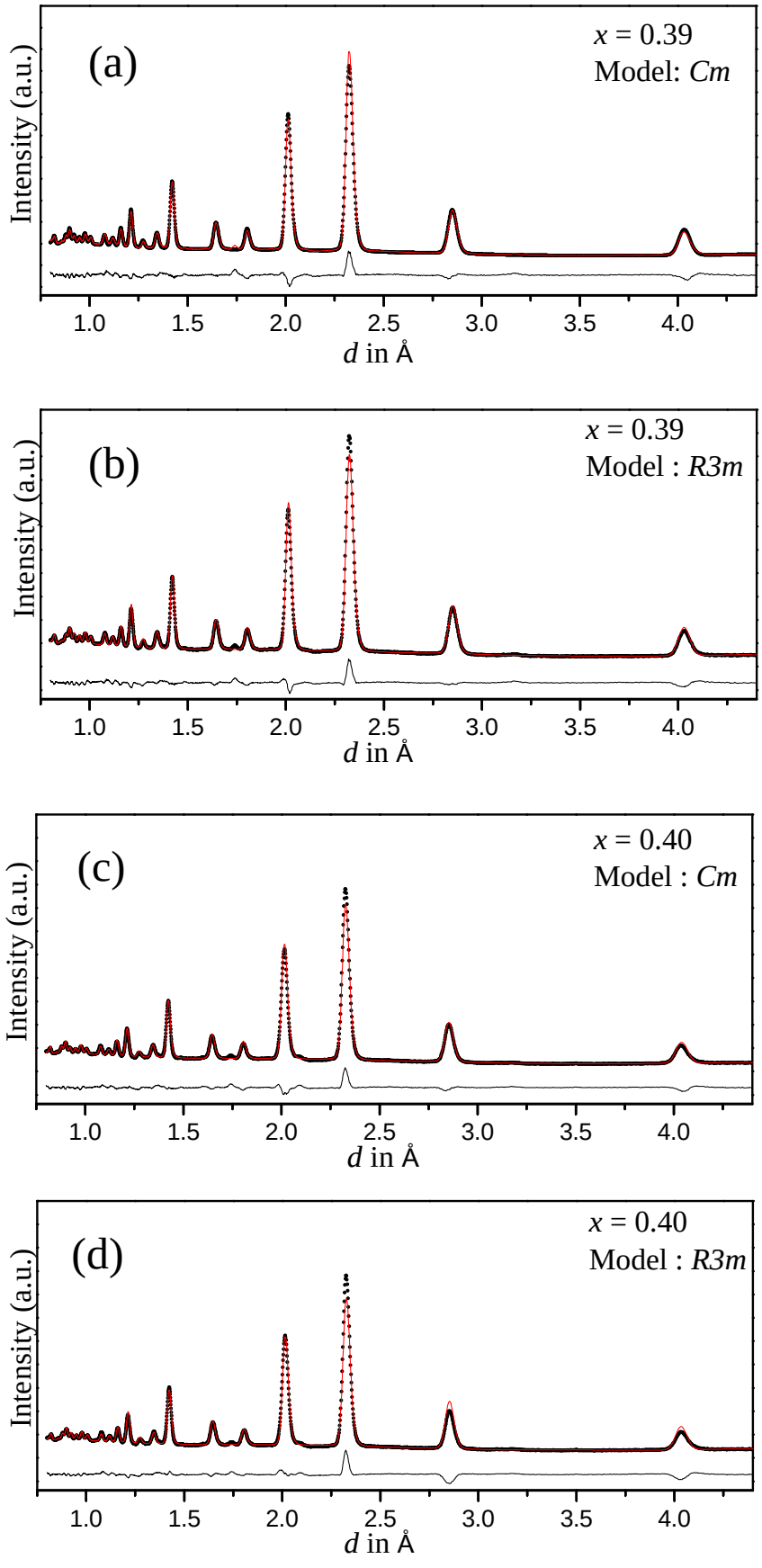

Figure 3-9 Observed (•), calculated(-) and difference (-) plots for x = 0.39 and 0.40. The data are from the 90° bank of the GEM detector.

600 °C with an average interval of 20 °C. Figure 3-10 shows the phase transition as a function of temperature for $x = 0.10$. From the change in the {200} Bragg reflection, a gradual phase transition is evident. The high-temperature phase is a non-polar cubic phase. The pattern at 600 °C was modelled with a $Pm\bar{3}m$ structure and lattice parameters were $a = b = c = 3.9882(9)$Å.

Figure 3-11 shows the temperature-driven phase transition for the composition $x = 0.39$. It has been seen from the room-temperature powder diffraction data that this particular composition is better fitted with a monoclinic crystal structure although the accepted model had been a rhombohedral structure. To show further evidence against the rhombohedral symmetry, we focus on the {200} Bragg reflection which is a singlet for $R3m$ model. Figure 3-12 displays how the {200} Bragg reflection changes as a function of temperature. To account for the changes seen, a single Pseudo-Voigt peak was fitted to the {200} peak to extract the FWHM and the intensity as a function of temperature.The decrease in the FWHM and the increase in the intensity with the increase of temperature can also be seen in fig 3-12b, which suggests that {200} may not be a single peak. This provides crucial information on the symmetry breaking and supports our assumed monoclinic Cm model, for which {200} is indeed a doublet.

Recently a high-temperature neutron diffraction study [36] on BS-PT ceramics especially in the MPB region has been reported and confirmed the presence of a monoclinic phase along with the tetragonal phase. In addition, it was also concluded that the coexistence of monoclinic and tetragonal phases originate from a 'martensitic-type phase transition' which is unstable under the influence of an external electric field.

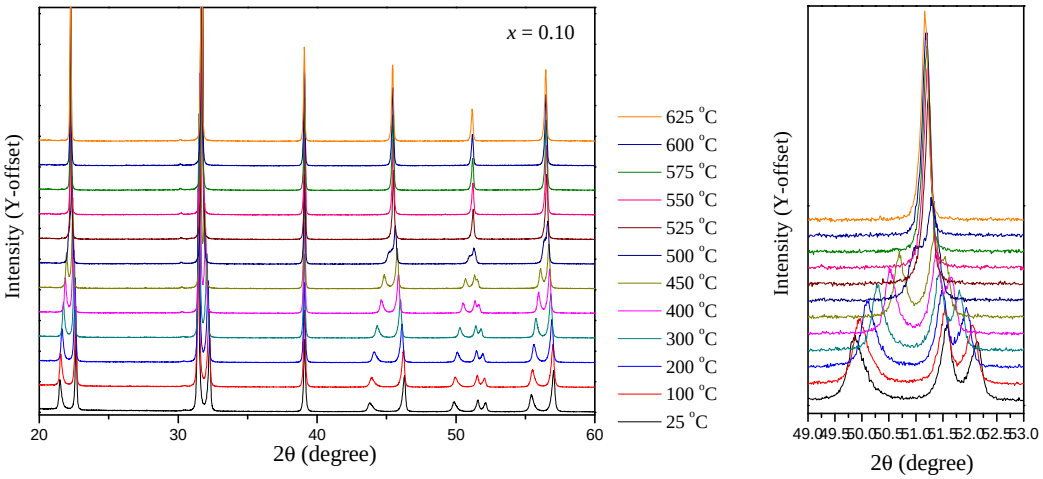

Figure 3-10 Structural phase transition as a function of temperature for x = 0.10. A selected range of 2θ shows the transformation of the {210} Bragg Reflection with the temperature.

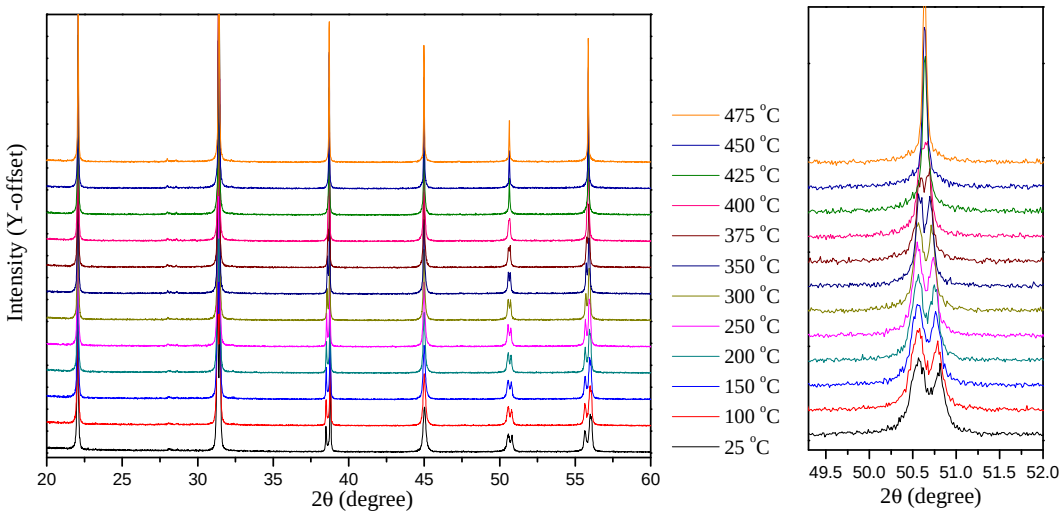

Figure 3-11 Structural phase transition as a function of temperature for x = 0.39. The gradual transformation to the high-temperature cubic phase is also evident from the transformation of the {210} Bragg peak as a function of temperature.

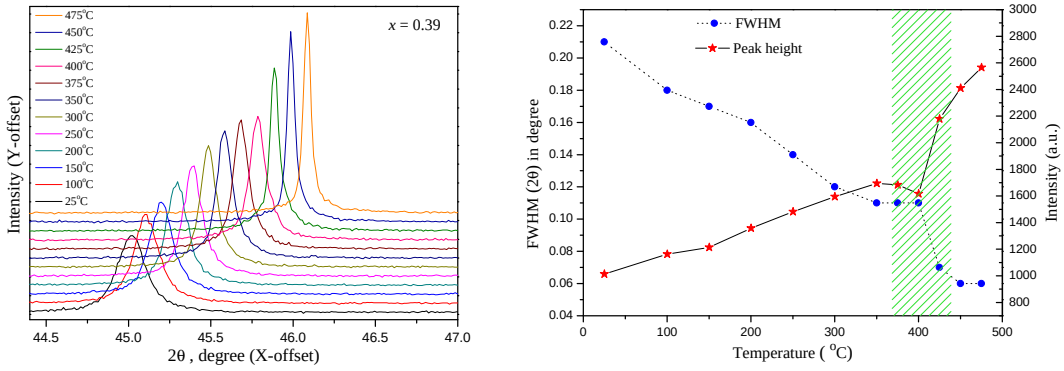

Figure 3-12 Variation of the peak height and FWHM of the {200} Bragg peak for the composition x = 0.39. The x-ray powder scans were taken under identical experimental conditions.

3.3.2 Dielectric properties of BS-PT ceramics

To investigate the physical properties of BS-PT ceramics, temperature- and frequency-dependent capacitance and conductance were measured using disc-shaped sintered ceramics. The real and imaginary parts of the dielectric permittivity were calculated assuming the parallel plate capacitor equations. Both ε' and ε'' as a function of temperature were measured at frequencies 50kHz, 100kHz and 150kHz for 15 different samples with compositions between x = 0.05 and 0.40. For all the samples there was a single peak in the temperature-dependent dielectric constant, which corresponds to the ferroelectric to paraelectric phase transition. This involves a structural phase transition from a polar phase to a non-polar phase (centrosymmetric cubic phase) as seen from the high-temperature x-ray diffraction experiments. The phase transition temperature (T_m) for each composition was estimated from the peak of the dielectric constant versus temperature plot (fig 3-13, 3-15, 3-17). Figure 3-19 shows the variation of the phase transition temperature (T_m) as a function of composition. It is evident from the plot that the phase transition temperature or the Curie temperature exceeds that of undoped PT for $x \leq 0.30$. It reaches a maximum at around x = 0.15 and then drops almost linearly with increasing x. This enhancement in the Curie temperature is an unusual event in the case of PT-based binary solid solutions where normally the Curie temperatures do not exceed that of the pure PT which is approximately 492 °C. However exceptions have only been seen when PT is mixed with other Bi-based compound, for example solid solutions of $BiZn_{2/3}Nb_{1/3}O_3$−$PbTiO_3$ [37], $BiInO_3$-$PbTiO_3$ [38] etc. This suggests that

apart from the structural changes in the system, the presence of Bi ion plays a crucial role in determining the physical properties of the material. The increase of the Curie point has been reasoned by Inaguma et al. [10] as an effect of the Bi-O covalent bond which increases ferroelectric stability. A few other Bi-based systems which demonstrate such non-linear characteristics were studied by Stringer et al. [39] who suggested that the enhancement of the Curie temperature above that of the $PbTiO_3$ could be as a consequence of a coupling between the random electric fields resulting from random strain fields throughout the crystal lattice and the polarization. However, we have found an apparent structural correlation between the Curie temperature and the shift of the Ti/Sc atom from its ideal position in the tetragonal unit cell (fig- 3-6b), which suggests a non-linear value of intrinsic polarization as a function of composition. A comprehensive list of PT-based solid solutions [xABO$_3$+(1-x)PbTiO$_3$] showing non-linearity in T_c as a function of compositions can be also be found in the article by Isupov [40]. Very recently, the non-linear behaviour of T_c in tetragonal BS-PT and corresponding cation displacement have been published by Chen et al. [41] for x = 0.05, 0.15, 0.25 and 0.35. This supports our results and the conclusion regarding a possible correlation between these physical parameters (fig 3-20).

BS-PT ceramics have not demonstrated any significant frequency dispersion in the real part of the dielectric permittivity similar to that found in typical relaxor materials such as PMN-PT. However ε'' for each composition has demonstrated a high frequency dependence especially at high temperatures. This can be attributed as an effect of the high conduction in the samples and because of that the phase transition peaks are inhibited in ε'' vs. T data for the compositions (x) between 0.05 and 0.30. The slight relaxation seen in ε' for x = 0.40 could be due to compositional inhomogeneities. Dielectric properties of BS-PT ceramics with composition x = 0.36 were studied by Porokhonskyy et al. [8] in the frequency interval 100 Hz to 1 THz and it was suggested that this particular sample exhibited relaxation unlike relaxor or dipolar glasses, but due to some dynamic disorder, originating, for example, from domain wall motion.

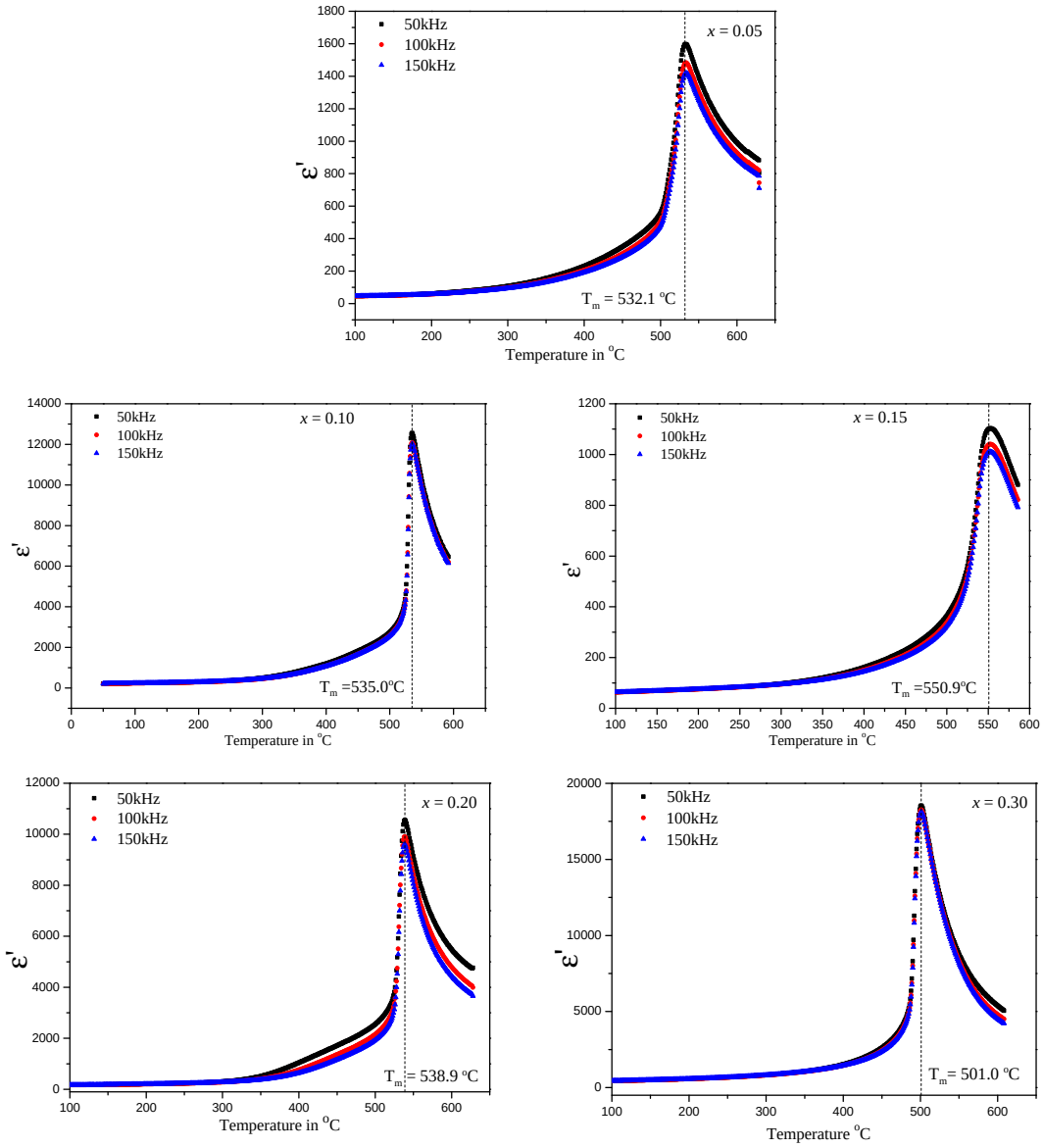

Figure 3-13 Temperature-dependent dielectric constant of BS-PT ceramics for different compositions.

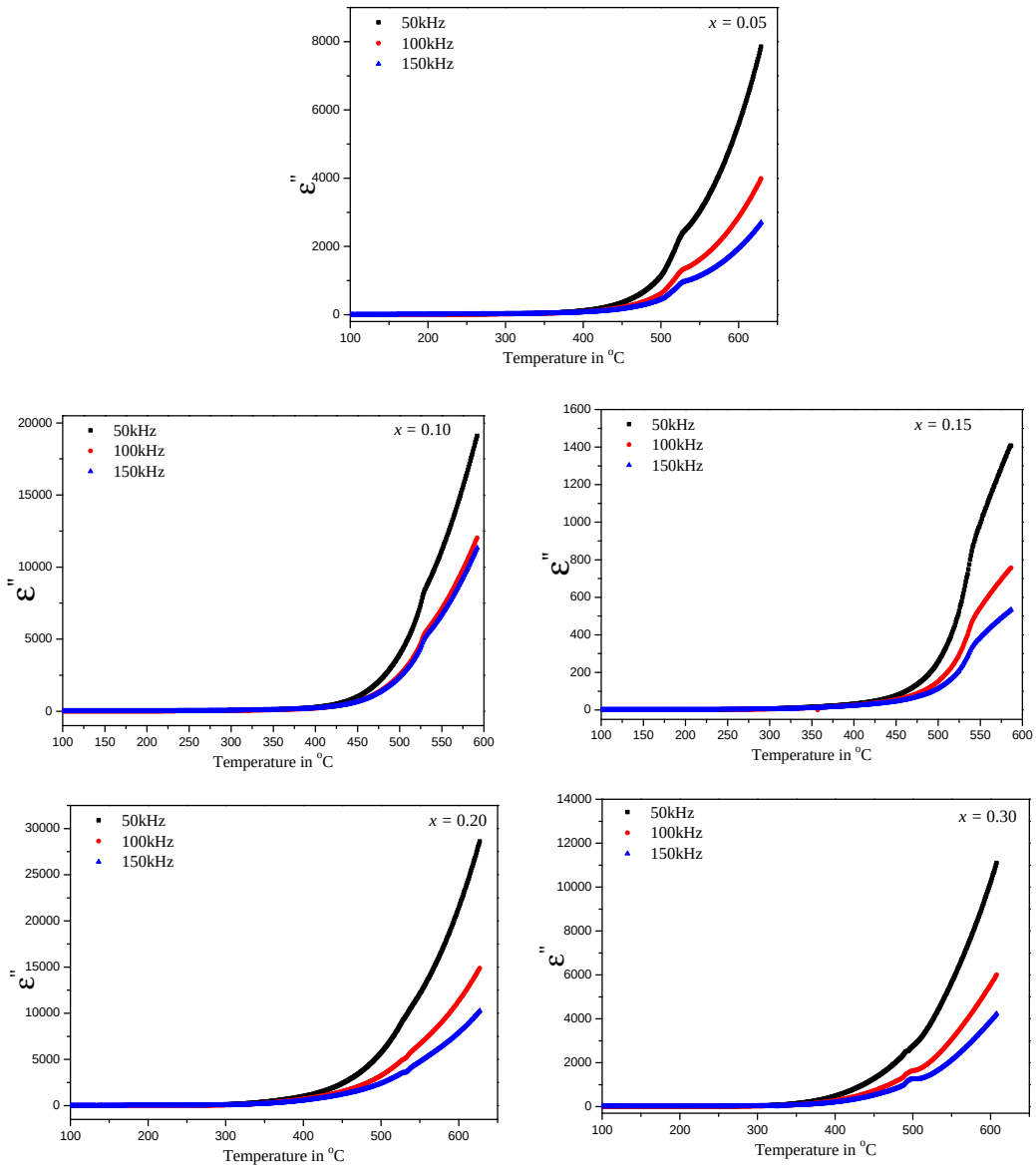

Figure 3-14 Temperature-dependent imaginary part of the dielectric permittivity of BS-PT ceramics for different compositions.

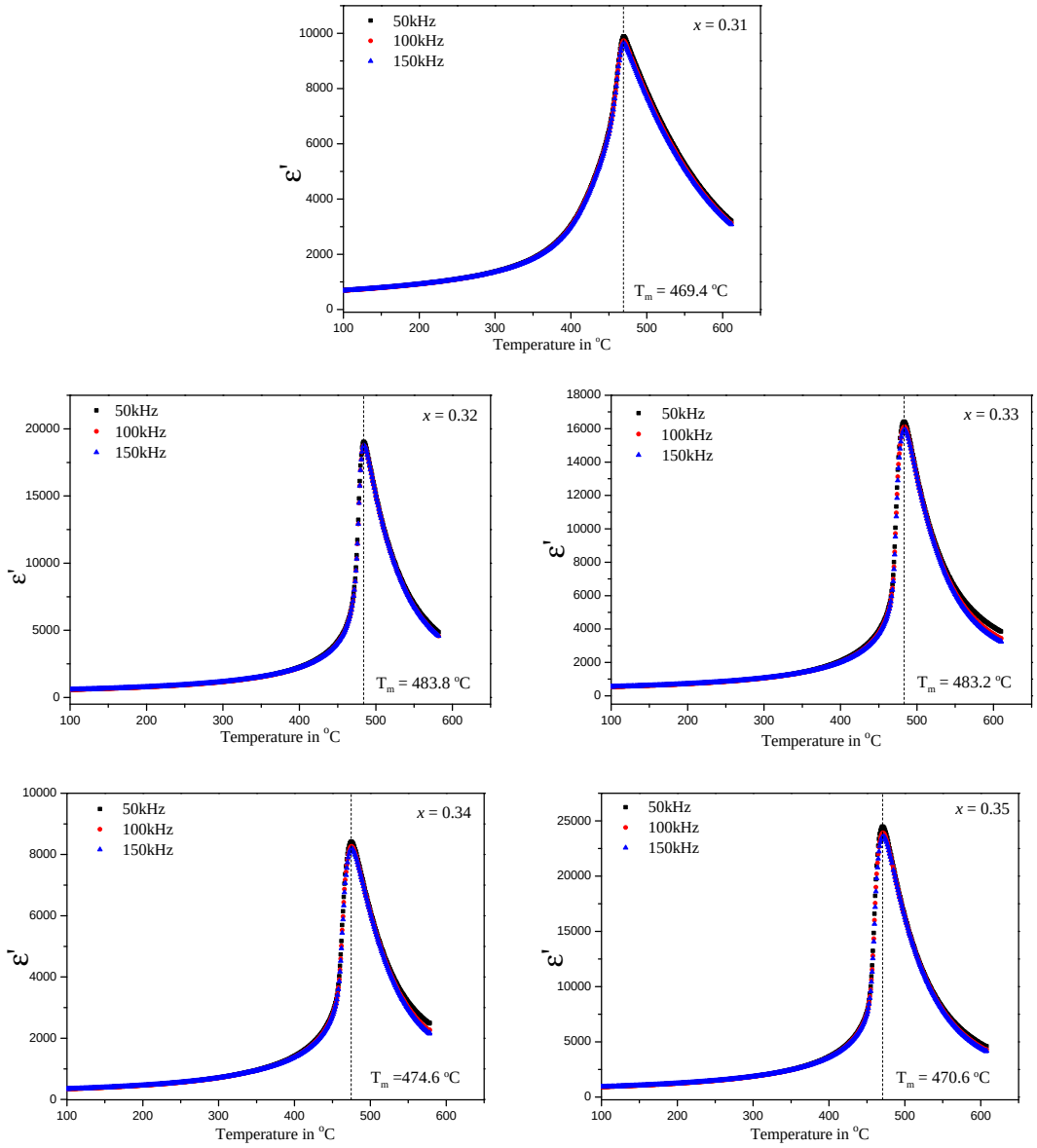

Figure 3-15 Temperature-dependent dielectric constant of BS-PT ceramics for different compositions.

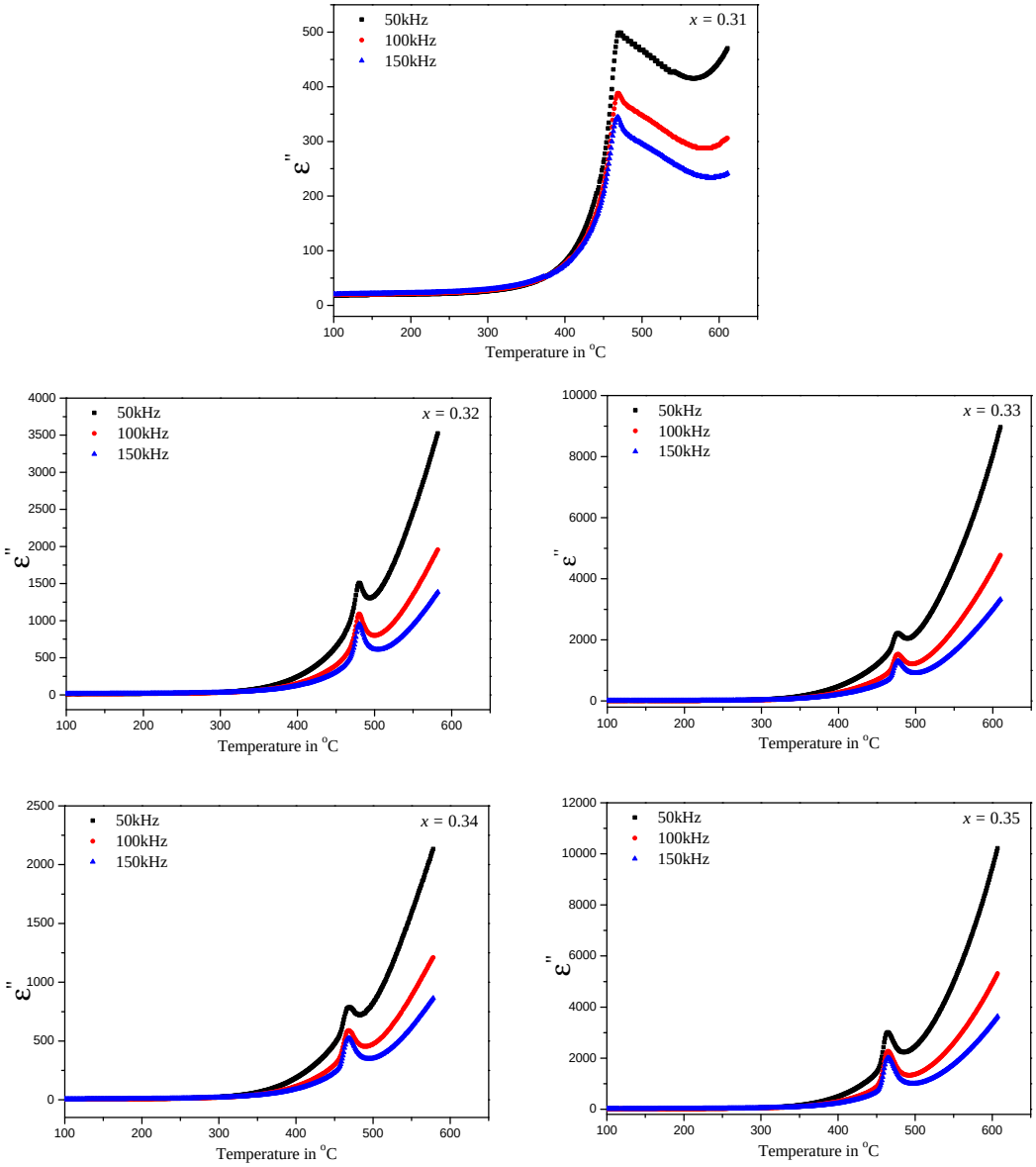

Figure 3-16 Temperature-dependent imaginary part of the dielectric permittivity of BS-PT ceramics for different compositions.

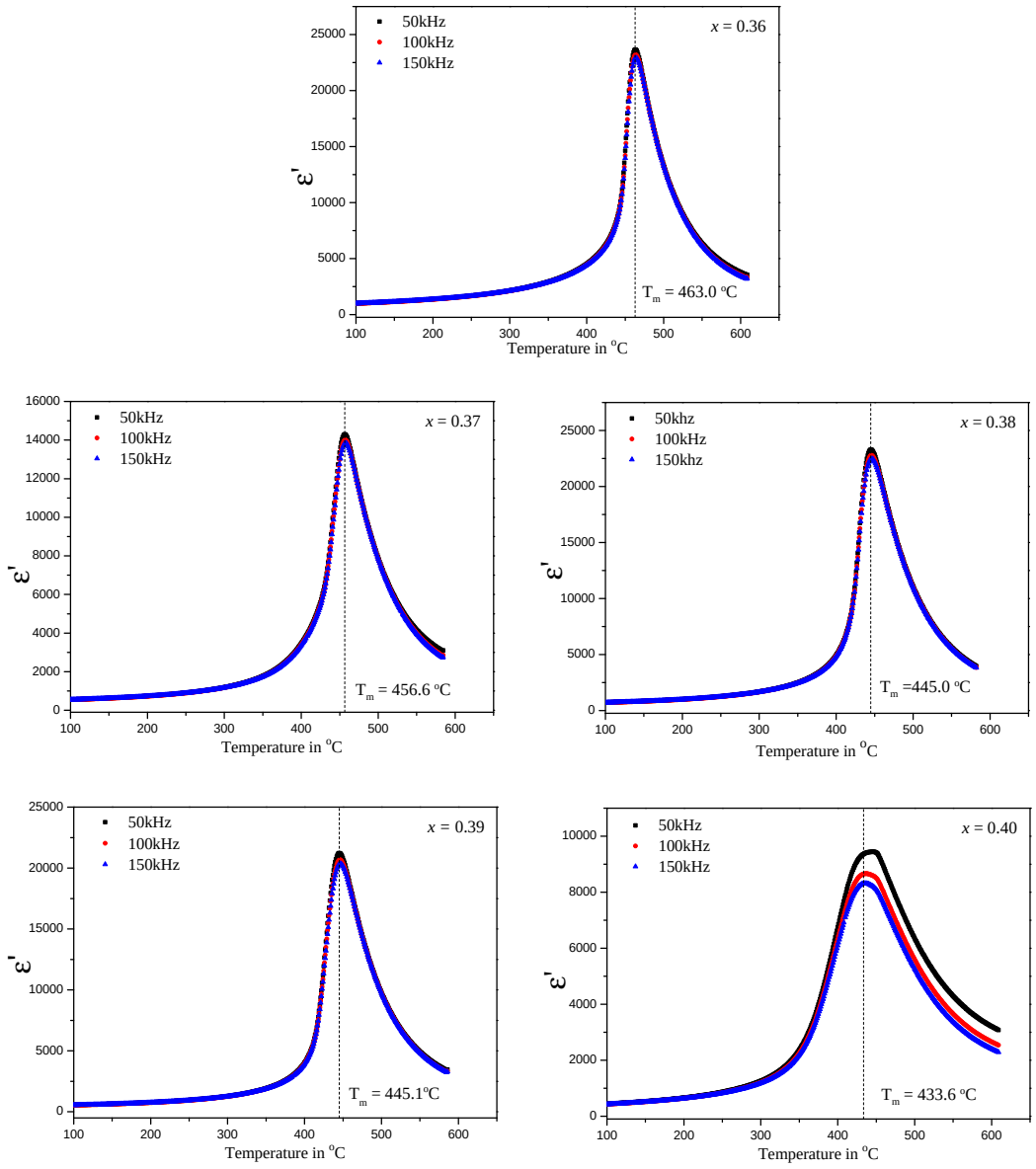

Figure 3-17 Temperature-dependent dielectric constant of BS-PT ceramics for different compositions.

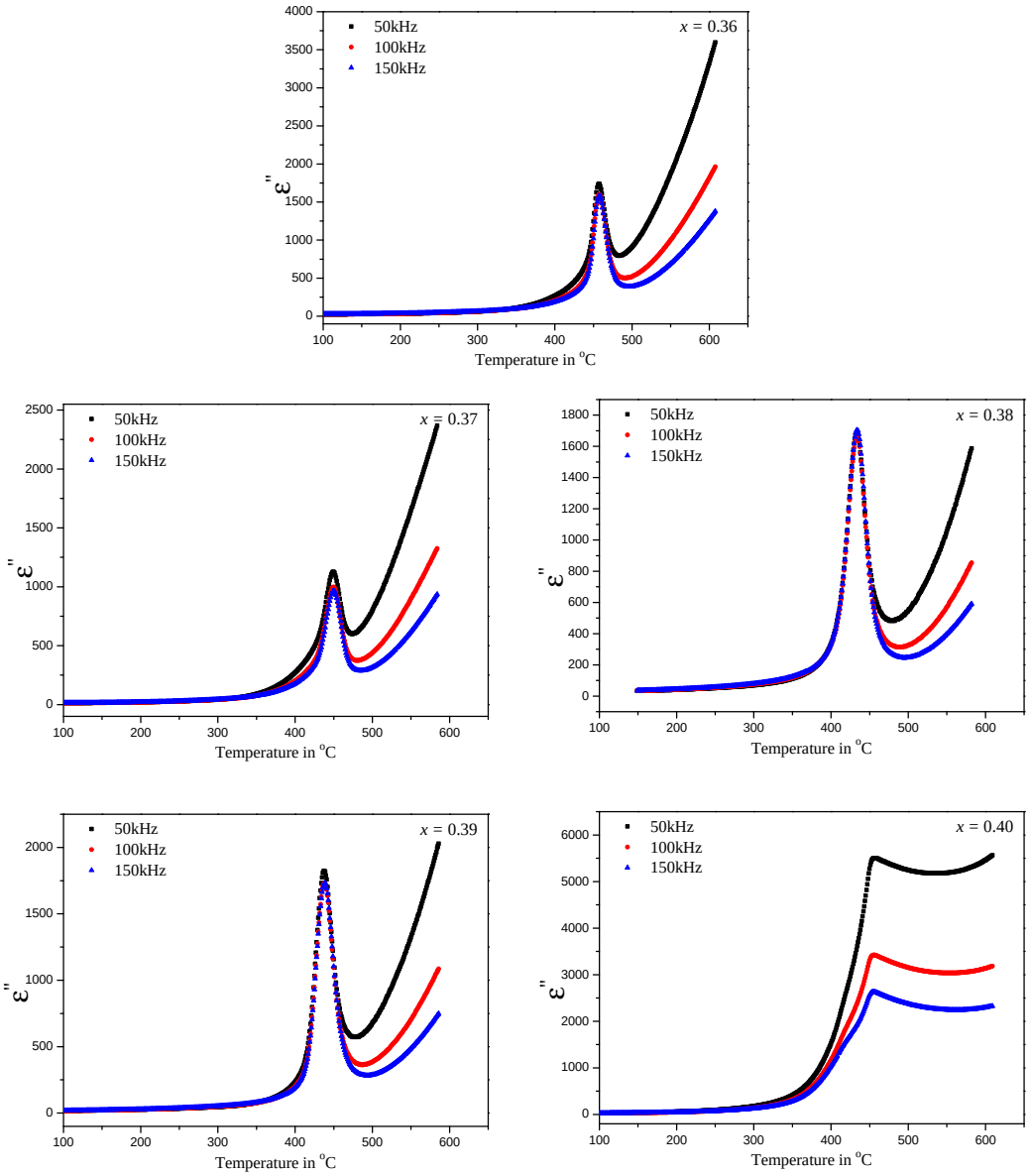

Figure 3-18 Temperature-dependent imaginary part of the dielectric permittivity of BS-PT ceramics for different compositions.

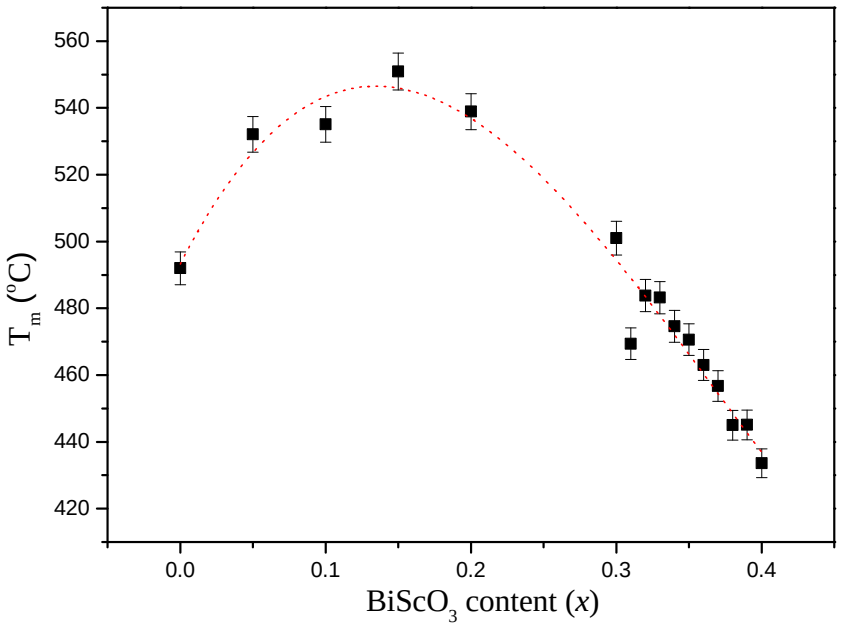

Figure 3-19 The compositional dependence of the ferroelectric to paraelectric transition temperatures (T_m, obtained from the dielectric plots) for BS-PT ceramics demonstrates a non-linear dependence on doping concentration, which is not very common in case of PT-based binary solid solutions.

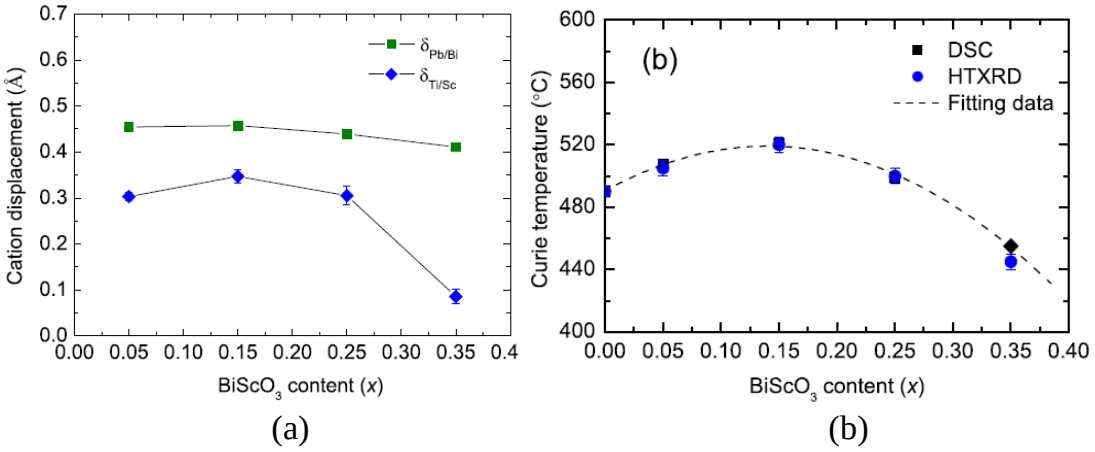

Figure 3-20 (a) Cation displacements and (b) T_c for BS-PT ceramics as a function of composition reported by Chen et al. [41].

3.3.3 Investigation of Single Crystals of BS-PT

3.3.3.1 Single crystal growth

Single crystals were grown following the flux-growth technique [13]. Calcined ceramics were mixed with a flux containing PbO and Bi_2O_3 in a ratio of 70:30 by weight. The mixture, which consisted of a ratio of flux:ceramics of 40:60 by weight, was then heated to 1200 °C with a dwelling time of 4h. A slow cooling rate (1 °C/h from 1200 °C to 800 °C, 5 °C/h from 800 °C to 600 °C and finally 50 °C/h down to room temperature) was employed to provide sufficient time for nucleation.

3.3.3.2 Experimental Technique

The experimental procedure consists of two main stages: (1) Determination of the orientation of the crystal and (2) precise investigation of individual Bragg reflections. The first part of the experiment was performed on a Gemini R CCD diffractometer (Oxford diffraction), which allowed Bragg intensities to be collected very quickly over extended regions of reciprocal space. This provided the essential information to determine the orientation of the crystal with respect to a custom-made crystal-holder and with this knowledge, it was possible to position that crystal in the high resolution x-ray diffractometer (HRXRD) to observe individual Bragg reflections and their fine splittings, if any. The HRXRD is a four circle PANalytical X'Pert Pro MRD equipped with a solid state PIXcel detector. This allowed us to investigate selected regions of the reciprocal space more precisely.

The custom-built crystal holder is schematically shown in fig 3-21 and consists of a rectangular frame with a metal pin inside. The faces of the frame serve as the natural coordinate system for defining the orientation of a crystal. One of the faces is equipped with the rail for fitting into the platform on the HRXRD. A short (about 5 min) data collection at the CCD diffractometer allowed us to locate the positions of about 13 strong reflections and to determine the orientation of three pseudocubic axes $a^\star$, $b^\star$ and $c^\star$ relative to the three orthogonal faces of the frame. The different twin components were not resolved, therefore the directions of $a^\star$, $b^\star$ and $c^\star$ should be understood as the average directions of reciprocal lattice basis for the different twin domains. The crystal holder was then transferred to the high resolution diffractometer while preserving the orien-

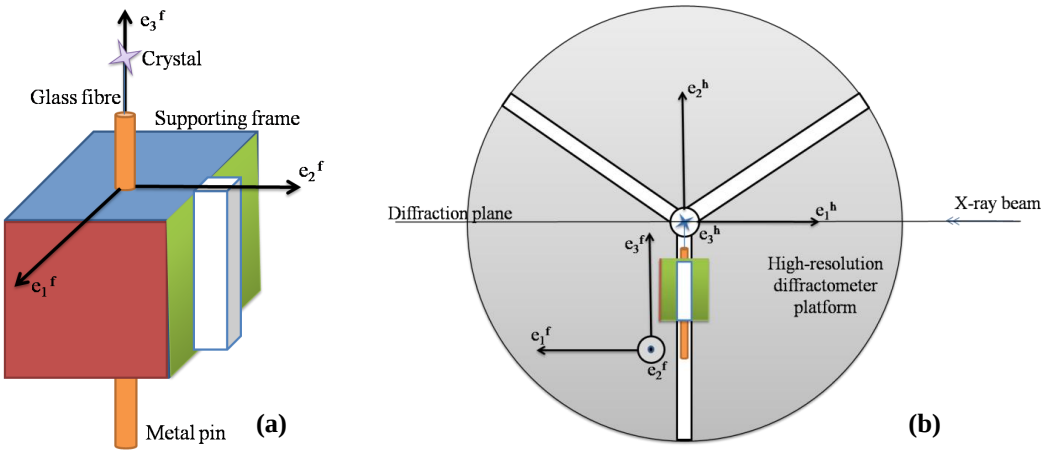

Figure 3-21 (a) The schematic view of the custom-built crystal holder used to preserve the orientation of a crystal. The metal pin is used to attach the frame and a crystal to the HUBER goniometer head. (b) The positioning of the supporting frame on the platform of the high-resolution diffractometer.

Table 3-4 Summary of the measurements performed at the HRXRD

Crystal data	
Composition	$x = 0.64$
Cell setting	Pseudocubic
Crystal size	$0.15 \times 0.15 \times 0.15$ mm^3
Averaged lattice constants as determined from CCD	$a = 4.0186(9), b = 4.0196(9), c = 4.0223(9)$Å; $\alpha = 89.90(2)^\circ, \beta = 89.91(2)^\circ, \gamma = 89.90(2)^\circ$
Experimental details	
Diffractometer	Panalytical X'Pert Pro
Detector	PIXcel
Number of collected reciprocal space maps	20
Total number of reflection positions	83

tation of a crystal relative to the three orthogonal faces of the crystal holder. Keeping the orientation fixed makes it possible to calculate the diffractometer angles to bring the point of the reciprocal space h$a^\star$+k$b^\star$+l$c^\star$ onto the Ewald sphere.

A series of 20 different ω-2θ maps for different Bragg reflections (corresponding to different {hkl}) were recorded on the high-resolution diffractometer. The summary of the measurements is presented in the Table 3-4.

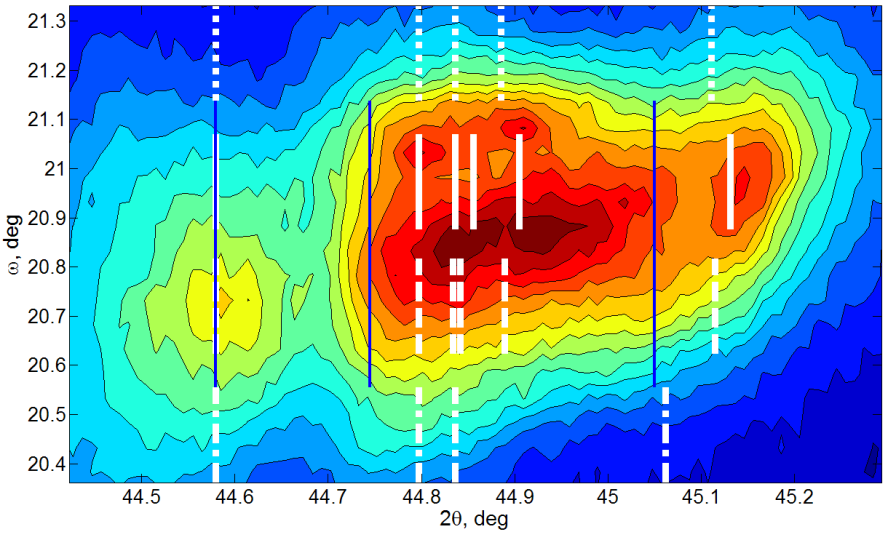

Figure 3-22 The ω vs. 2θ plot shows the contribution of twin domains into the $\{002\}_{pc}$ reflection. The white lines represent the possible splittings in 2θ for different combinations of lattices [(1) M(C)+M(C), (2) O(P)+O(P), (3) M(P)+M(P), (4) M(P)+M(C) from bottom to top, respectively]. The blue lines predict the splittings if a single triclinic lattice is assumed.

3.3.3.3 Results and discussions

For the general treatment of the data a list of indices $\{hkl\}_{pc}$ (pc refers to the pseudocubic reference axes) was generated by assuming a primitive cubic lattice (space group $Pm\bar{3}m$). Then the peaks obtained in each map were assigned to a specific (hkl) by finding the best possible correspondence between the observed and the calculated splitting in 2θ values. This was ensured by minimizing the Global Error-Sum (GES) defined as follows:

$$\sum_{m=1}^{M}\sum_{t=1}^{T_m-1}[\Delta 2\theta_{tOBS}(h_m) - \Delta 2\theta_{tCALC}(h_m)]^2 \qquad (3\text{-}3)$$

where $\mathbf{h}_m = h_m\mathbf{a}^* + k_m\mathbf{b}^* + l_m\mathbf{c}^*$; $\Delta 2\theta_t(\mathbf{h}_m) = 2\theta_{t+1}(\mathbf{h}_m) - 2\theta_t(\mathbf{h}_m)$ and $\Delta 2\theta_{tOBS}$ and $\Delta 2\theta_{tCALC}$ refer to the observed and calculated splittings, respectively.

The outer sum runs over the total number (M) of ω vs. 2θ maps collected whereas the inner sum runs over the total number of splittings observed ($T_m - 1$, where T_m refers to the total number of peaks observed in the m^{th} map) within a particular map.

In general the splitting observed in the ω vs. 2θ maps for particular reflections, such as $\{00l\}_{pc}$, $\{hhh\}_{pc}$, $\{hh0\}_{pc}$ provides crucial information about the symmetry of a

single domain. Figure 3-22 demonstrates the ω vs. 2θ plot of the $\{002\}_{pc}$ Bragg reflection observed for the BS-PT sample. It is evident from the splittings present that the $\{002\}_{pc}$ map contains more than five different contributions, which is inexplicable by a single phase, even if a triclinic lattice is assumed. Having confirmed that a single phase is not sufficient to explain all the splittings observed for different $\{hkl\}_{pc}$, a few different combinations of two phases were then considered. Different lattices (Primitive or C-centered) from the same crystal system were also taken into account. These various combinations were tested for the ability to reproduce the observed splittings of the $\{002\}_{pc}$ reflection. The six different values of 2θ observed in case of $\{002\}_{pc}$ can only be modelled by (a) two primitive orthorhombic (O(P)), (b) two primitive monoclinic (M(P)) lattices or (c) a combination of primitive orthorhombic and primitive monoclinic lattices. With these possible combinations, a least squares fit was carried out taking account of all the twenty ω vs. 2θ maps recorded and minimizing the global error-sum (GES) defined by Equation 3-3. The refinement was carried out varying the parameters responsible for the splittings. For example, when a combination of primitive orthorhombic O(P) ($a_1 \neq b_1 \neq c_1, \alpha_1 = \beta_1 = \gamma_1$) and a primitive monoclinic lattice M(P) ($a_2 \neq b_2 \neq c_2, \alpha_2 = \gamma_2 = 90 \neq \beta_2$) was chosen, the refinable parameters were the following: $b_1 - a_1$, $c_1 - a_1$, $a_2 - a_1$, $b_2 - a_1$, $c_2 - a_1$ and β_2. In a similar fashion the refinable parameters were determined for different combinations of lattices and in the case of C-centered monoclinic lattices M(C), the lattice parameters were used in the pseudocubic setting ($a = b \neq c, \alpha = \beta \neq \gamma$).

The outcome of the fit for different combinations is listed in Table 3-5. It should also be noted that the refinements frequently fell into local minima and the final result was sensitive to the starting values of the parameters. To avoid this problem, a particular routine was followed, which involved : (1) generation of 10000 random starting points for the parameters to be refined and calculation of the error-sum for each of them; (2) the best 100 starting points were chosen on the basis of the values obtained from the error-sum in stage (1) to perform the refinements. However, when occasionally different solutions having similar error-sums were obtained, the solution which provided the least error-sum for the $\{002\}_{pc}$ reflection was selected. From Table 3-5, it is evident that any combination consisting either of a rhombohedral phase (R) or a tetragonal phase (T) or a C-centered monoclinic lattice M(C) is not a good choice. In powder diffraction, these

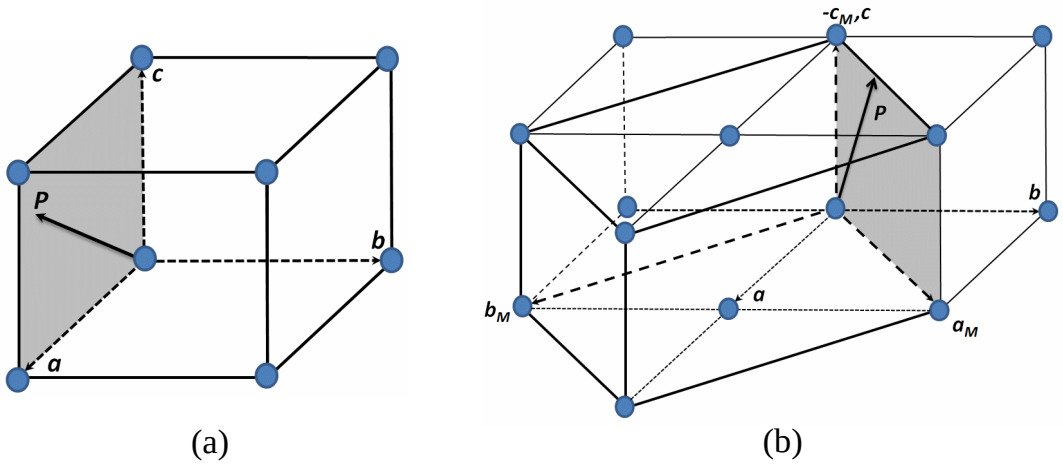

Figure 3-23 (a) A primitive monoclinic M(P) lattice, for this the mirror plane has Miller indices (010). (b) A C-centered M(C) monoclinic cell, for this the mirror plane has Miller indices $(1\bar{1}0)$. On pseudocubic setting the lattice parameters are $a = b \neq c, \alpha = \beta \neq \gamma$.

similar pseudo-symmetric structures are difficult to distinguish and it can be possible to get an average model consisting of R + T, R + M or T + M from the refinement of the powder pattern. In fig 3-24, further reciprocal space maps having different $\{hkl\}_{pc}$ are shown with the predicted 2θ positions obtained from the refinements. Two O(P) lattices and two M(P) lattices were found with comparable values of GES. However, from the $\{222\}_{pc}$ it is clear that two O(P) lattices are not sufficient to reproduce more than two reflections observed in $\{222\}_{pc}$ which suggests that M(P) + M(P) is probably the best representation of the domain structures of BS-PT single crystals at the MPB. The values of the refined parameters for the M(P)+M(P) lattices are listed in Table 3-6.

Table 3-5 Summary of the results of the refinement of observed splitting with different combination of phases.

Different combination of lattices	The set of varied parameters	Global Error Sum	The best error sum for {200} map / corresponding GES
R + T	$\alpha 1$ $a2-a1$ $c2-a1$	0.10 - 0.21	0.018 / 0.14
R + O(P)	$\alpha 1$ $a2-a1$ $b2-a1$ $c2-a1$	0.07 - 0.14	0.003 / 0.09
R + M(P)	$\alpha 1$ $a2-a1$ $b2-a1$ $c2-a1$ $\beta 2$	0.04 - 0.10	0.006 / 0.06
T+M(C)	$c1-a1$ $a2-a1$ $c2-a1$ $\alpha 2, \gamma 2$	0.05 - 0.27	0.003 / 0.07
T+M(P)	$c1-a1$ $a2-a1$ $b2-a1$ $c2-a1$ $\beta 2$	0.04 - 0.08	0.002 / 0.04
O(P)+O(P)	$b1-a1$ $c1-a1$ $a2-a1$ $b2-a1$ $c2-a1$	0.11 - 0.14	0.001 / 0.12
O(P)+M(C)	$b1-a1$ $c1-a1$ $a2-a1$ $c2-a1$ $\alpha 2, \gamma 2$	0.03-0.25	0.002 / 0.06
O(P)+M(P)	$b1-a1$ $c1-a1$ $a2-a1$ $b2-a1$ $c2-a1$ $\beta 2$	0.02 - 0.08	0.0015 / 0.03
M(C)+M(C)	$c1-a1$ $a2-a1$ $b2-a1$ $c2-a1$ $\alpha 1$, $\gamma 1$ $\alpha 2, \gamma 2$	0.04-0.20	0.01 / 0.06
M(P)+M(P)	$b1-a1$ $c1-a1$ $a2-a1$ $b2-a1$ $c2-a1$ $\beta 1, \beta 2$	0.02 - 0.05	0.0008 / 0.0305

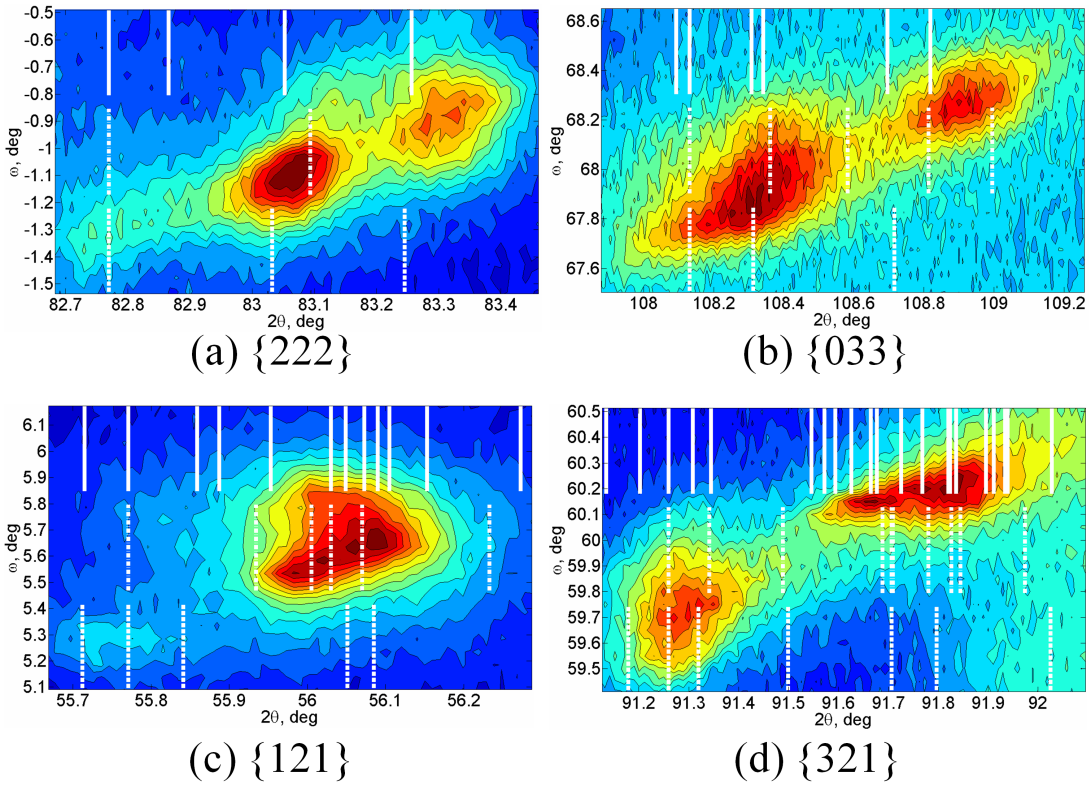

Figure 3-24 Additional four ω vs 2θ maps for different $\{hkl\}_{pc}$s. The lines represent the predicted 2θ positions after refinement assuming different combinations of lattices [from bottom to the top (1) R+T, (2) O(P)+O(P), (3) M(P)+M(P)].

Table 3-6 Values of the refined parameters for M(P)+M(P) model.

Model	Varied parameters	Refined values
M(P)+M(P)	$b1-a1$	-0.016 Å
	$c1-a1$	-0.04 Å
	$a2-a1$	-0.04 Å
	$b2-a1$	-0.03 Å
	$c2-a1$	-0.02 Å
	$\beta 1$	89.92°
	$\beta 2$	90.11°

3.4 Discussions

The behaviour of the structural phase transition in BS-PT ceramics as a function of composition is complex, especially at the MPB. The precise and unambiguous determination of the phase boundary location along with the correct symmetry of the phases based on one-dimensional powder diffraction data is challenging. However from the Rietveld refinements against neutron powder diffraction data, the phases of the BS-PT system as a function of composition have been determined. Three different regions were identified where the high temperature cubic phase stabilizes into (1) a tetragonal phase for $x \leq 0.35$; (2) a tetragonal+monclinic phase for $0.36 \leq x \leq 0.38$ and finally (3) to a apparent monoclinic phase for $x \geq 0.39$. The suggestion of monoclinic symmetry for composition $x \geq 0.39$ has been further supported by high-temperature x-ray diffraction results. In addition, a correlation has been shown between the enhancement of the Curie temperature and the shift of the Ti/Sc atom from its ideal position.

The single crystal diffraction experiments have provided interesting results for the crystal with MPB composition ($x = 0.36$). This stands out from the powder diffraction results providing strong evidence against as yet assumed R+T model for the MPB and even for the T+M model which we found the best description from the powder data. This once again points out the complexity of the problem and renders many questions on the phase formations at MPB. Further research is on-going in developing more single crystals across the phase diagram to determine and establish a more accurate phase diagram than we currently have from the powder diffraction data. It is also important to determine the exact stoichiometric ratio between Pb/Ti and Bi/Sc as the average structure is very sensitive to the compositional fluctuations for this system.

References

[1] F. Jona and G. Shirane, *Ferroelectric Crystals* (Oxford Pergamon Press, 1962).

[2] J. Kuwata, K. Uchino, and S. Nomura, Ferroelectrics **37**, 579 (1981).

[3] T. R. Shrout, Z. P. Chang, N. Kim, and S. Markgraf, Ferroelectr. Lett. Sect. **12**, 63 (1990).

[4] Y. Yamashita, Jpn. J. Appl. Phys. **33**, 5328 (1994).

[5] R. E. Eitel, C. A. Randall, T. R. Shrout, P. W. Rehrig, W. Hackenberger, and S. E. Park, Jpn. J. Appl. Phys. **40**, 5999 (2001).

[6] R. E. Eitel, C. A. Randall, T. R. Shrout, and S. E. Park, Jpn. J. Appl. Phys. **41**, 2099 (2002).

[7] Y. Shimojo, R. Wang, T. Sekiya, T. Nakamura, and L. E. Cross, Ferroelectrics **284**, 121 (2003).

[8] V. Porokhonskyy, S. Kamba, A. Pashkin, M. Savinov, J. Petzelt, R. E. Eitel, and C. A. Randall, Appl. Phys. Lett. **83**, 1605 (2003).

[9] R. E. Eitel, S. J. Zhang, T. R. Shrout, C. A. Randall, and I. Levin, J. Appl. Phys. **96**, 2828 (2004).

[10] Y. Inaguma, A. Miyaguchi, M. Yoshida, and T. Katsumata, J. Appl. Phys. **95**, 231 (2004).

[11] C. A. Randall, R. E. Eitel, and T. R. Shrout, J. Appl. Phys. **93**, 9271 (2003).

[12] J. Chaigneau, J. M. Kiat, C. Malibert, and C. Bogicevic, Phys. Rev. B **76**, 094111 (2007).

[13] S. Zhang, L. Leburn, S. Rhee, R. E. Eitel, C. A. Randall, and T. R. Shrout, J. Cryst. Growth. **236**, 210 (2002).

[14] S. Zhang, C. A. Randall, and T. R. Shrout, Jpn. J. Appl. Phys. **42**, L1152 (2003).

[15] S. Zhang, C. A. Randall, and T. R. Shrout, Appl. Phys. Lett. **83**, 3150 (2003).

[16] S. Zhang, C. A. Randall, and T. R. Shrout, Solid State Comm. **131**, 41 (2004).

[17] S. Zhang, C. A. Randall, and T. R. Shrout, Jpn. J. Appl. Phys. **43**, 6199 (2004).

[18] J. C. Nino and S. Trolier-McKinstry, J. Mater. Res. **19**, 568 (2004).

[19] H. Wen, X. Wang, and L. Li, J. Appl. Phys. **100**, 084315 (2006).

[20] H. Wen, X. Wang, X. Deng, T. Sun, and L. Li, J. Appl. Phys. **101**, 016103 (2007).

[21] H. Wen, X. Wang, C. Zhong, L. Shu, and L. Li, Appl. Phys. Lett. **90**, 202902 (2007).

[22] J. Xaio, A. Wu, and P. Vilainho, Appl. Phys. Lett. **92**, 032902 (2008).

[23] A. Belik, J. Am. Ceram. Soc. **128**, 706 (2006).

[24] R. E. Eitel, T. R. Shrout, and C. A. Randall, Jpn. J. Appl. Phys. **43**, 8146 (2004).

[25] J. Ryo, S. Priya, C. Sakaki, and K. Uchino, Jpn. J. Appl. Phys. **41**, 6040 (2002).

[26] J. Cheng, R. Eitel, N. Li, and L. E. Cross, J. Appl. Phys. **94**, 605 (2003).

[27] T. Song, R. E. Eitel, T. R. Shrout, C. A. Randall, and W. Hackenberger, Jpn. J. Appl. Phys. **42**, 5181 (2003).

[28] P. Winotai, N. Udomkan, and S. Meejoo, Sensor Actuator Phys. **122**, 257 (2005).

[29] T. Song, R. E. Eitel, T. R. Shrout, and C. A. Randall, Jpn. J. Appl. Phys. **43**, 5392 (2004).

[30] S. Zhang, R. E. E. C. A. Randall, T. R. Shrout, and E. F. Alberta, Appl. Phys. Lett. **86**, 262904 (2005).

[31] C. J. Stringer and C. A. Randall, J. Am. Ceram. Soc. **90**, 1802 (2007).

[32] A. M. Glazer and S. A. Mabud, Acta Cryst. B **34**, 1065 (1978).

[33] D. L. Corker, A. M. Glazer, R. W. Whatmore, A. Stallard, and F. Fauth, J.Phys.: Condens. Matter. **10**, 100 (1998).

[34] B. Noheda, J. Gonzalo, L. Cross, R. Guo, S. E. Park, D. Cox, and G. Shirane, Phys. Rev. B **61**, 8687 (2000).

[35] D. Pandey, A. K. Singh, and S. Baik, Acta Crystallogr., Sect. A: Found. Crystallogr **64**, 192 (2008).

[36] B. Kim, P. Tong, D. Kwon, J. M. S. Park, and B. G. Kim, J. Appl. Phys. **105**, 114101 (2009).

[37] S. Nomura, K. Kaneta, J. Kuwata, and K. Uchino, Mater. Res. Bull. **17**, 1471 (1982).

[38] R. Duan, R. F. Speyer, E. Alberta, and T. R. Shrout, J. Mater. Res. **19**, 2185 (2004).

[39] C. J. Stringer, T. R. Shrout, C. A. Randall, and I. M. Reaney, J. Appl. Phys. **99**, 024106 (2006).

[40] V. A. Isupov, phys. stat. sol. (a) **181**, 211 (2000).

[41] J. Chen, K. Nittala, J. L. Jones, P. Hu, and X. Xing, Appl. Phys. Lett. **96**, 252908 (2010).

Chapter 4

Structural investigation of xBiScO$_3$-(1-x)BaTiO$_3$

4.1 Introduction

Bismuth scandium oxide $BiScO_3$ (BS) was first synthesized by Tomashpolski et al. [1] under high pressure and reported to be ferroelectric with triclinic symmetry. The main reason that this material has not been investigated up until 2001 [2], is because of its poor phase stability (perovskite tolerance factor ~ 0.907) under ambient conditions as it can only be prepared at high pressures. Since the discovery of BS-PT system in 2001, BS has exhibited potential to be an attractive candidate for lead-free applications. Incorporation of BS in PT significantly enhanced the physical properties of $PbTiO_3$ and modified the structure as a function of composition. In addition to PT, BS was used to develop novel materials by alloying with other known stable lead-free compounds and solid solutions such as $Na_{1/2}Bi_{1/2}TiO_3$ (fig 4-1) and $K_{1/2}Na_{1/2}NbO_3$ [3–5] in order to ameliorate the physical properties of the end members. The KNNBS system shows an increase in d_{33} piezoelectric charge coefficient from $\sim$ 100 pC/N to a value of $\sim$ 200 pC/N for an orthorhombic rhombohedral 'MPB' composition at 98%KNN 2%BS. Very recently there are many reports on BS-based ternary systems, such as BS mofified $0.93K_{1/2}Na_{1/2}NbO_3$-$0.07LiTaO_3$ (fig 4-2) , $(K_{0.475}Na_{0.475}Li_{0.05})(Nb_{0.95}Sb_{0.05})O_3$ (fig 4-3) and (1-y)$(Na_{0.5-0.5x}K_{0.5-0.5x}Li_x)NbO_3$-$y$BiScO$_3$ (y = 0.01 and x = 0 0.06) (fig 4-4).

In the previous chapter we have discussed the structure and dielectric properties of the BS-PT system, which was one of the systems predicted by Eitel et al. [2], based on the tolerance factor approach. Following that concept and to develop lead-free materials with improved qualities, a lead-free analogue of BS-PT can be prepared by replacing the Pb with Ba. Since $BaTiO_3$ and $PbTiO_3$ have a similar structure at room

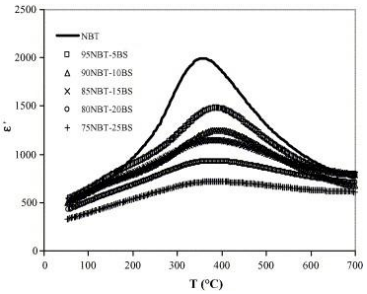

(a)

x	0.05	0.10	0.15	0.20	0.25
T_m (°C)	383	397	385	386	385
ε'_{max}	1510	1270	1150	940	720

(b)

Figure 4-1 Properties of (1-x)NBT-xBS ceramics as a function of x. Although the T_m remains nearly constant with increasing x, the broadening of the dielectric peak increases with x. No structural details were reported for the ceramics as a function of x [6].

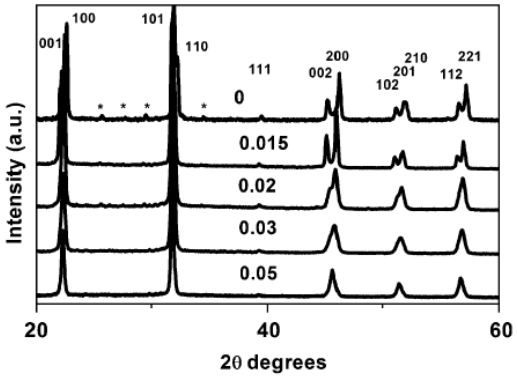

(a)

Composition	0	0.015	0.02	0.05
Property				
d_{33} (pC/N)	200	156	108	32
$\varepsilon_{r\text{-max}}$	3599	4197	1804	1278
T_c (°C)	447	397	359†	202†

†Temperature of ε_{r-max} of broad peak.

(b)

Figure 4-2 Structure and property for the solid solution (1-x)[0.93KNN0.07LiTaO]-xBiScO$_3$ as a function of x. (a). The tetragonality (c/a) decreases with increasing BiScO$_3$ content. For $x \geq 0.02$ the structure is pseudocubic. (b). The table shows the decrease in d_{33}, ε' and T_c with the increase of BS content [7].

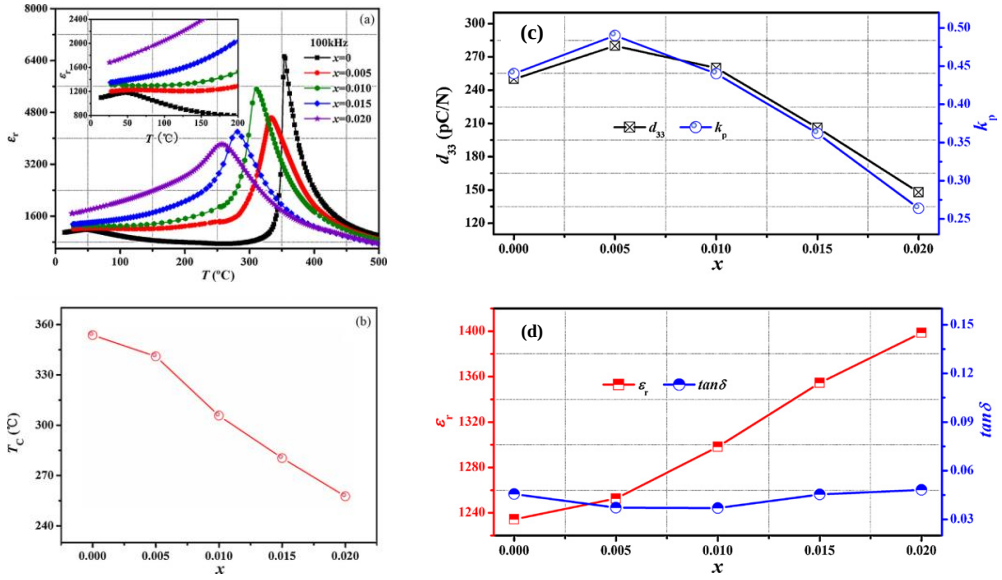

Figure 4-3 Properties of a newly developed solid solution (1-x)$K_{0.475}Na_{0.475}Li_{0.05}$)($Nb_{0.95}Sb_{0.05}$)$O_3$-$x$BiScO$_3$ for different values of x. The structure was reported as tetragonal for $x \leq 0.20$. Decrease in Tc with increase in BS was seen (a, b) and the ceramics with x = 0.005 poled at 30 °C exhibited optimum piezoelectric properties with d_{33} = 280 pC/N, k_p = 49%, ε' = 1432 and tanδ = 0.037 [8].

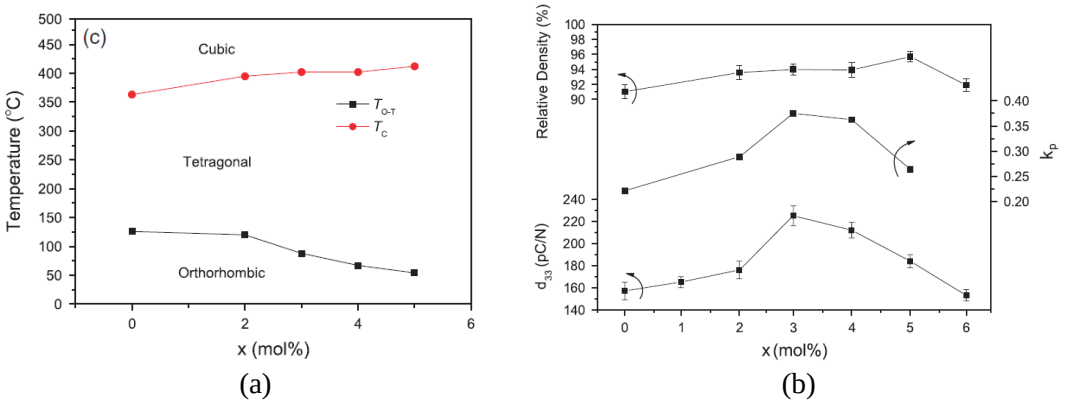

Figure 4-4 Properties of solid solution 0.99($Na_{0.5-0.5x}K_{0.5-0.5x}Li_x$)$NbO_3$-0.01BiScO$_3$ as a function of x. (a) Compositional dependences of T$_c$ and T$_{OT}$. (b) Compositional dependences of the d_{33}, k_p and density of ceramics [9].

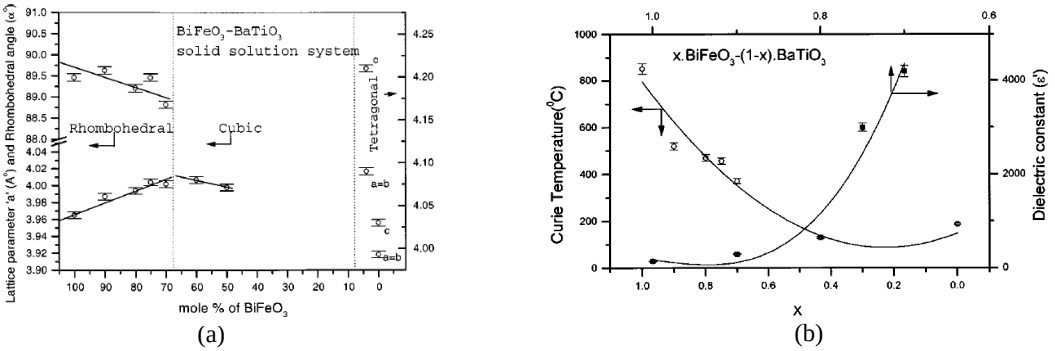

Figure 4-5 Structure and properties of xBiFeO$_3$-(1-x)BaTiO$_3$ ceramics as a function of x [12].

temperature, it is interesting to compare the effect of BiScO$_3$ on the structure and physical properties of BT. When Pb was replaced by Ba in high-temperature piezoeletric xBiFeO$_3$-(1-x)PbTiO$_3$ [10, 11], to form the solid solution of xBiFeO$_3$-(1-x)BaTiO$_3$, a tetragonal-pseudocubic phase boundary was seen at $x \sim 0.10$ with an initial decrease in T_c for $x \leq 0.20$ [12]. Fig 4-5 shows the structural changes and the variations of T_c and ε' of the BF-BT ceramics as a function of composition.

Solid solutions of xBiScO$_3$-(1-x)BaTiO$_3$ were first studied as thin films [13]. Epitaxial films of xBS-(1-x)BT system were grown using the pulsed laser deposition technique. Formation of stable perovskite phases was confirmed between compositions x = 0.2 and 0.6 and an apparent phase boundary was identified around x = 0.4 (fig 4-6a). Recently Ogihara et al. [14] has published the results of the investigation carried out on bulk ceramics of BS-BT system as a function of composition. A structural change from tetragonal to pseudocubic symmetry was observed at about x = 0.05-0.075 (fig 4-6b). From dielectric measurements it was concluded that the material evolves as a highly diffusive and dispersive relaxor with increasing BS concentration (x = 0.10 to 0.40). In particular, BS-BT ceramics with x = 0.30 were reported to be high energy density capacitor and demonstrated superior properties than some commercial X7R capacitors [15]. More recently, a couple of investigations were also carried out on BS-BT ceramics doped with K(Bi$_{1/2}$Ti$_{1/2}$)O$_3$ (fig 4-7), Ba(Zn$_{1/2}$Ti$_{1/2}$)O$_3$ (fig 4-8) and even PbTiO$_3$ (fig 4-9) in order to improve the physical properties of this system. However, as yet, no detailed structural information is available on this novel system as a function of composition.

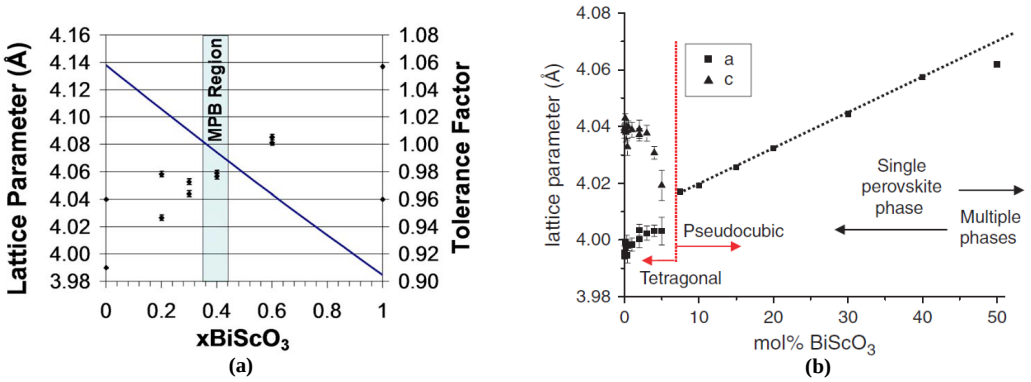

Figure 4-6 The phase diagrams of BS-BT systems reported earlier from the investigations of (a) thin films [13] and (b) bulk ceramics [14].

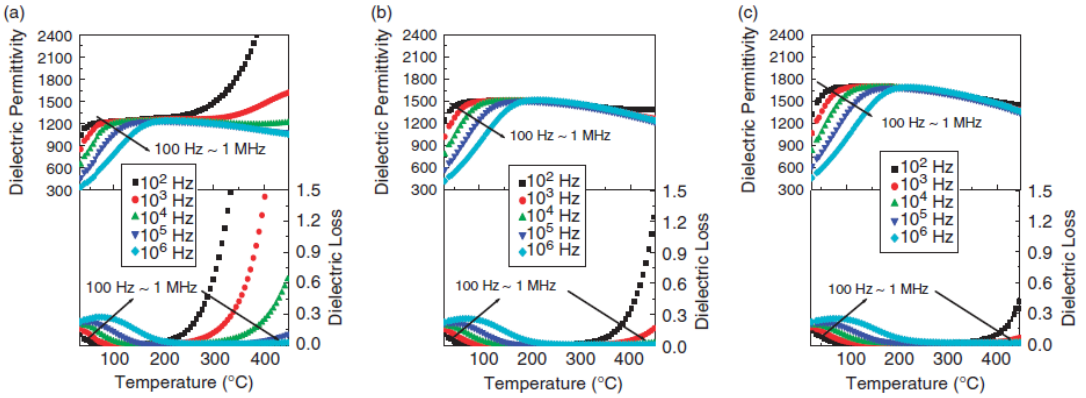

Materials	Hot-isostatic pressing (HIP) Thickness (μm)	ε_r	Loss (%) at 1 MHz	TCε (ppm/°C) at 1 MHz	Energy density (J/cm^3) at 200 kV/cm	RC constants (s) at 300°C	Resistivity (×109 Ω·cm) at 300°C	Normal sintering ε_r	Loss (%) at 1 MHz
BSBT	170	1300	2.2	−600	2.7	0.01	0.1	1230	0.5
BSBT-KBT10	170	1500	1.5	−700	2.9	0.1	1	1350	1.2
BSBT-KBT20	170	1750	1.5	−800	2.7 (4.0†)	0.8	5	1670	1.7

†Thickness of 90 μm at 220 kV/cm.

Figure 4-7 Effect of KBT on the properties of BS-BT ceramics. (Top) Temperature dependence of dielectric constant and loss for 0.40BS-0.60BT ceramics with (a) 0 %, (b) 10% and (c) 20% of KBT. (Bottom) The table presents the values of various physical parameters as a function of KBT content [16].

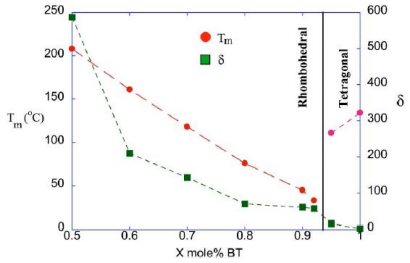

(a)

x mol % BT	0.5	0.6	0.7	0.8	0.9	0.92	0.95	1
Structure	Rhombohedral						Tetragonal	
lattice parameter (Å)	4.046	4.040	4.030	4.022	4.014	4.009	a: 3.997 c: 4.023	a: 3.992 c: 4.034
T_m(°C)	208	161	118	76	45	33	111	134
ε_m at T_m	1100	1170	1240	1360	2570	3960	3520	9740

(b)

Figure 4-8 Properties of (1-x)[0.5BiScO$_3$ - 0.5Bi(Zn$_{1/2}$Ti$_{1/2}$)O$_3$] - xBaTiO$_3$ ceramics as a function of x. (a) An apparent rhombohedral-tetragonal phase boundary exists at $x \sim 0.93$. (b) the table shows the values of various structural and physical parameters as a function of x [17]

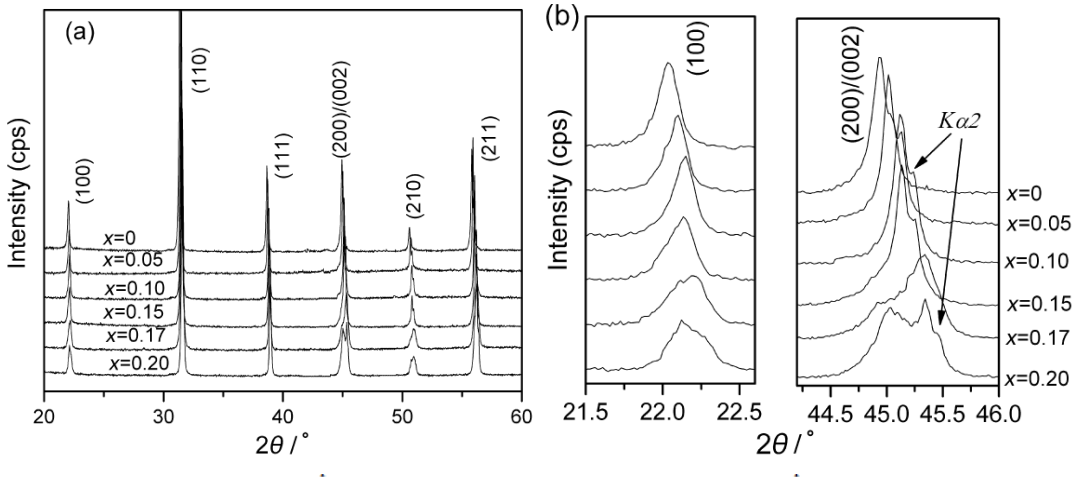

x value	0.20	0.17	0.15	0.10	0.05	0
Lattice parameters* ($\times 10^{-10}$ m)	tetragonal a = 3.9963(5) c = 4.0327(7)	tetragonal a = 3.9987(7) c = 4.0345(1)	4.0155(1)	4.0159(4)	rhombohedral 4.0256(1)	4.0314(1)
T_m (°C)	155	105	60	60	65	85
ε_m at T_m	3826.2	3570.1	3580.4	2305.1	1516.3	1050.4

Figure 4-9 Structure and properties of 0.80BT-(0.2-x)BS-xPT for $x \leq 0.20$ [18].

As mentioned before, to understand the structure-property relationships in these novel functional materials it is crucial to understand the structural changes due to doping of various ions in order to tune the system according to the need. Therefore, in this chapter we discuss in detail the effect of incorporation of $BiScO_3$ on the structure of $BaTiO_3$, which is a popular ferroelectric material with a perovskite structure. BT has been chosen is because its high dielectric constant, large spontaneous polarization, good piezoelectric and non-linear optical properties have made it a promising lead-free alternative for various applications starting from multilayer capacitors, ferroelectric memories, piezoeletric resonators to optical modulators [19]. BT has a tetragonal structure at room temperature, however it has three temperature-dependent phase transitions as shown in fig 4-10. As a result of these phase transitions, BT suffers from the fundamental drawback of poor thermal stability of its properties. This is why it is important to investigate BT-based materials, so that modified and improved BT can be used for a wider range of temperatures.

The structural phase transition in the BS-BT system as a function of composition was initially studied using high-resolution x-ray powder diffraction. However, to understand the influence of the doping at the atomic level, neutron powder diffraction data were collected and Rietveld refinements have been performed. In addition, non-ambient x-ray diffraction was carried out on BS-BT ceramics to investigate the temperature-dependent phase transitions for different composition of the samples. Dielectric properties of the ceramics are also discussed to demonstrate the quality and homogeneity of the material synthesized as well as the change in the ferroelectric transition temperatures of the ceramics as a function of composition.

4.2 Experimental

4.2.1 Synthesis and preliminary characterization

Ceramics of BS-BT with different compositions were prepared by the conventional solid state synthesis route. The starting materials were $BaCO_3$ (Alfa Aesar), TiO_2 (Alfa Aesar), Bi_2O_3 (Alfa Aesar) and Sc_2O_3 (Metall Rare Earth Limited, China) having purity $\sim 99.99\%$. The amount of starting materials for different stoichiometric ratio of the

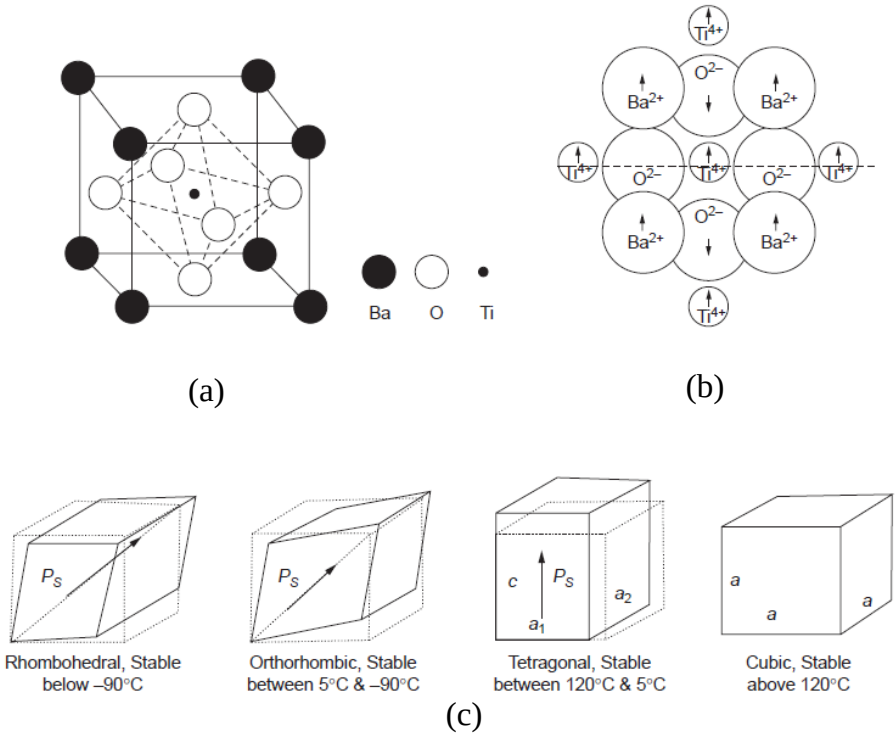

Figure 4-10 Schematic diagrams showing (a) the unit cell of $BaTiO_3$, (b) the ion displacement due to the tetragonal distortion in $BaTiO_3$, and (c) the temperature dependence of the structure of the unit cell. This illustration has been adopted from the book by Kao [20].

samples were calculated from the following equations :

$$Bi_2O_3 + Sc_2O_3 = 2BiScO_3 \quad (4\text{-}1)$$

$$BaCO_3 + TiO_2 = BaTiO_3 + CO_2 \quad (4\text{-}2)$$

In the BS-BT system Bi^{+3} and Sc^{+3} are expected to substitute Ba^{+2} and Ti^{+4}, respectively. The precursors for BS-BT ceramics were calcined at 1000 °C for about 6-10 hrs. A second stage of calcination was performed at 1200 °C for about 8-10hrs and finally the ceramics were sintered at 1400 °C for 10 hrs. After each stage of firing x-ray diffraction patterns were collected to establish the best conditions for synthesizing these ceramics. Fig 4-11 demonstrates the effect of firing at different temperatures. Two distinct effects were noticed when the ceramics were fired at 1400 °C : (1) disappearance of the peaks from unknown phases and (2) a gain in the intensities of the peaks with the narrowing of the peak widths. This suggests that high-temperature sintering is necessary to form a single phase of highly crystalline material. Figure 4-12 shows the the morphology of the ground sintered ceramics for $x = 0.05$. An average grain size of the order of 3 μm

was observed.

4.2.2 X-ray powder diffraction

High resolution x-ray powder diffraction on BS-PT ceramics was performed utilizing a PANalytical X'Pert Pro MPD. Data were collected using a PIXcel detector with step size of 0.013 in the two-theta range of 20-90° in Bragg-Brentano geometry. High-temperature diffraction patterns were collected using an Anton Paar furnace (HTK1200N). Low-temperature diffraction experiments were carried out using a Bruker D5005 diffractometer equipped with a Phenix cryostat (Oxford Cryosystems). Data were collected in the temperature range from 17 °C to −253 °C.

4.2.3 Neutron powder diffraction

Neutron powder diffraction scans (time of flight data) were collected at the ISIS facility using the high resolution powder diffractometer (HRPD). Approximately 12-15 g of powder were loaded into a cylindrical vanadium can and data collected for a total count of 30-35 μA of current. High-resolution data collected at the back-scattering bank (168° bank) were utilized for the Rietveld refinement.

4.3 Results and discussions

4.3.1 Structural investigation

4.3.1.1 Ambient x-ray powder diffraction

Figure 4-13 shows the room-temperature x-ray diffraction patterns of BS-BT ceramics as a function of doping concentration. It is quite evident that a small amount (x = 0.03) of BS diminishes the tetragonality of BT and a second phase is starting to appear when x = 0.05. Figure 4-13 also demonstrates how the {200} doublet of the tetragonal phase transforms to a different phase through a region of co-existing phases with increasing x. As mentioned before, after sintering the samples at around 1400 °C for about 8-10 hrs, there was almost no evidence of any additional peak that was not attributable to the main perovskite phase. There was also no evidence of any super-lattice peaks, indicating that long-scale ordering of cations or oxygen octahedral tilting did not occur.

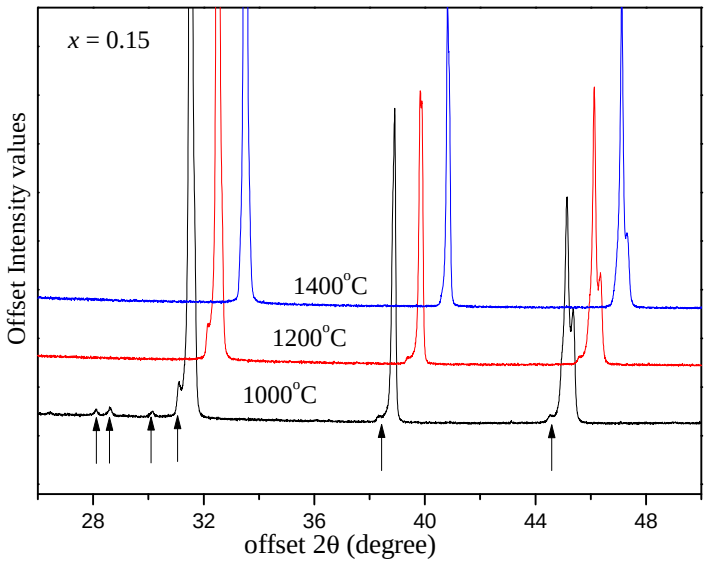

Figure 4-11 Development of the x-ray profile after each stage of firing for the composition $x = 0.15$. Arrows indicate the presence of unwanted phases. Repeated grinding and heating at high temperature were required to form single-phase solid solutions.

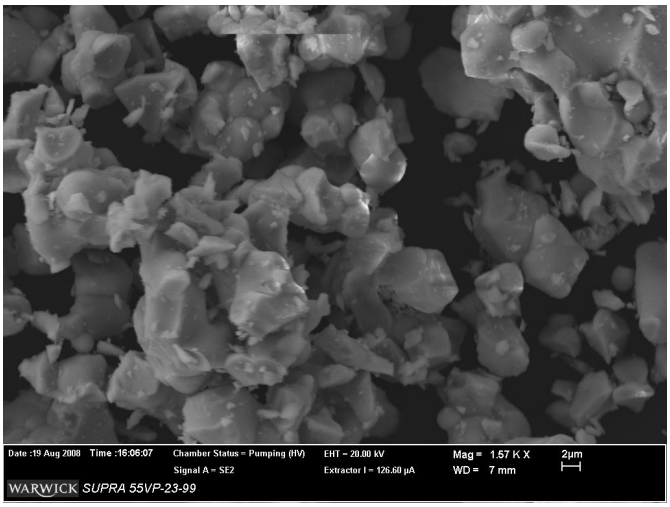

Figure 4-12 Morphology of the BS-BT ceramics for $x = 0.05$. An average grain size of $\sim 3\mu$m can be seen here, although the grains are in agglomerated form.

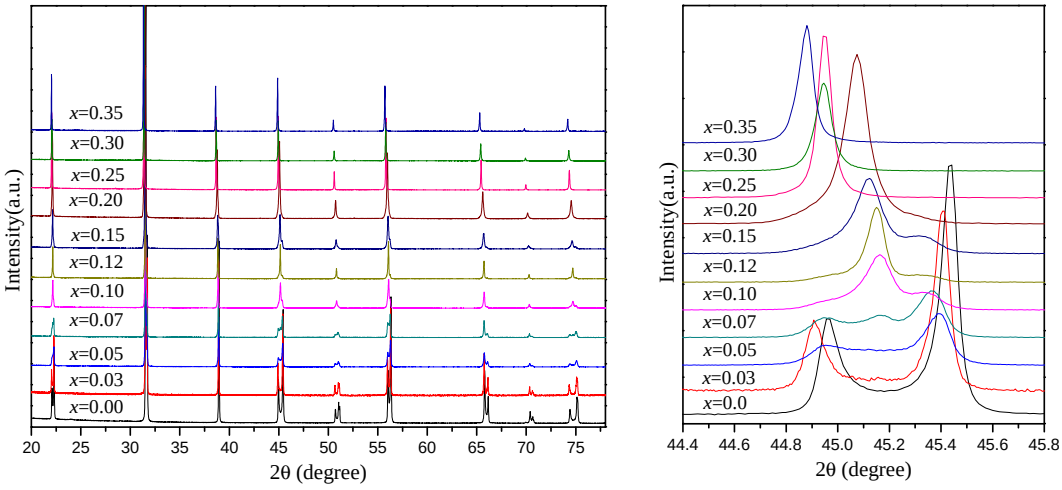

Figure 4-13 Room-temperature x-ray diffraction patterns for BS-BT ceramics as a function of composition.

4.3.1.2 Ambient neutron powder diffraction

To obtain more detailed crystallographic information concerning structural changes as a consequence of doping, Rietveld refinements were performed against the neutron diffraction data recorded at ambient temperature for the different compositions. The phase, for x = 0.03 was refined with a perovskite tetragonal phase (space group: $P4mm$) from a starting model of undoped BT [21]. A reduction in the tetragonality from 1.01030(1) (undoped BT) to 1.01000(1) was seen as a combined effect of decrease in c and increase in a lattice constants. In this refinement, as in all others subsequently, Ba and Bi ions and Sc and Ti ions were constrained at the same sites (A and B sites of the ABO_3 perovskite structure, respectively) and with the same value of the isotropic thermal displacement parameters. It should be mentioned that, when the thermal displacement parameters for all the ions were released together to refine, in some cases the values for Ti/Sc came out as negative and to avoid this non-physical result, the thermal displacement parameters for Ti/Sc were refined keeping the rest fixed. To improve the overall fitting, anisotropic thermal displacement parameters were also tried for different compositions, but that did not provide any sensible improvement and values were below zero on several occasions. It has recently been pointed out [22] that it is difficult to model anisotropic parameters utilizing data with a limited range of d values and, in this case, the minimum d was 0.67 Å.

Co-existence of two phases can be seen starting from $x = 0.05$ till $x = 0.20$, beyond that the tetragonal phase completely transforms to a pseudocubic phase at $x = 0.25$ and higher. The sample with composition $x = 0.30$ was refined assuming a cubic structure with a centro-symmetric space group $Pm\bar{3}m$. The lattice parameters were $a = b = c =$ 4.03624(1) Å. The structures for $0.05 \leq x \leq 0.20$ were refined assuming a model consisting of a tetragonal ($P4mm$) and a rhombohedral phase ($R3m$). A gradual decrease in the tetragonal component of the phase was observed as x increases across the phase diagram. The rhombohedral phase was found to be highly pseudo-symmetric, which is very close to the ideal cubic structure and as doping increased the pseudocubic angle finally reached 90°. Initially, the pattern for $x = 0.07$ was subjected to indexing as a single phase by performing Pawley refinements which provided orthorhombic and monoclinic solutions. However, the whole powder pattern refinement assuming a single-phase model was unsatisfactory. Therefore, having tried various different combinations of crystal systems, the best model to describe the diffraction pattern for $x = 0.07$ was found to be a mixture of a tetragonal and a strongly pseudocubic rhombohedral phase. The rhombohedral phase (space group $R3m$) was refined in the rhombohedral setting assuming Ba and Bi ions fixed at the origin to avoid the floating origin in both $P4mm$ and $R3m$ space groups. The structural parameters obtained from Rietveld refinements are summarized in Table 4-1. The lattice parameters obtained from the refinements of the BS-BT ceramics as a function of composition are shown in figure 4-14. Figure 4-15 shows the observed, calculated and the difference plots achieved from the refinements for $x = 0.03$, 0.07 and 0.30 assuming a single tetragonal, tetragonal+rhombohedral and a cubic phase, respectively.

4.3.1.3 Non-ambient x-ray powder diffraction

4.3.1.3.1 High-temperature x-ray diffraction Investigation of structural phase transition as a function of temperature in a ferroelectric or piezoeletric system is essential because it determines the thermal stability of the properties and hence determines the suitability in different applications. High-temperature x-ray powder patterns were collected for the BS-BT ceramics to follow the structural phase transition as a function of temperature for different values of x. Powder scans were recorded from 25 °C up to 300 °C with an interval of 10 °C during heating. Only one phase transition was ob-

Table 4-1 Refined crystallographic data for xBiScO$_3$(1 − x)BaTiO$_3$ ceramics for the compositions between x = 0.05 and 0.15.

$BiScO_3$ content		x = 0.05		x = 0.07		x = 0.10		x = 0.15	
Space group		*P*4*mm*	*R*3*m*	*P*4*mm*	*R*3*m*	*P*4*mm*	*R*3*m*	*P*4*mm*	*R*3*m*
Phase fraction (%)		65.5	34.5	60.51	39.49	21.59	78.41	15.52	84.48
a (Å)		3.99853(2)	4.01598(7)	4.00017(2)	4.01703(4)	4.00065(5)	4.01740(2)	4.00199(7)	4.02068(2)
b (Å)		3.99853(2)	4.01598(7)	4.00017(2)	4.01703(4)	4.00065(5)	4.01740(2)	4.00199(7)	4.02068(2)
c (Å)		4.03517(4)	4.01598(7)	4.03612(4)	4.01703(4)	4.03657(8)	4.01740(2)	4.0375(1)	4.02068(2)
$\alpha = \beta = \gamma$ (°)		90.0	89.99(2)	90.0	89.99(3)	90.0	90.00(1)	90.0	89.959(3)
Bi/Ba (0,0,0)	U_{iso}	0.23(3)	0.01(1)	0.03(3)	0.2(3)	0.04(5)	0.14(9)	0.14(8)	0.51(6)
Sc/Ti	x	0.5	0.5348(2)	0.5	0.483(4)	0.5	0.525(4)	0.5	0.521(3)
	y	0.5	0.5348(2)	0.5	0.483(4)	0.5	0.525(4)	0.5	0.521(3)
	z	0.492(1)	0.5348(2)	0.493(2)	0.483(4)	0.461(2)	0.525(4)	0.444(3)	0.521(3)
	U_{iso} (Å^2)	0.01(1)	0.05(1)	0.003(4)	0.8(1)	0.01(1)	0.004(4)	0.01(1)	0.01(3)
O1	x	0.5	0.508(2)	0.5	0.495(1)	0.5	0.509(1)	0.5	0.5028(9)
	y	0.5	0.508(2)	0.5	0.495(1)	0.5	0.509(1)	0.5	0.5028(9)
	z	0.0243(9)	0.508(2)	0.023(1)	0.495(1)	-0.0003(2)	0.509(1)	-0.002(3)	0.5028(9)
	U_{iso} (Å^2)	0.25(3)	0.36(4)	0.24(3)	0.06(3)	0.5(1)	0.36(4)	0.8(1)	0.35(2)
O2	x	0.5		0.5		0.5		0.5	
	y	0.0		0.0		0.0		0.5	
	z	0.520(1)		0.520(1)		0.506(2)		0.506(2)	
	U_{iso} (Å^2)	0.13(2)		0.19(2)		0.02(5)		0.06(7)	
Sc/TiO1a (Å)		1.887(7)	1.946(1)	1.898(8)	1.999(2)	1.864(2)	1.968(2)	1.802(2)	1.986(1)
Sc/TiO1b (Å)		2.148(7)	2.081(1)	2.138(8)	2.021(2)	2.173(2)	2.053(2)	2.235(2)	2.040(1)
Sc/TiO2a (Å)		2.0025(4)		2.0030(4)		2.008(1)		2.016(2)	
R_{Bragg}		4.74		3.99		2.89		3.83	
R_{wp}		11.88		12.48		12.65		11.75	
χ^2		3.399		3.168		4.05		3.901	

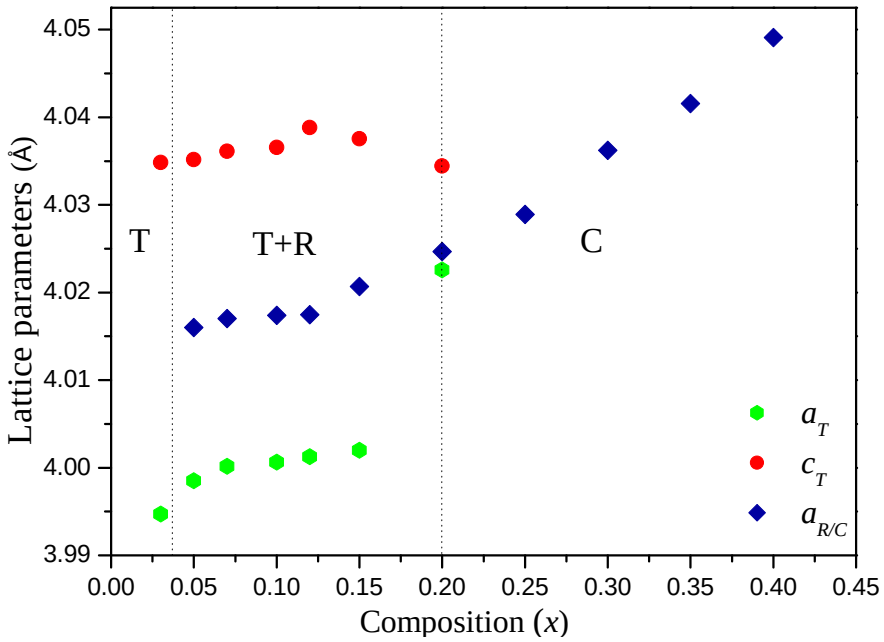

Figure 4-14 Lattice parameters obtained from the refinements for BS-BT ceramics as a function composition. Error-bars are too small to be visisble.

served in the temperature region of 140-200 °C for the BS-BT samples with x between 0.03 and 0.20. Figures 4-16 and 4-17 show the x-ray patterns at different temperatures. A selected region of the 2θ scale in both cases has also been shown to illustrate the variation of the lattice parameters as a function of temperature. The room temperature phases gradually transformed to a cubic system (space group: $Pm\bar{3}m$) and there was no evidence of any intermediate phases between the room-temperature and the high-temperature cubic phases.

4.3.1.3.2 Low-temperature x-ray diffraction Since BT shows two low-temperature phase transitions (fig 4-10), low-temperature diffraction patterns of BS-BT samples with different compositions were collected in the temperature range from room temperature down to −253 °C. Powder patterns were collected during cooling with an interval of 10 °C. Figure 4-18 shows the contour plot of the diffraction data obtained in the temperature range of 17 °C to −253 °C. There is no evidence of any structural change over this range of temperature and the straight lines, which are individual Bragg reflections as a function of temperature, suggest that there is hardly any change in the lattice parameters as well. This phenomenon of suppression of low-temperature phases has been seen previously in BT-based material, such as BiZn$_{1/2}$Ti$_{1/2}$O$_3$-BaTiO$_3$ [23].

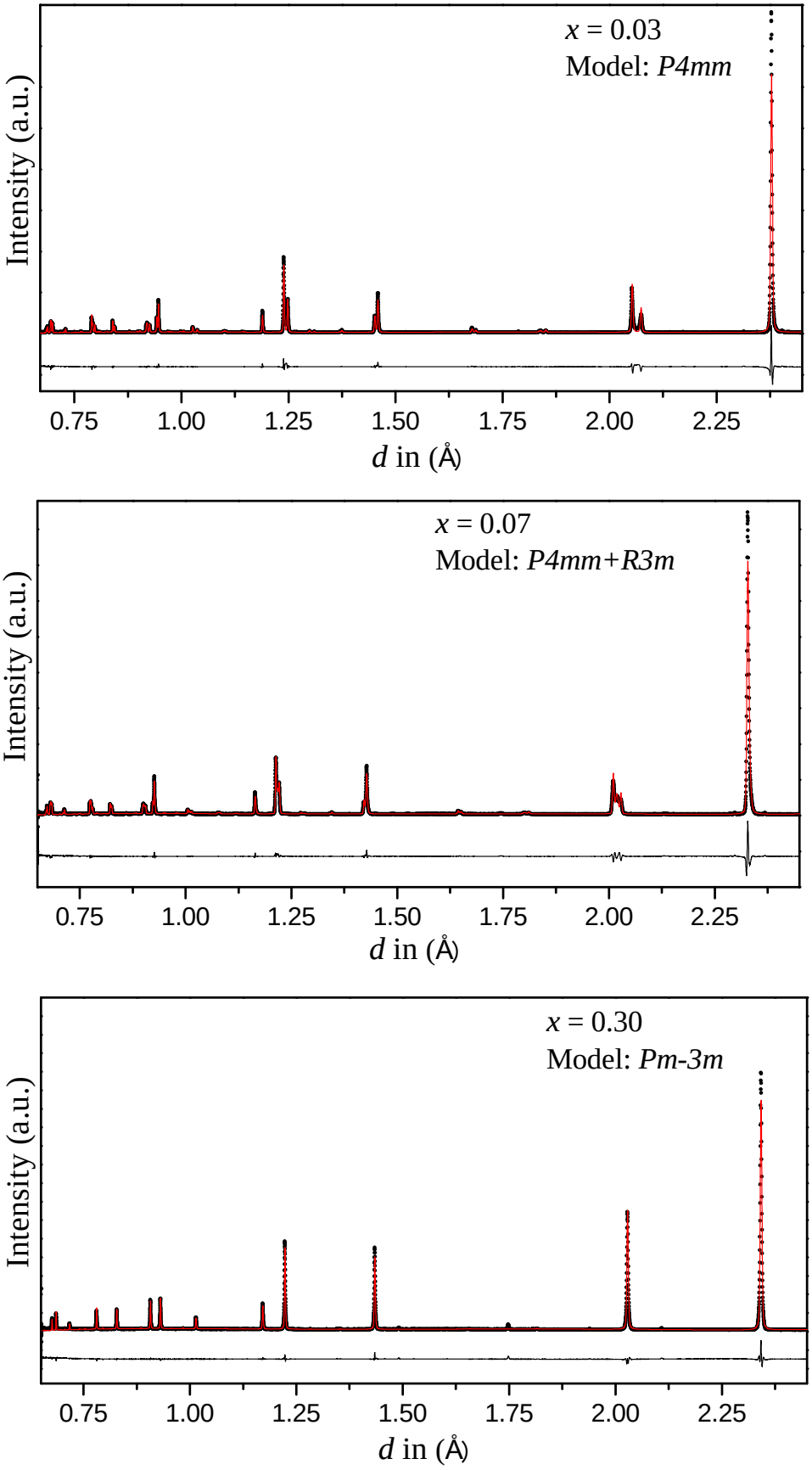

Figure 4-15 Calculated (-), observed (•) and the difference (-) plots of the neutron diffraction patterns obtained from the refinements for BS-BT ceramics with different compositions.

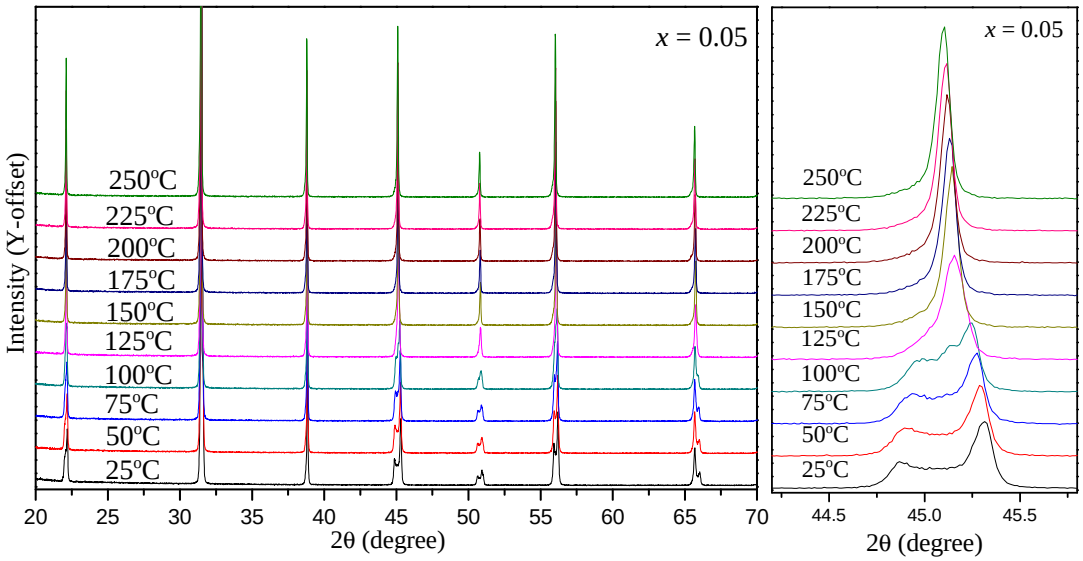

Figure 4-16 High-temperature x-ray diffraction patterns for BS-BT ceramics with x = 0.05

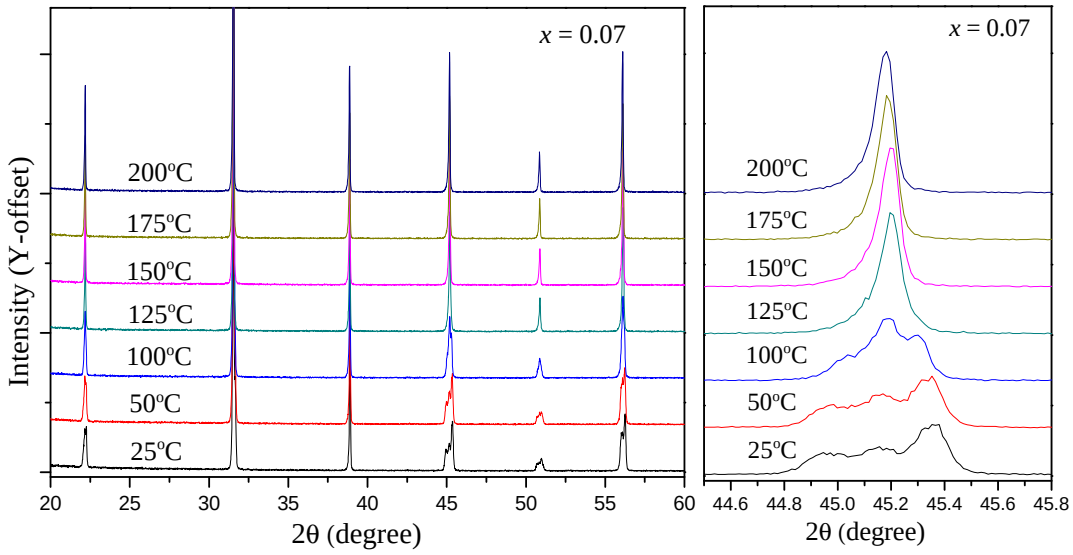

Figure 4-17 High-temperature x-ray diffraction patterns for BS-BT ceramics with x = 0.07

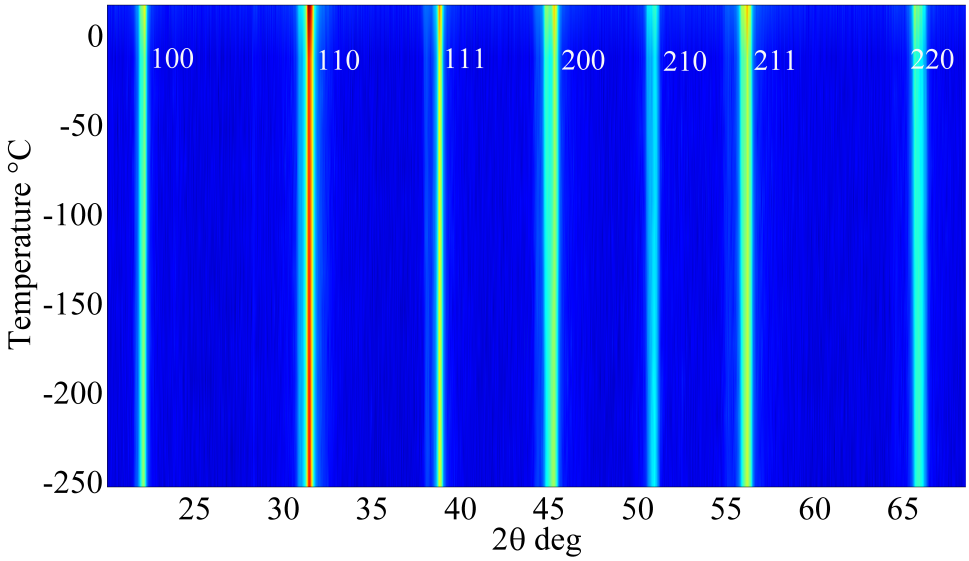

Figure 4-18 Contour plot of the low-temperature diffraction patterns for the sample $x = 0.05$ providing no evidence of structural phase transition in the given range of temperature. This suggests that the incorporation of BS into BT has inhibited the other two low-temperature phase transitions.

4.3.2 Dielectric properties

The real and imaginary parts of the dielectric permittivity for unpoled BS-BT ceramics were calculated from the capacitance and conductance measurements as a function of temperature and frequency. Figure 4-19 shows the temperature dependence of the dielectric constant for six different samples where $x \leq 0.15$. The data have been presented at frequencies between 20 kHz and 100 kHz. The central peak for all the compositions refers to the ferroelectric to paraelectric phase transition. The phase transition temperatures (T_m) for each composition were estimated from the maximum of the dielectric response curve and it is evident that for these samples there has not been much change in the ferroelectric transition temperature or Curie temperatures due to the doping in comparison to the undoped BT which is around 120-130 °C. The maximum dielectric constants observed for these ceramics were between 200 and 1000 depending on the composition. These relatively low values of dielectric constant at the Curie temperature (maximum dielectric constant for undoped BT ~ 10,000-12,000) could be because of high porosity in the samples. It is further important to note that the ceramics with $x \leq 0.15$ do not show any substantial frequency dispersion in the dielectric constant and the transition temperatures are also frequency independent. However it is evident

from figure 4-20 that the variation of ε'' as a function of temperature has been significantly affected by conduction or leakage current. As a consequence of this high leakage the phase transition peak is not distinguishable from these plots for most of the compositions and a high frequency dispersion in ε'' has been seen, especially at high temperatures.

Figure 4-21 shows the temperature dependent ε' and ε'' for the compositions x = 0.20 and 0.25. These two samples have demonstrated relatively broad maxima in the ε' versus T plot with a higher degree of frequency dispersion in ε'. The flattening of the dielectric constant peak could be because of the enhanced compositional inhomogeneity with the increased doping concentration. Similar to the other compositions these samples have also demonstrated high conduction which has subdued the phase transition peak in the ε'' versus T plots.

Similar results on dielectric properties of BS-BT ceramics were reported by Ogihara et al. [14], however we have not observed any 'core-shell' effect as reported by them. This was argued as an effect of inhomogeneity occurred due to prolonged heating of the samples. In addition, the reported low-temperature dielectric data did not show any anomaly due to the structural phase transition in the temperature range of $-100\,^{\circ}$C to $25\,^{\circ}$C, which supports our low-temperature diffraction data. More recently dielectric properties of BS-BT ceramics with x =0.05 and 0.10 were studied by Guo et al. [24] which describes the BS-BT ceramics as re-entrant type relaxors, where the relaxor state occurs after the ferroelectric phase transition upon cooling.

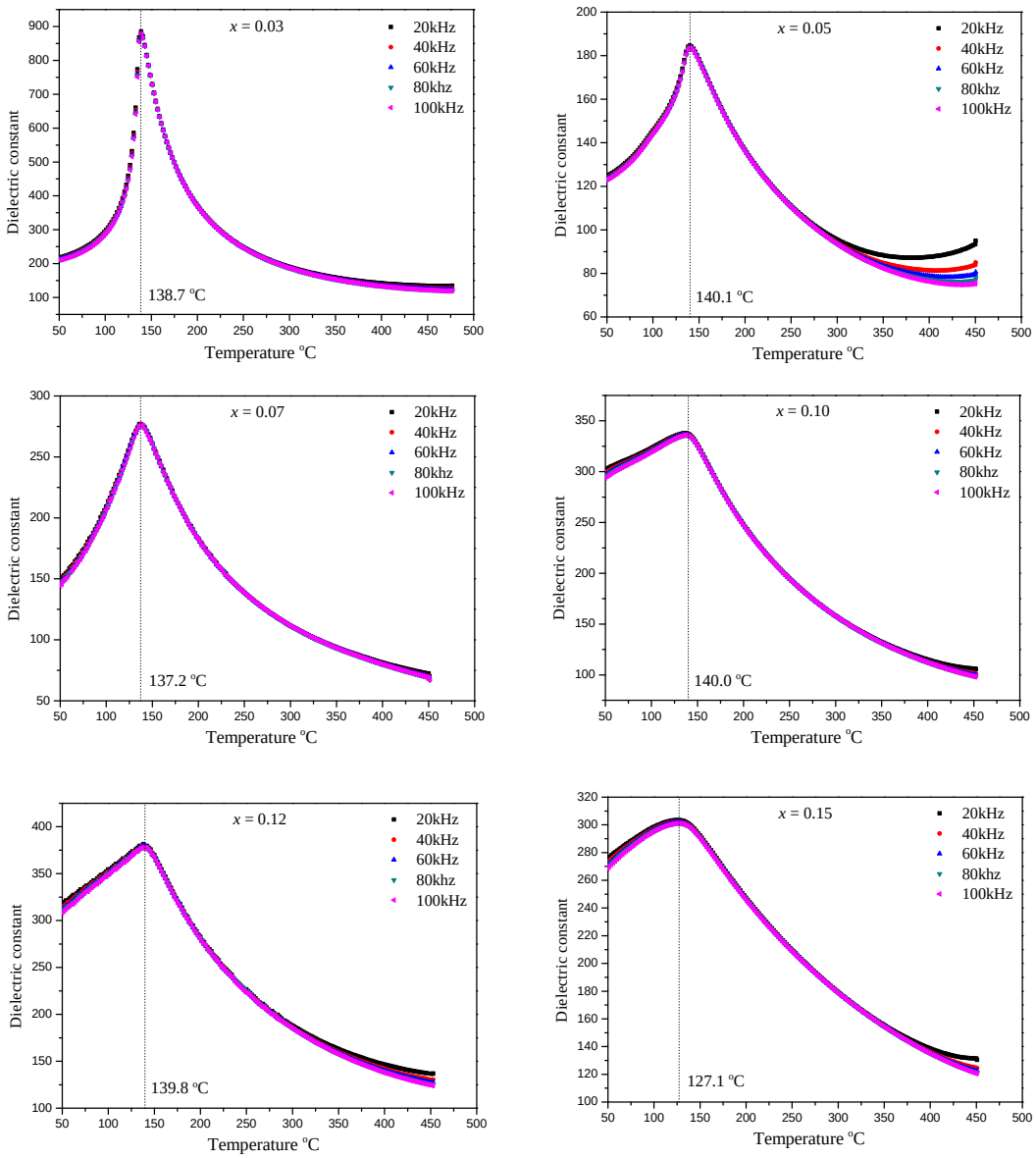

Figure 4-19 Temperature-dependent dielectric constant for BS-BT ceramics for different values of doping concentration (x).

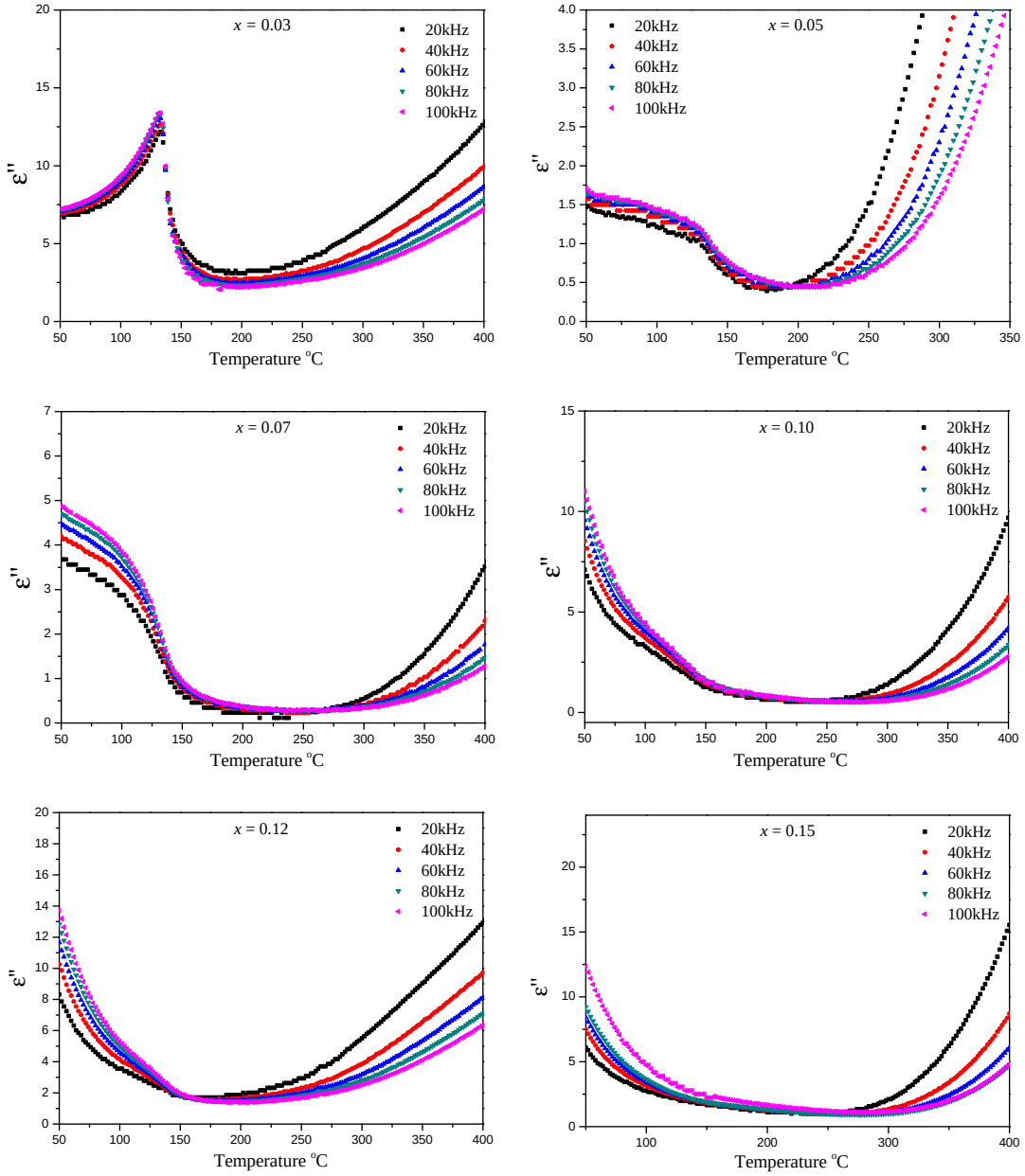

Figure 4-20 Temperature-dependent ε'' for BS-BT ceramics for different values of doping concentration (x).

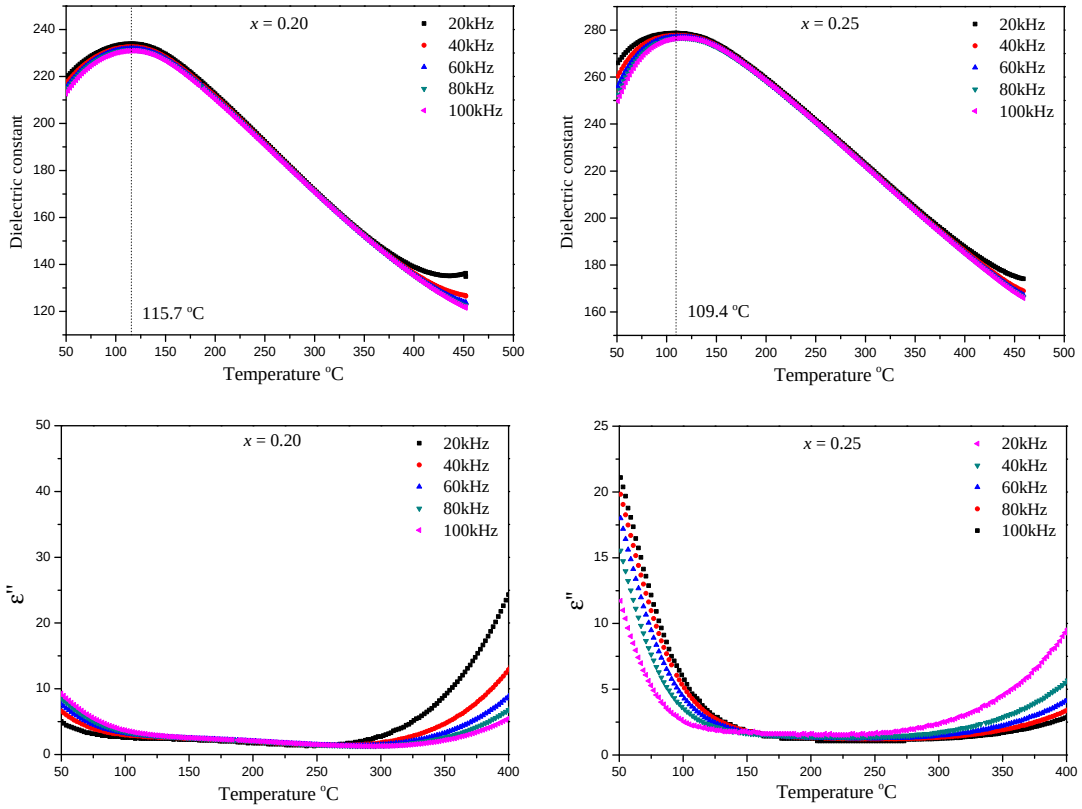

Figure 4-21 Temperature-dependent ε' and ε'' for BS-BT ceramics for x = 0.20 and 0.25. Effect of conduction is evident from the ε'' vs. T plot where phase transition peaks are not distinguishable.

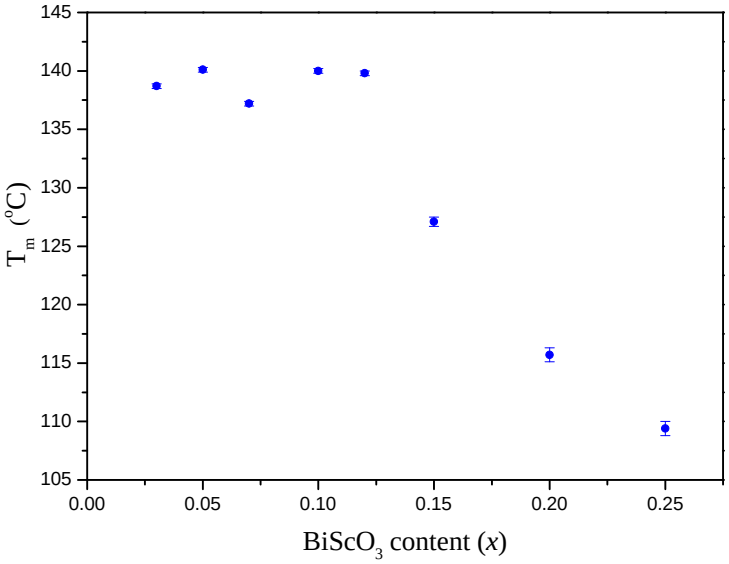

Figure 4-22 Phase transition temperatures (T_m) estimated from the ε' vs T plots as a function of composition.

4.4 Discussions

The structural phase transition in BS-BT ceramics observed as a function of composition is a gradual transformation from the tetragonal to the cubic system through a region of co-existing phases (tetragonal+rhombohedral). The co-existence of these two phases (space groups $P4mm$ + $R3m$) was seen in the region $0.05 \leq x \leq 0.20$. No evidence was found of a single bridging phase between the tetragonal and rhombohedral or cubic phase. For $x \geq 0.25$ the room-temperature phase was transformed into a paraelectric phase with a centro-symmetric space group $Pm\bar{3}m$. Samples for $x \geq 0.10$ showed a monotonic decrease in T_c with the increase of x (fig 4-22).

This behaviour of the structural phase transition as a function of composition is quite distinct from $PbTiO_3$-based solid solutions where intermediate monoclinic phases have been reported in many systems. The existence of a monoclinic phase has also been reported in the BS-PT system [25]. The appearance of monoclinic phases in $PbTiO_3$-based materials has recently been argued as the effect of chemical pressure induced by dopants at ambient pressure [26] and evidence of monoclinic phases in undoped $PbTiO_3$ was found between 10-20 GPa through high pressure x-ray diffraction and Raman spectroscopy. However, when $BaTiO_3$ was studied under high pressure, a tetragonal to pseudocubic phase transition was observed at room temperature [27–29]. In addition, substituents normally induce strain which also plays an important role in structural phase transitions. It was shown theoretically that strain can effectively inhibit the structural phase transitions in BT and a direct cubic (high-temperature phase) to rhombohedral (room temperature phase) phase transition is possible under ambient conditions [30]. Therefore, probably as a consequence of the induced strain upon doping, in many $BaTiO_3$-based solid solutions (either A-site or B-site or both A and B substituted) a direct tetragonal to pseudocubic phase transition is normally observed and this also suppresses the other phase transitions of BT at low temperature. Although the diminution of tetragonality seems to be a general tendency for BT-based solid solutions, it should be noted that some exceptions exist, where enhancement of the tetragonality was seen, such as, when $BaTiO_3$ is doped with $Na_{0.5}Bi_{0.5}TiO_3$ [31] and $PbTiO_3$ [32].

References

[1] Y. Y. Tomashpolski, E. V. Zubova, K. P. Burdina, , and Y. N. Venettsev, Soviet Physics Crystallography **13**, 859 (1969).

[2] R. E. Eitel, C. A. Randall, T. R. Shrout, P. W. Rehrig, W. Hackenberger, and S. E. Park, Jpn. J. Appl. Phys. **40**, 5999 (2001).

[3] R. Zuo, C. Ye, , and X. Fang, Jpn. J. Appl. Phys. **46**, 6733 (2007).

[4] H. Du, W. Zhou, F. Luo, D. Zhu, S. Qu, Y. Li, and Z. Pei, J. Appl. Phys. **104**, 044104 (2008).

[5] H. Du, W. Zhou, F. Luo, D. Zhu, S. B. Qu, Y. Li, and Z. Pei, J. Appl. Phys. **104**, 034104 (2008).

[6] E. Boucher, P. Marchet, and J. Mercurio, J. Phys. IV France **128**, 3 (2005).

[7] T. A. Skidmore, T. P. Comyn, and S. J. Milne, J. Am. Ceram. Soc. **93**, 624 (2010).

[8] X. Li, J. Zhu, M. Wang, Y. Luo, W. Shi, L. Li, J. Zhu, and D. Xiao, J. Alloy. Comp. **499**, 1 (2010).

[9] X. Sun, J. Deng, C. Sun, J. Li, J. Chen, R. Yu, G. Liu, X. Xing, and L. Qiaoz, J. Am. Ceram. Soc. **92**, 1853 (2010).

[10] D. I. Woodward, I. M. Reaney, R. E. Eitel, and C. A. Randall, J. Appl. Phys. **94**, 3313 (2003).

[11] T. Comyn, S. McBridea, and A. Bell, Materials Letters **58**, 3844 (2004).

[12] M. M. Kumar, A. Srinivas, and S. V. Suryanarayana, J. Appl. Phys. **87**, 855 (2000).

[13] D. S. Tinberg and S. Trolier-Mckinstry, J. Appl. Phys. **101**, 024112 (2007).

[14] H. Ogihara, C. A. Randall, and S. Trolier-Mckinstry, J. Am. Ceram. Soc. **92**, 110 (2009).

[15] H. Ogihara, C. A. Randall, and S. Trolier-Mckinstry, J. Am. Ceram. Soc. **92**, 1719 (2009).

[16] J. B. Lim, S. Zhang, N. Kim, and T. R. Shrout, J. Am. Ceram. Soc. **92**, 679 (2009).

[17] C. C. Huang, D. P. Cann, X. Tan, and N. Vittayakorn, J. Appl. Phys. **102**, 044103 (2007).

[18] Z. Yao, H. Liu, Y. Liu, Z. Li, X. Cheng, M. Cao, and H. Hao, J. Ceram. Soc. Japan **116**, 1150 (2008).

[19] K. Uchino, *Ferroelectric Devices* (CRC Press, 2000).

[20] K. C. Kao, *Dielectric Phenomena in Solids* (Elsevier Academic Press, 2004).

[21] G. H. Kwei, A. C. Lawson, S. J. L. Billinge, and S. W. Cheong, J. Phys. Chem. **97**, 2368 (1993).

[22] H. Yokoto, N. Zhang, A. E. Taylor, P. A. Thomas, and A. M. Glazer, Phys. Rev. B **80**, 104109 (2009).

[23] C. C. Huang and D. P. Cann, J. Appl. Phys. **104**, 024117 (2008).

[24] H. Y. Guo, C. Lei, and Z. G. Ye, Appl. Phys. Lett. **92**, 172901 (2008).

[25] J. Chaigneau, J. M. Kiat, C. Malibert, and C. Bogicevic, Phys. Rev. B **76**, 094111 (2007).

[26] M. Ahart, M. Somayazulu, R. E. Cohen, P. Ganesh, P. Dera, H. Mao, R. Hemley, Y. Ren, P. Liermann, and Z. Wu, Nature **451**, 545 (2008).

[27] G. A. Samara, Phys. Rev. **151**, 378 (1966).

[28] E. V. Mejia-Uriarte, R. Y. Sato-Berru, M. Navarrete, M. Villagran-Muniz, C. Medina-Gutierrez, C. Frausto-Reyes, and H. Murrieta, Meas. Sci. Technol. **17**, 1319 (2006).

[29] U. D. Venkateswaran, V. M. Naik, and R. Naik, Phys. Rev. B **58**, 14256 (1998).

[30] W. Zhong, D. Vanderbilt, and K. M. Rabe, Phys. Rev. Lett. **73**, 1861 (1994).

[31] K. Datta, K. Roleder, and P. A. Thomas, J. Appl. Phys. **106**, 123512 (2009).

[32] G. Shirane and K. Suzuki, J. Phys. Soc. Japan **6**, 274 (1951).

Chapter 5

Structural investigation of $x(Na_{1/2}Bi_{1/2})TiO_3$-(1-x)$BaTiO_3$

5.1 Introduction

Continuing the investigation of the influence of Bi ion in $BaTiO_3$, Bi has been added in BT along with Na ion, which essentially means the formation of a solid solution between $Na_{1/2}Bi_{1/2}TiO_3$ and $BaTiO_3$. When BT was studied with the A site partially substituted by only Bi, it was found that there exists a solubility limit which is 3-5% of Bi and beyond that a second phase, $Bi_2Ti_2O_7$, is developed [1, 2].

$Na_{1/2}Bi_{1/2}TiO_3$ (NBT) developed by Smolensky [3], is an example of a perovskite-based ferroelectric material, which has a rhombohedral structure on average at room temperature [4–6]. NBT has attracted much interest because of its unusual optical and dielectric properties in comparison with other perovskite-based systems. After four decades of investigations, controversy still exists about the basic properties of NBT, such as the number of different crystallographic phases, their polar order and the temperature range of phase existence or coexistence [5, 7–14].

NBT is considered to be an attractive candidate as a lead-free piezoelectric material since it has demonstrated superior ferroelectric and piezoelectric properties over a wide range of temperatures [15]. However a complex sequence of structural phase transition below the Curie temperature (fig 5-1) and a high coercive field ($\sim$ 73kV/cm) are significant disadvantages of this material.

NBT has demonstrated excellent properties in solid solutions with $BaTiO_3$ and $K_{1/2}Bi_{1/2}TiO_3$ [17]. In particular, the solid solution with BT has been shown to have enhanced physical properties corresponding to a rhombohedral-tetragonal phase boundary (MPB) when the composition is close to 0.94NBT-0.06BT [18]. Therefore many

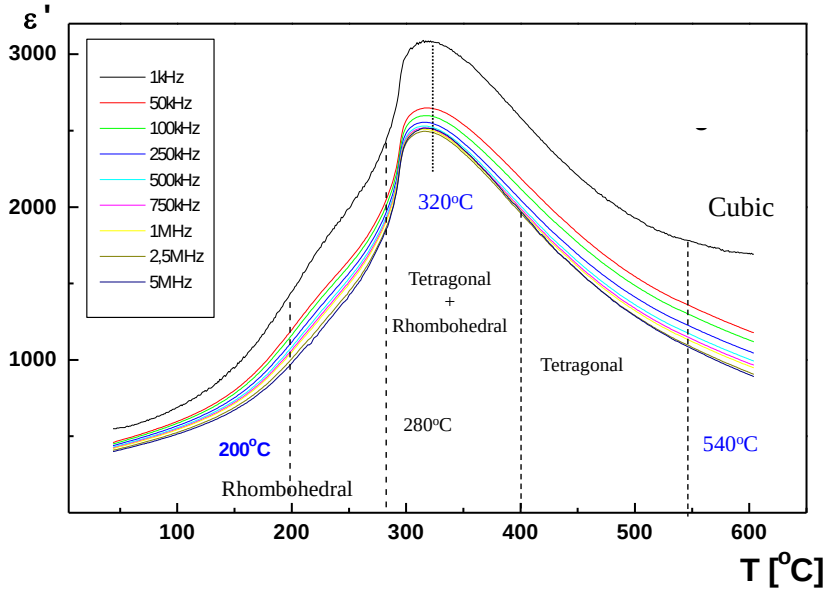

Figure 5-1 The low-frequency temperature dependence of the dielectric constant for NBT ceramics reported by Roleder et al. [16]. Dashed lines indicate points at which piezoelectric anomalies were observed. Structural details as a function of temperature was published by Jones and Thomas [5].

studies [19–25] of the NBT-BT system have been performed near the MPB, i.e. the NBT-rich end of the phase diagram and, to date, few studies have been reported on the BT-rich end of this system [26]. Figure 5-2 shows the phase diagram of the NBT-BT system published by Takenaka et al. [18] who reported the existence of an antiferroelectric phase based on dielectric and piezoeletric measurements. However, Suchanicz et al. [27] later described the antiferroelectric region as coexistence of polar tetragonal regions in a non-polar cubic matrix and Qu et al. [28] suggested coexistence of trigonal and tetragonal states with alternating polar micro domains to explain the deformed hysteresis loops of the antiferroelectric states. Very recently, ceramics of xNBT-(1-x)BT for $1.0 \leq x \leq 0.90$ have been studied and it has been argued that 'lattice-distortion' plays a key role in the enhancement of d_{33} values in the vicinity of rhombohedral-tetragonal phase boundary. Both rhombohedral (90-α) and tetragonal (c_T/a_T) lattice distortions become smaller at the phase boundary causing poling by field and depoling by temperature easier and subsequently resulting in higher d_{33} (fig 5-3).

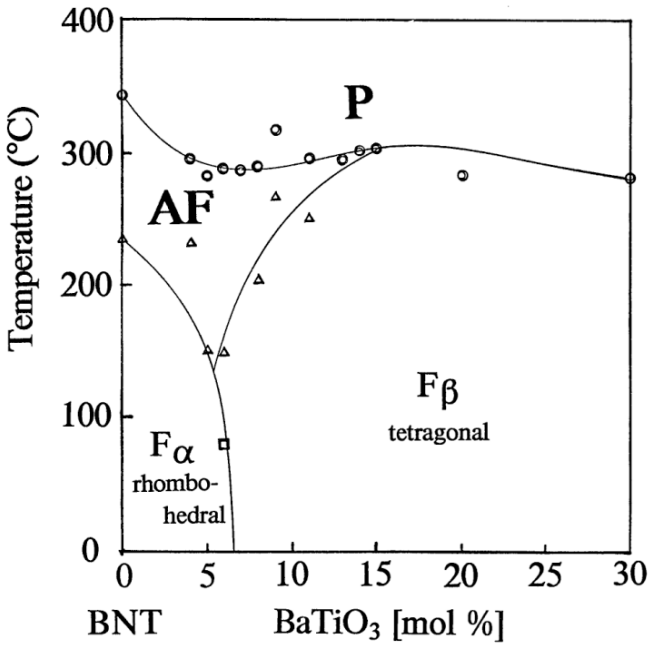

Figure 5-2 Phase diagram of NBT-BT as reported by Takenaka et al. [18] where Fα is ferroelectric rhombohedral phase, Fβ is ferroelectric tetragonal phase, AF is antiferroelectric phase and P is paraelectric phase.

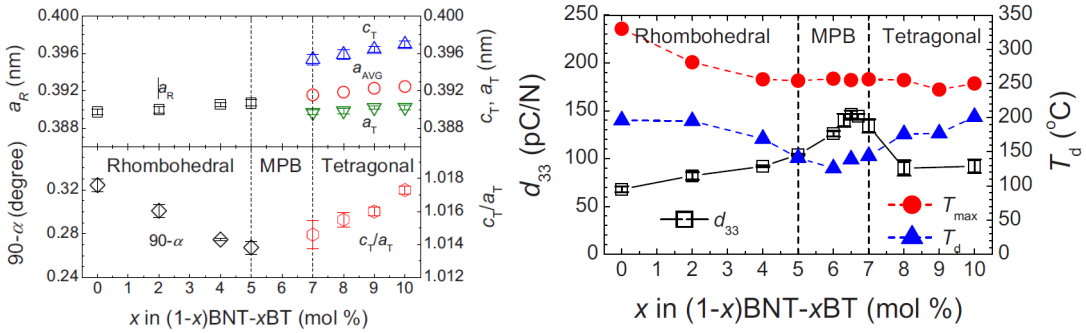

Figure 5-3 (a) Compositional dependence of lattice parameters of NBT-BT ceramics. (b) Composition dependence of d_{33}, T_d and T_{max} at 100 kHz. The figures have been taken from the article by Sung et al. [29].

In this chapter, the structure and the dielectric properties of xNBT-(1-x)BT ceramics are reported for $x \leq 0.40$. The incorporation of NBT into BT is shown to result in an increased tetragonal axial ratio (c/a) of the unit cell, which attains a maximum of 1.019 when $x = 0.40$. From detailed structural analysis obtained through Rietveld refinement, it is understood that the enhancement of the tetragonality does not occur because of the larger off-centering of the B ion (Ti^{+4}) in the perovskite cell, but rather as an effect of a decrease in the oxygen-octahedral volume which effectively raises the tetragonality. From the dielectric study an accompanying rise in ferroelectric to paraelectric transition temperatures (T_c) was seen with increasing NBT concentration.

5.2 Experimental

5.2.1 Synthesis and physical characterization:

Ceramics of NBT-BT with different compositions were prepared through the conventional solid-state synthesis route. The starting materials were $BaCO_3$ (Alfa Aesar), TiO_2 (Alfa Aesar), Bi_2O_3 (Alfa Aesar) and Na_2CO_3 (Alfa Aesar) having purity $\sim$ 99.99%. The amount of starting materials for different stoichiometric ratios of the samples were calculated from the following equations :

$$Na_2CO_3 + Bi_2O_3 + 4TiO_2 = 4Na_{1/2}Bi_{1/2}TiO_3 + CO_2 \quad (5\text{-}1)$$

$$BaCO_3 + TiO_2 = BaTiO_3 + CO_2 \quad (5\text{-}2)$$

5.2.2 X-ray powder diffraction

High resolution x-ray powder diffraction on NBT-BT ceramics was performed utilizing a PANalytical X'Pert Pro MPD equipped with a curved Johansson monochromator giving focused pure Cu$K\alpha_1$ radiation, axial divergence controlled by a 0.02 rad soller slit in the diffracted beam. Data were collected using a PIXcel detector (active length = 3.347° in 2θ) with step size of 0.013° in the range 20°-90° 2θ in Bragg-Brentano geometry.

5.2.3 Neutron powder diffraction

Neutron powder diffraction scans (time of flight data) were collected at the ISIS facility using the high-resolution powder diffractometer (HRPD). Approximately 15 g of powder were loaded into a cylindrical vanadium can and data collected for a total count of 40 μA of current. Data collected at the back-scattering bank were used for Rietveld refinement.

5.3 Results and discussions

5.3.1 Structural investigation

5.3.1.1 Ambient X-ray powder diffraction

Room temperature x-ray powder patterns were collected for nine different compositions of NBT-BT ceramics including undoped $BaTiO_3$. Figure 5-4 shows the powder patterns in the compositional range between x = 0.0 and 0.30. This confirms the formation of a single perovskite phase in this range of composition and the patterns could be indexed with a primitive tetragonal unit cell of volume approximately 4×4×4 Å^3. There was no evidence of any superlattice reflection suggesting that there is neither cation ordering nor tilting of the octahedra as a consequence of the doping. Figure 5-5 demonstrates the ambient temperature x-ray diffraction patterns for samples with x = 0.35 and 0.40. This has been shown separately since these two compositions show evidence of secondary phases. The additional peaks for x = 0.35 and 0.40 were identified as Ba- and Bi-based pyrochlore phases, such as $Bi_2Ti_2O_7$ or Ba_2TiO_4, which account for the majority of the additional peaks.

The primary conclusion from the x-ray diffraction results would be that the fundamental structure of BT remains unaltered due to the doping of NBT till x = 0.40. In addition, an enhancement of the tetragonality can easily be anticipated from figure 5-4 which also demonstrates the gradual increase in the separation of the (200) and (002) peaks as a function of x. Another important observation made from the x-ray diffraction patterns is that there are distinct changes in the width and intensity of the peaks from each Bragg reflection as a function of composition. The (111) singlet was fitted individually with a Pseudo-Voigt function for each composition from x = 0.0 to x =

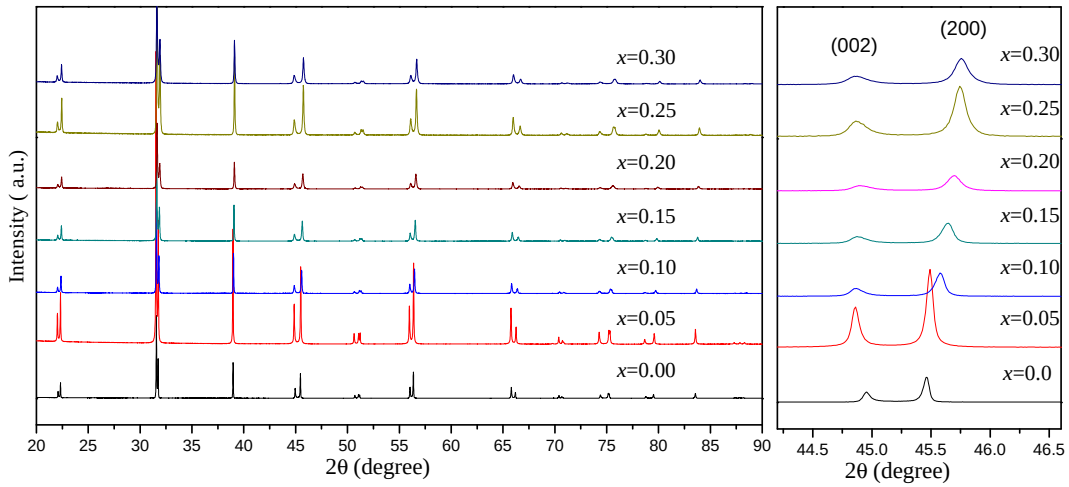

Figure 5-4 Room-temperature x-ray diffraction patterns for NBT-BT ceramics as a function of composition confirms the formation of a single perovskite phase in the given compositional range. A gradual increase in separation of (200) and (002) peaks suggests an increase in the tetragonal axial ratio of the unit cell.

0.40. A gradual increase in FWHM along with a decrease in the intensity was observed (fig 5-6). In general, peak broadening can be modelled as an effect of the finite size of the diffracting crystallites. However, in this case the A-site of the perovskite has a random distribution of three different elements with a slight mismatch in their ionic radii (Bi^{+3} = 1.34 Å, Ba^{+2} = 1.61 Å, Na^{+1} = 1.39 Å), it is therefore very likely that the system contains defects such as micro-distortion or stacking faults that are additionally responsible for the broadening.

5.3.1.2 Ambient neutron powder diffraction

Neutron diffraction is crucial in this particular system to probe the lighter atom oxygen (Z=8) in the presence of heavy atoms like Ba (Z = 56) and Bi (Z = 83). Therefore, in order to investigate the effect of doping at the atomic level, Rietveld refinements were performed against the neutron powder diffraction data. Refinements were done using Topas Academic [30] for compositions from x = 0 to x = 0.4. A Crystallographic Information File (CIF) for perovskite $BaTiO_3$ [31] was used as a starting model to refine against the data for x = 0. For the doped samples, the starting models were obtained from the refined structure of the previous composition. In NBT-BT solid solutions Ba^{+2}, Bi^{+3} and Na^{+1} ions are assumed to share the A-site in the ABO_3 perovskite-type struc-

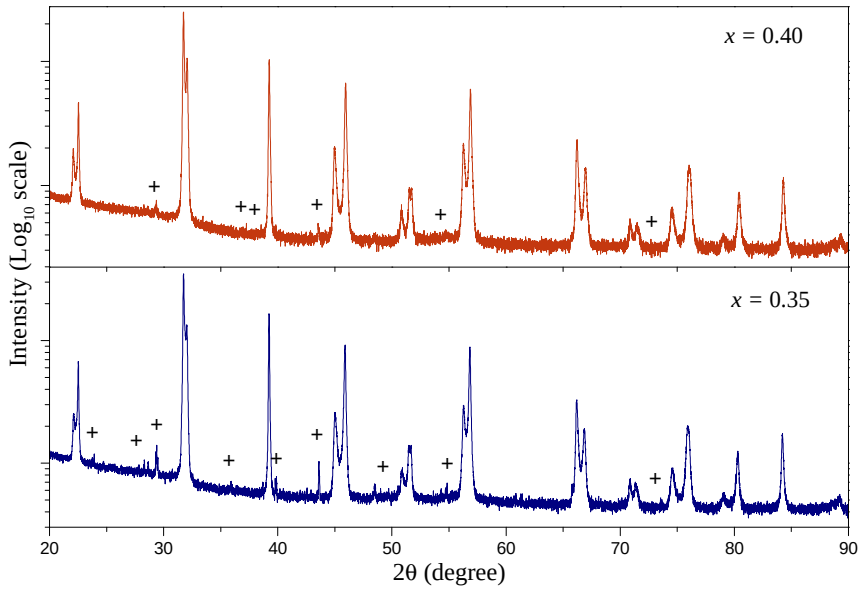

Figure 5-5 Room-temperature x-ray diffraction patterns for NBT-BT samples having x = 0.35 and x = 0.40. The Y-scale has been plotted in log scale to emphasize the presence of extra peaks in the background. (+) signs indicate the peaks which do not belong to the primary perovskite phase.

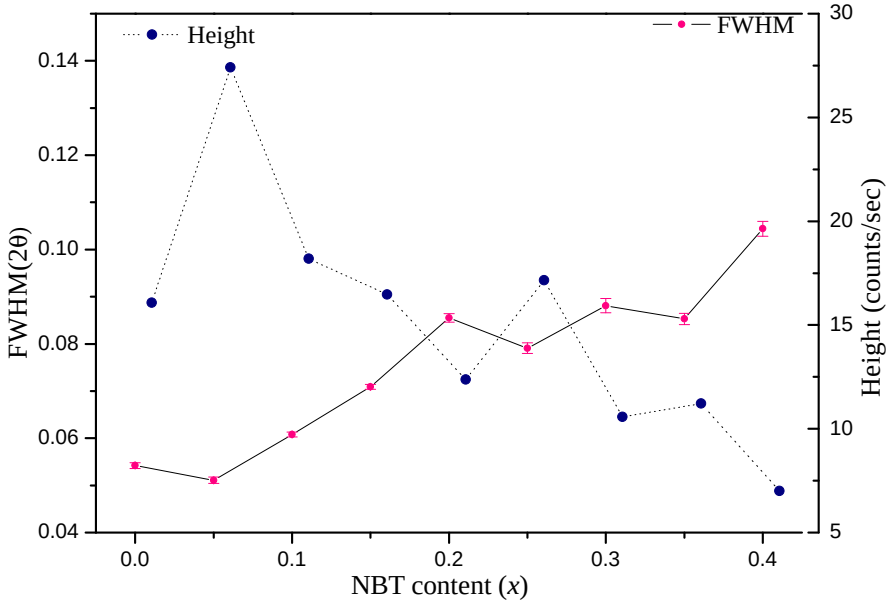

Figure 5-6 Variation of the FWHM of the (111) Bragg peak as a function of composition. Each pattern was recorded in identical experimental condition.

ture. In refinements, all three ions were fixed at (0,0,0) in the space group *P*4*mm* to prevent a floating origin . The *z* coordinates of the oxygens and the Ti ion were refined along with the isotropic thermal displacement parameters (U_{iso}) for all elements. The refinements converged quickly with a goodness of fit (GOF) in the range between 3.6 and 5.2 depending on the composition. Isotropic thermal parameters were assumed because of the inaccessibility of a wide range of *d*-values; for all sets of data the minimum value of *d* was 0.65 Å, which is insufficient to allow meaningful refinement of anisotropic displacement parameters (ADPs) in these systems [32]. U_{iso}s for Ba^{+2}, Bi^{+3} and Na^{+1} were initially constrained to the same values. However, to ameliorate the goodness of fit (GOF), those parameters were allowed to refine independently, but no improvement was found. In some cases, the U_{iso} refined to negative values, even for undoped BT, which is physically unrealistic. This is interpreted as the consequence both of the truncation of the data at the relatively high *d*-value of 0.65 Å and the consequences of absorption. When an absorption correction was included in the refinement, the values of U_{iso} became positive; however, this did not improve the GOF and worsened the R_{Bragg}. The combination of significant chemical disorder (site-sharing by three species on the A-site) with a truncated data set means that the extraction of further detail concerning the extent and anisotropy of the thermal vibrations is not possible. Fractional values of compositions were also released to be refined, but the GOF was not improved and the parameters were fixed to reproduce the expected composition. The crystallographic data obtained from the refinements are summarized in Table 5-1.

As pointed out earlier, though there was no structural phase transition due to the doping , an increase in the tetragonality of the unit cell (*c*/*a* ratio of the unit cell) was noticed with increasing *x* (fig 5-8). In BT, the tetragonal distortion occurs with an off-centering of the Ti ion, which is also responsible for the existence of the spontaneous polarization at room temperature. Therefore, to understand the coupling between the shifts of the Ti ion from its ideal position and the tetragonality of the unit cell in NBT-BT ceramics, the displacements were calculated from the Ti-O bond lengths (fig 5-10) and it is evident from fig 5-8 that the coupling between these two parameters is not linear. It should be noted that a plot of the individual lattice parameters, *a* and *c*, (fig 5-9) shows that there are two different contributions to the increase in the tetragonality as a function of doping. When the doping concentration is below 15% both an increase in *c*

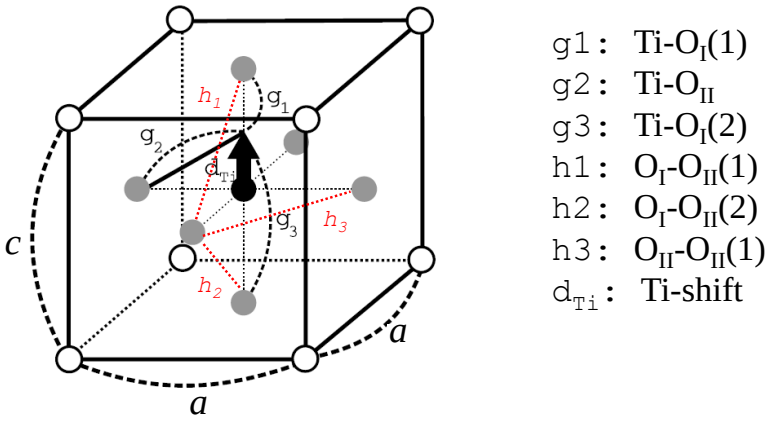

Figure 5-7 Schematic representation of various bonds in a tetragonal perovskite unit cell.

and decrease in a contribute to the enhancement of the axial ratio. However above x = 0.15, a gradual decrease in c and also decrease in a are observed and it is the contraction in a which effectively raises the tetragonality. The contraction in the non-polar directions can also be anticipated from the behaviour of the Ti-O_{II} and O_{II}-O_{II} bond lengths as a function of doping (fig 5-10 and fig 5-11, respectively). Also, the O-O bondlengths in the oxygen octahedra of the perovskite reflect a gradual decease in octahedral volume with the increase of x. The final calculated patterns obtained from the refinements of the diffraction data for NBT-BT ceramics are shown in figure 5-12.

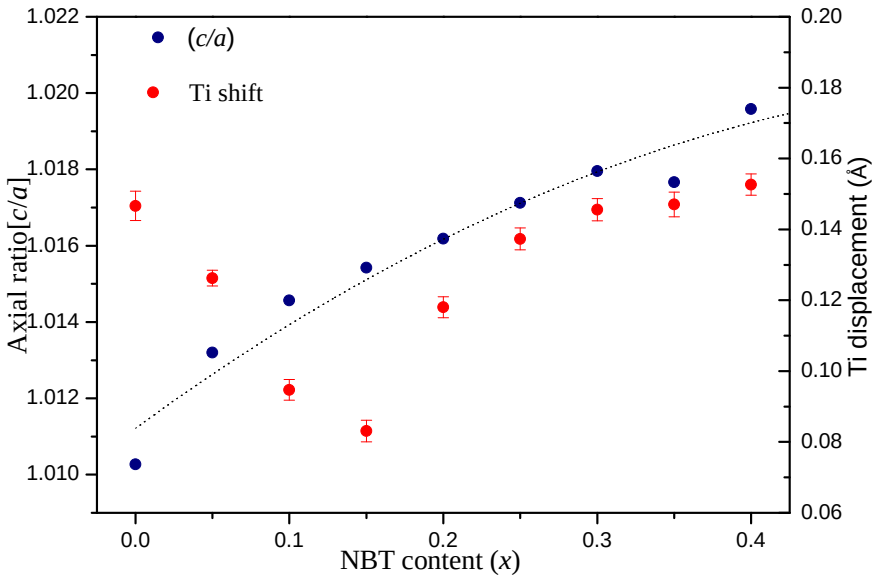

Figure 5-8 Tetragonal axial ratio and Ti-O bond-lengths of the perovskite structure as a function of composition (x).

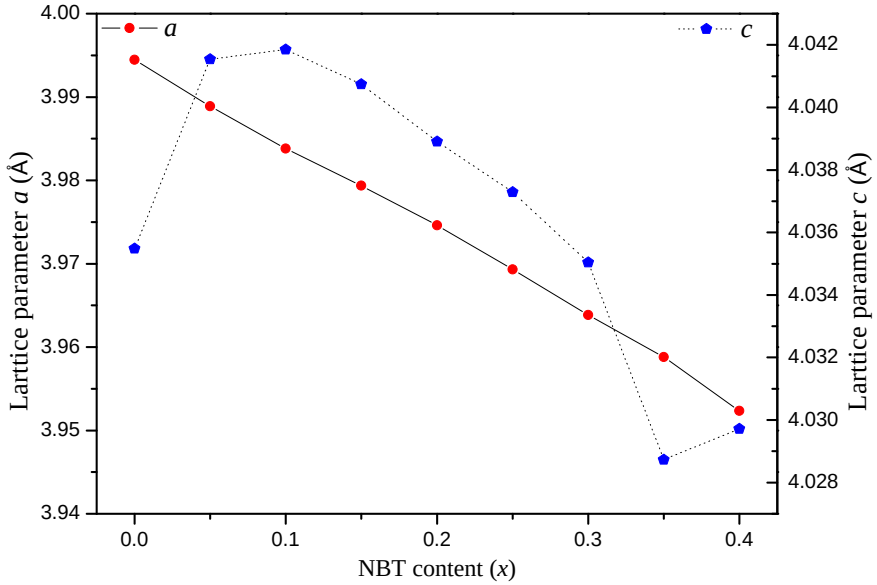

Figure 5-9 Tetragonal lattice parameters for NBT-BT samples as a function of composition (x).

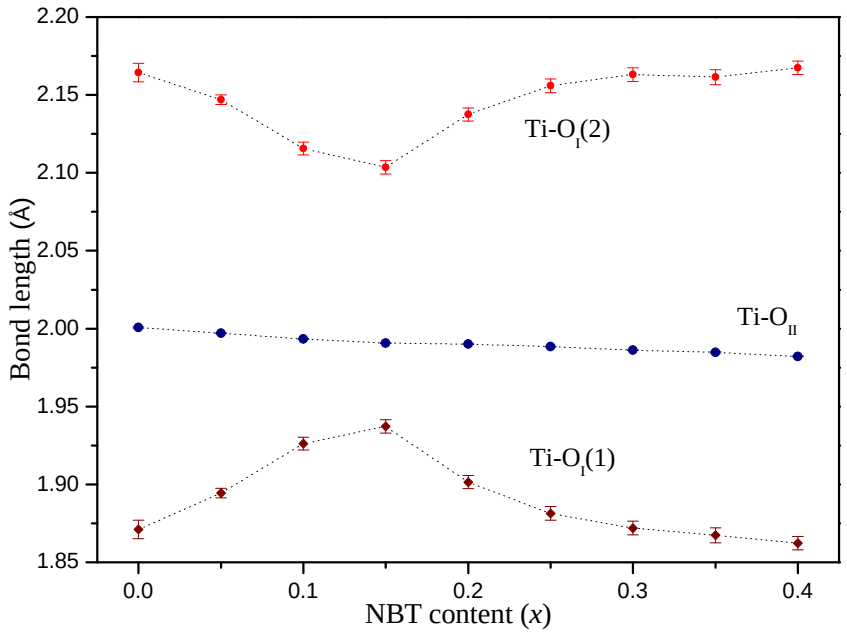

Figure 5-10 Three different Ti-O bond-lengths in the perovskite structure obtained from the refinement as a function of composition (x).

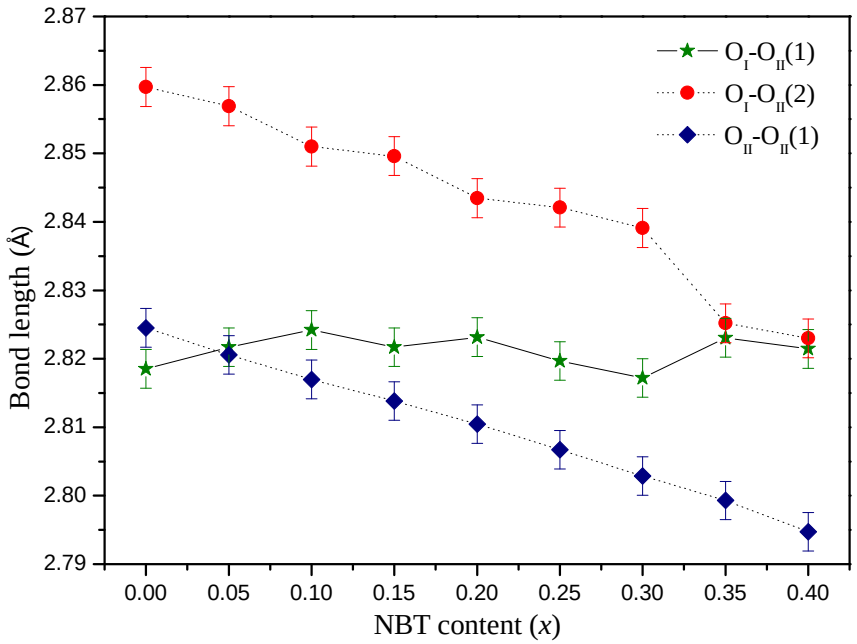

Figure 5-11 Different O-O bond-lengths in the perovskite structure obtained from the refinement as a function of composition (x).

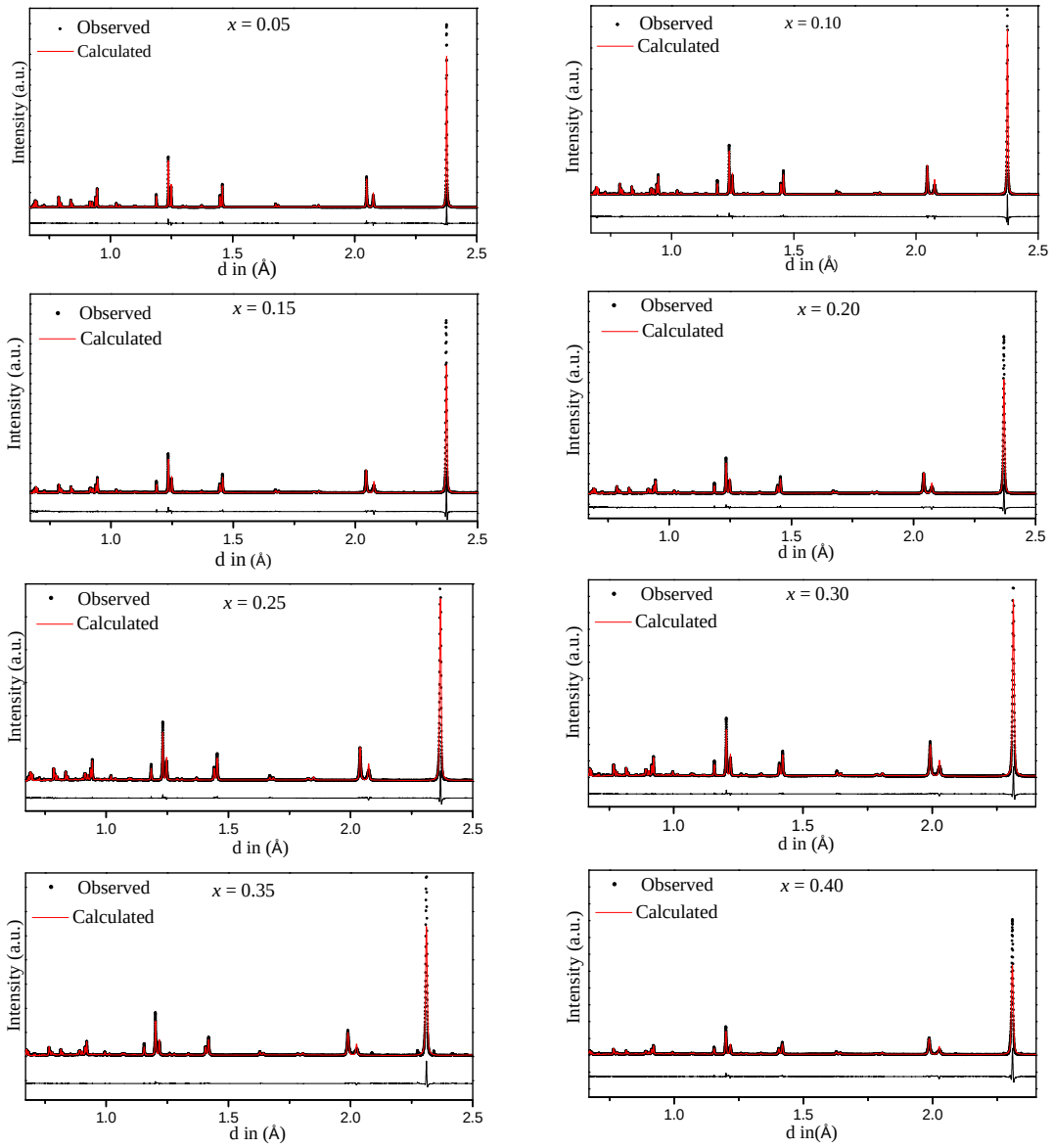

Figure 5-12 Observed (•), calculated(-) and difference (-) plots of the neutron diffraction patterns obtained after Rietveld refinements for different compositions of NBT-BT ceramics.

Table 5-1 Refined crystallographic data for $xNa_{1/2}Bi_{1/2}TiO_3(1-x)BaTiO_3$ ceramics for $0.05 \leq x \leq 0.40$ at room-temperature.

$Na_{1/2}Bi_{1/2}TiO_3$ content	$x = 0.0$	$x = 0.05$	$x = 0.10$	$x = 0.15$	$x = 0.20$	$x = 0.25$	$x = 0.30$	$x = 0.35$	$x = 0.40$
Space group					*P*4*mm*				
$a = b$ (Å)	3.99447(1)	3.98889(1)	3.98382(2)	3.97937(2)	3.97459(2)	3.96932(3)	3.96386(3)	3.95881(3)	3.95233(3)
c (Å)	4.03547(2)	4.04154(2)	4.04185(3)	4.04074(3)	4.03891(4)	4.03729(4)	4.03504(4)	4.02873(6)	4.02972(5)
c/a	1.0103	1.0132	1.0146	1.0154	1.0162	1.0171	1.0179	1.0177	1.0196
Cell Volume (Å^3)	64.389	64.306	64.147	63.987	63.804	63.609	63.399	63.139	62.947
Phase density	6.0141(6)	5.9943(4)	5.9815(6)	5.9688(8)	5.9581(9)	5.9485(1)	5.9403(1)	5.9367(1)	5.9266(1)
Ti(0.5,0.5,z)	0.490(1)	0.5008(7)	0.5125(9)	0.5175(9)	0.5112(9)	0.5113(9)	0.5114(9)	0.51684(9)	0.5196(8)
O1 (0.5,0.5,z)	0.0271(7)	0.0320(4)	0.0359(5)	0.0381(5)	0.0404(5)	0.0453(6)	0.0475(6)	0.0533(7)	0.0575(6)
O2 (0.5,0,z)	0.5199(9)	0.5259(4)	0.5312(5)	0.5332(5)	0.5369(6)	0.5414(5)	0.5437(5)	0.5529(6)	0.5577(6)
U_{iso} (Ba, Bi, Na) (Å^2)	-0.006(23)	0.32(2)	-0.34(2)	-0.36(2)	0.06(3)	0.76(3)	0.54(4)	1.06(5)	1.26(5)
U_{iso} (Ti) (Å^2)	0.27(3)	0.79(2)	0.47(3)	0.58(3)	0.45 (3)	0.42(4)	0.46(4)	0.29(4)	0.41(4)
U_{iso} (O1) (Å^2)	0.24(3)	0.74(2)	0.22(2)	0.21(2)	-0.24(2)	0.33(2)	0.52(3)	-0.11(3)	-0.01(2)
U_{iso} (O2) (Å^2)	0.14(2)	0.55(2)	0.06(1)	0.14(2)	0.21(2)	-0.33(1)	-0.20(1)	-0.16(2)	0.01(2)
TiO2 (Å)	2.0007(3)	1.9970(1)	1.9933(1)	1.9906(1)	1.9900(2)	1.9887(2)	1.9862(2)	1.9847(3)	1.9821(3)
TiO1a (Å)	1.871(6)	1.894(3)	1.926(4)	1.937(4)	1.901(4)	1.877(4)	1.872(4)	1.867(5)	1.862(4)
TiO1b (Å)	2.164(6)	2.147(3)	2.115(4)	2.103(4)	2.137(4)	2.159(4)	2.163(4)	2.161(5)	2.167(4)
R_{Bragg}	4.17	5.62	3.77	5.21	6.36	8.07	8.48	11.61	8.51
$\chi^2(R_{wp}/R_{exp})$	4.445	3.808	3.596	4.962	4.967	5.226	5.229	4.511	2.738

5.3.1.3 Non-ambient x-ray powder diffraction

5.3.1.3.1 High-temperature x-ray powder diffraction To investigate the influence of the doping on ferroelectric phase transition as a function of temperature both high- and low-temperature x-ray powder diffraction scans were recorded. High-temperature x-ray scans were recorded using an Anton Paar furnace in a Panalytical X'Pert Pro MPD diffractometer. Data were collected between 25°C and 325°C with an interval of 10°C for six different compositions from $x = 0.05$ to $x = 0.30$. Figure 5-13 shows the contour plot of the {200} reflection as a function of temperature for different compositions. It is evident that the tetragonal splitting diminishes with increasing temperature and becomes a singlet as a result of the structural phase transition to the cubic phase with space group $Pm\bar{3}m$. Approximate phase transition temperatures for each composition was determined from the contour plot, which suggests that with the increase of NBT content in the sample there is an increase in the phase transition temperature. From the x-ray diffraction data, lattice parameters as a function temperature were obtained which are shown in figure 5-14.

From the lattice parameters obtained for the tetragonal phase at room temperature and the cubic phase at 325 °C, a quantitative strain can be defined along the $< 001 >_c$ and $< 100 >_c$ direction as $(c_t - c_c)/c_c$ and $(a_t - a_c)/a_c$ respectively. These two parameters have been plotted in figure 5-15 as a function of x and it is evident that the strain along the $< 001 >_c$ direction increases with the increase of the doping. In figure 5-16 strain parameters have been re-plotted taking cubic lattice parameters at temperatures just above T_c and the tetragonal lattice parameters at the same reduced temperature (T_c - 100 °C. This also demonstrates similar behaviour as in figure 5-15. The enhancement in the phase transition temperature as a function of x could be as a consequence of the elevated induced strain in the tetragonal structure at ambient temperature.

5.3.1.3.2 Low temperature x-ray powder diffraction Low-temperature x-ray diffraction was performed on NBT-BT ceramics in the temperature range from 25 °C down to −253 °C on a Bruker D5005 diffractometer, which is equipped with a Phenix cryostat (Oxford Cryosystems). Scans were recorded during cooling at intervals of 10 °C.

It is well known that, in addition to the high-temperature ferroelectric phase transition, BT shows two other structural phase transitions at around 5 °C (tetragonal to

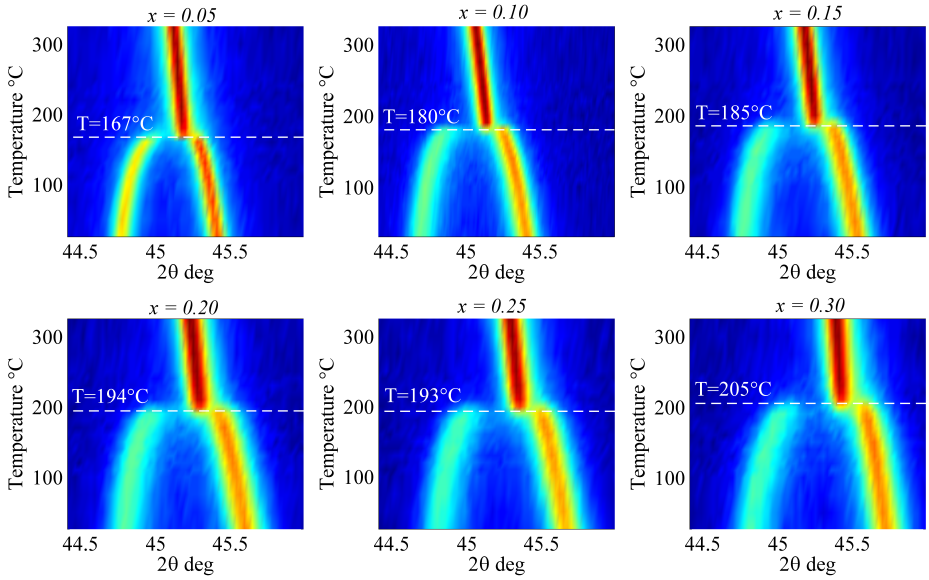

Figure 5-13 Contour plot showing the transformation of the (200) peaks as a function of temperature. The dotted lines represent approximately the phase transition temperatures.

orthorhombic) and −90 °C (orthorhombic to rhombohedral) during cooling. Figure 5-17 shows the contour plot of the diffraction patterns collected for the composition x = 0.05 in the temperature range between 25 °C to −253 °C. Each vertical line represents individual Bragg reflections {hkl} as a function of temperature which remain unaltered throughout the temperature range investigated. Therefore it provides no evidence for any structural phase transition on the given temperature range. It appears that this is also due to the local strains generated by the doping and has been predicted theoretically by Zhong et al. [33] for undoped BT.

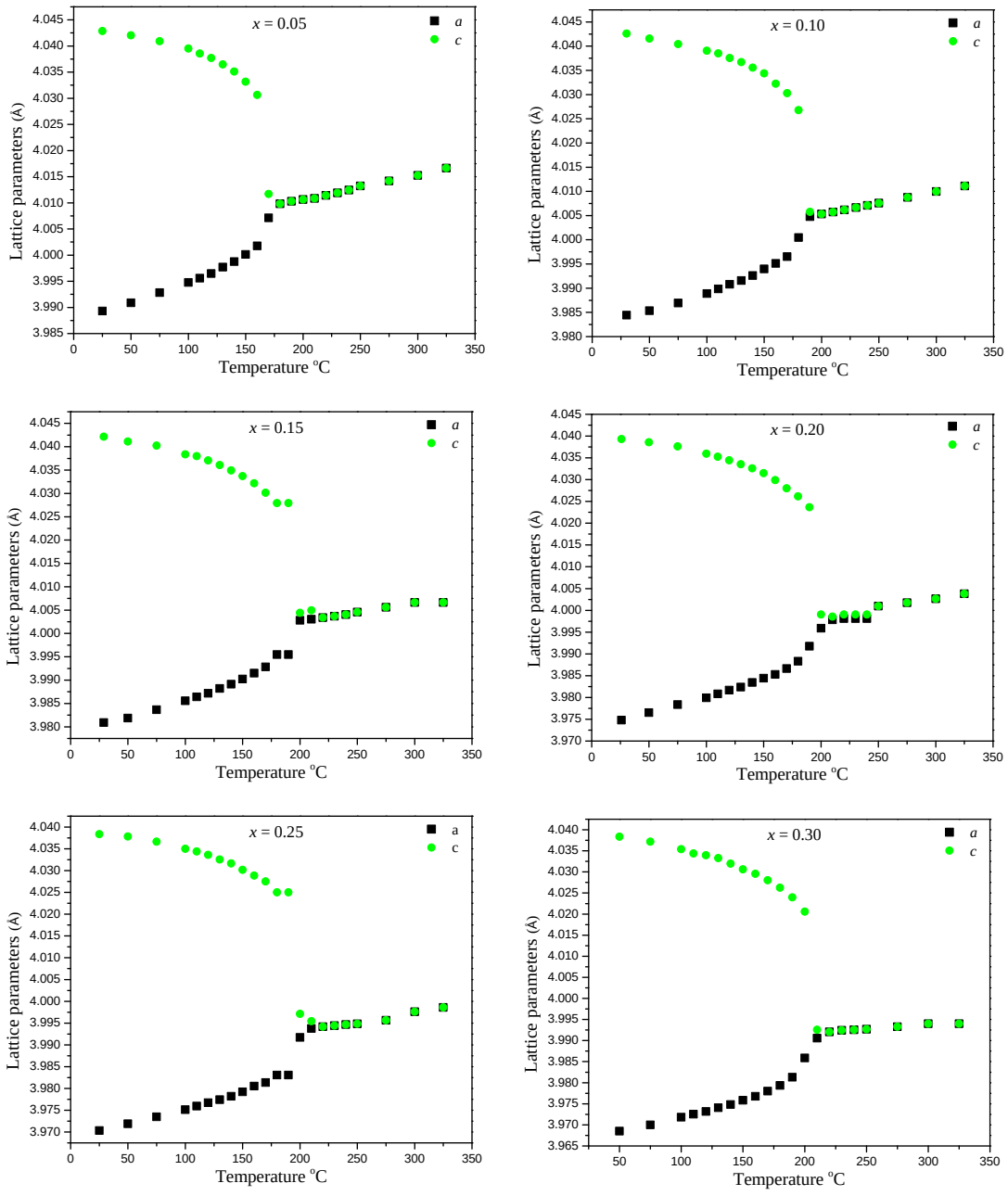

Figure 5-14 Lattice parameters as a function temperature obtained from the high-temperature x-ray diffraction patterns for compositions $x \leq 0.30$.

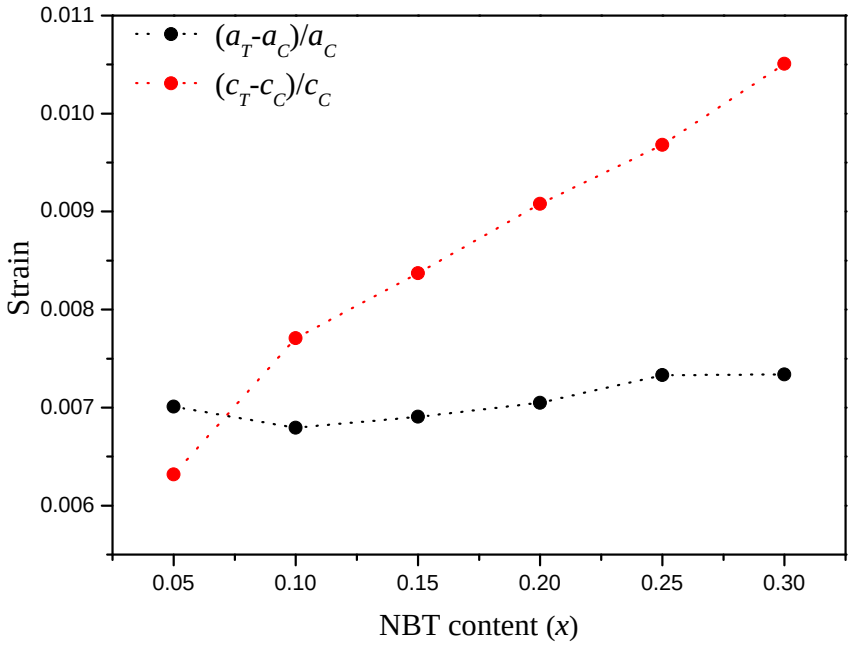

Figure 5-15 Variation of strain along c-axis and a axis of the tetragonal unit cell as a function of composition. Cubic lattice parameters are taken at 325 °C and tetragonal lattice parameters are taken at 25 °C. Error bars are too small too be visible.

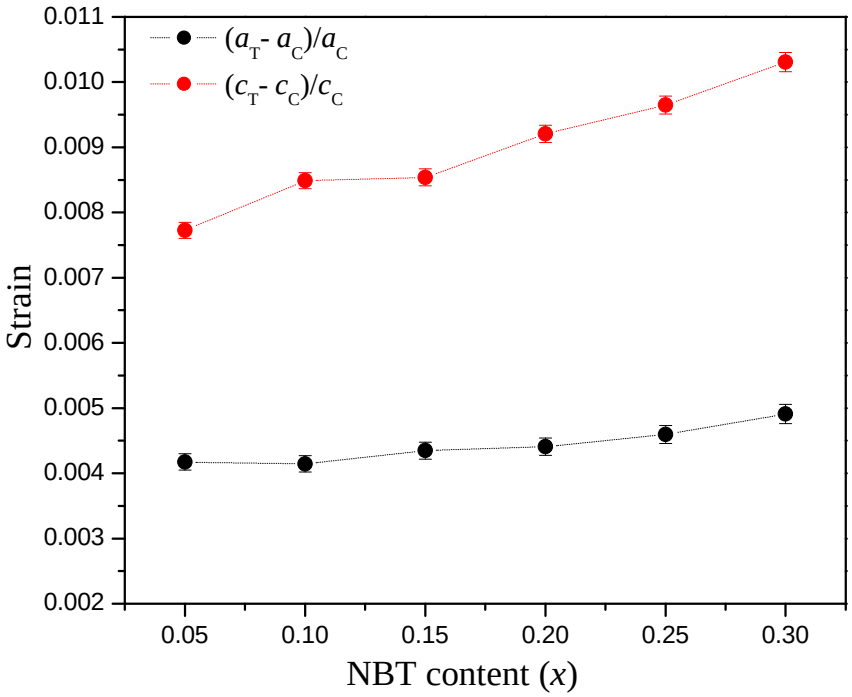

Figure 5-16 Re-plotting of the strain using the cubic parameters from just above T_c and the teragonal parameters at the same reduced temperature (T_c - 100 °C). Errors are larger here because of uncertainties in T_c and hence in the lattice parameters around T_c.

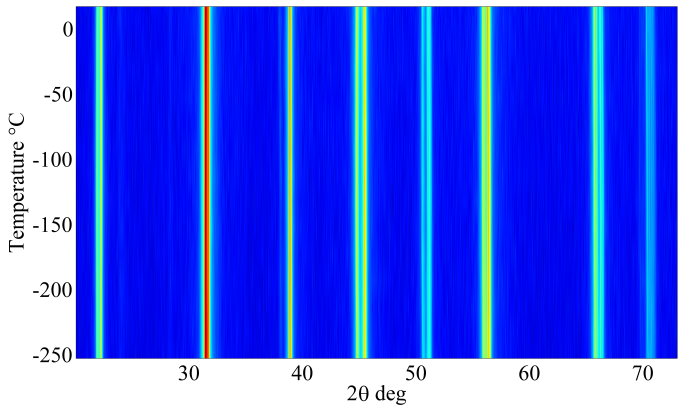

Figure 5-17 Contour plot of the low temperature diffraction scans for x = 0.05 providing no evidence of structural phase transition in the given range of temperature.

5.3.2 Dielectric properties

The temperature- and frequency-dependence of the dielectric permittivity were investigated for eight different compositions of NBT-BT ceramics between x = 0.05 and 0.30. The real and the imaginary parts of the dielectric permittivity ($\varepsilon = \varepsilon' + i\varepsilon''$) were calculated from the capacitance (C) and the conductance (G) data respectively, employing the following formulas assuming a parallel plate capacitor model:

$$\varepsilon' = Cd/\varepsilon_0 D \tag{5-3}$$

$$\varepsilon'' = Gd/\omega\varepsilon_0 D \tag{5-4}$$

where C = capacitance, G = conductance, d = sample thickness, D = area of the electrode, $\omega = 2\pi\times$frequency and ε_0 is the free space permittivity.

Figure 5-18 shows the temperature-dependence of ε' and ε'' for the NBT-BT ceramics with compositions $x \leq 0.30$, for which formation of a single perovskite phase was confirmed from the x-ray diffraction, at three different frequencies: 50 kHz, 100 kHz and 150 kHz. Figure 5-19 demonstrates the variation in ε' and ε'' as a function of temperature for x = 0.35 and 0.40 for which evidence of the existence of other undesired phases along with the primary phase was seen from the diffraction results. The central peak observed for each composition defines the ferroelectric (non-centrosymmetric space group: $P4mm$) to paraelectric phase (centrosymmetric space group: $Pm\bar{3}m$) transition. It is evident that the doping has primarily resulted in shifting the peak-

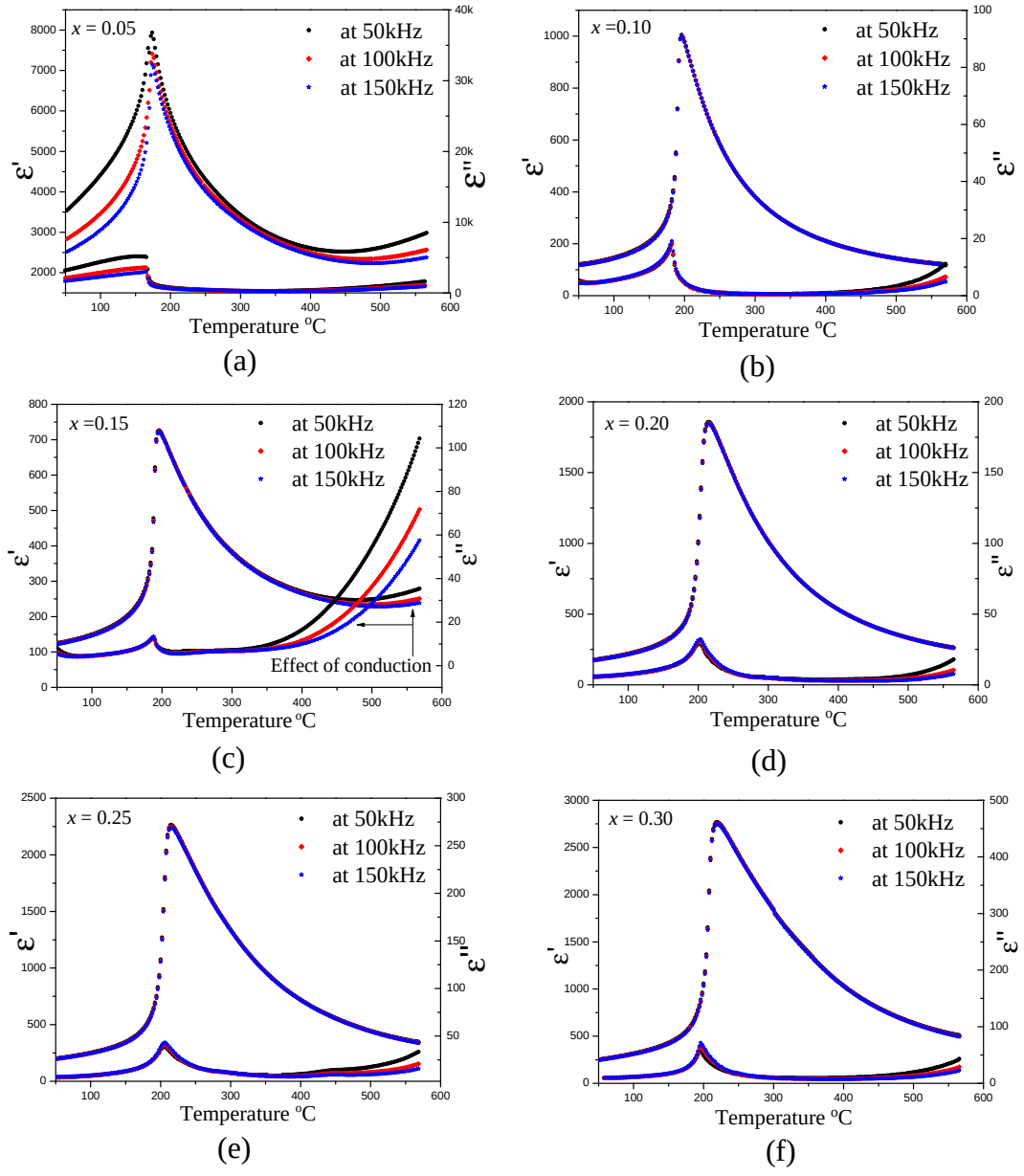

Figure 5-18 Temperature-dependent ε' and ε'' of NBT-BT ceramics for different composition at frequencies 50 kHz, 100 kHz and 150 kHz.

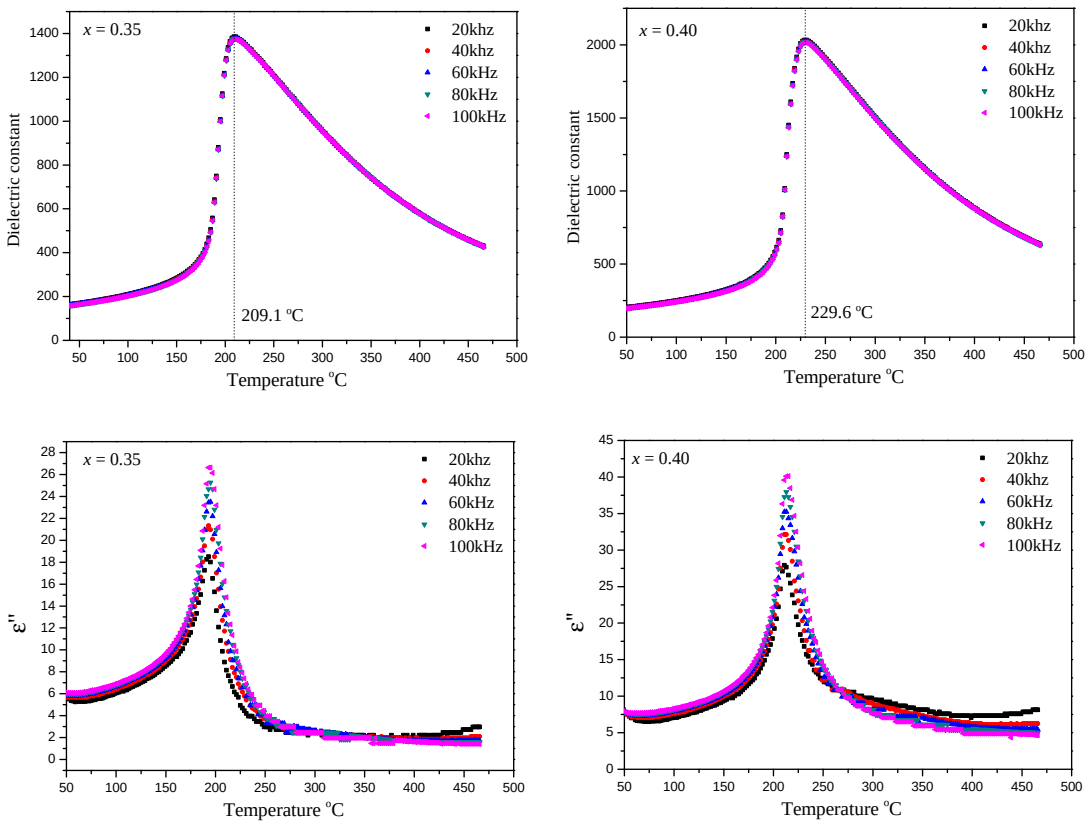

Figure 5-19 Temperature-dependent ε' and ε'' of NBT-BT ceramics for compositions x = 0.35 and 0.40.

temperatures (T_m) to higher temperature and secondly in broadening the ε'-T peaks with the increase of the doping content. Enhancement of transition temperatures is an unusual event in substitutional-type BT-based solid solutions and the only exception reported is where Ba was partially substituted by Pb [34]. The broadening can occur as a consequence of the compositional fluctuations which can give rise a distribution of T_c instead of a sharp Curie point.

The physical properties of $PbTiO_3$ differ from $BaTiO_3$ as a consequence of the covalent nature of the Pb-O bonding [35] whereas Ba-O bonding is purely ionic [36]. From theoretical studies [37] it was predicted the Bi should mimic Pb because of the presence of its stereo-chemically active lone pair electrons. Therefore, it is likely that the Bi-O bond induces a different component of polarization in the structure because of its possible covalent nature which could basically lead the ferroelectric transition temperatures to higher values. Also, doping of different atoms in BT causes local distortion and strain in the structure and these could be responsible for the enhancement of the

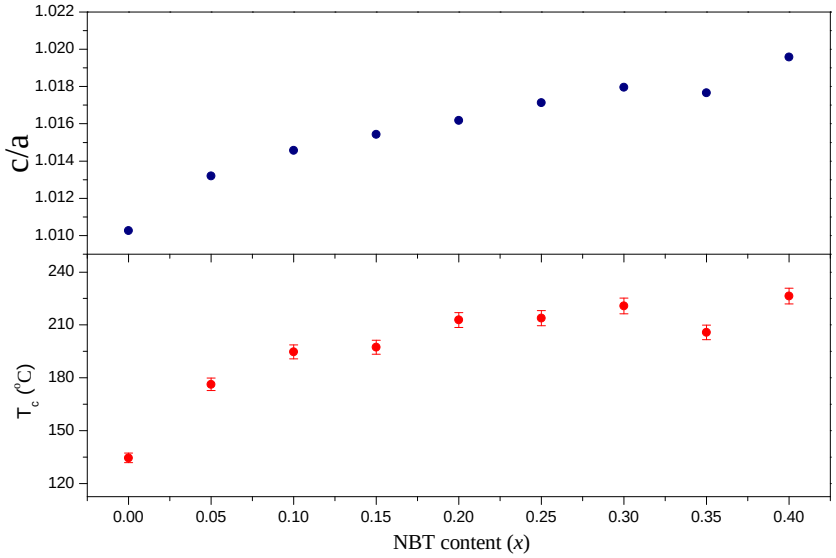

Figure 5-20 Tetragonality and T_c as a function of x demonstrate a linear correlation between these two parameters.

transition temperature together with the broadening of the ε' - T peak resulting from the strain induced relaxation of the polarization near the transition temperature. However, an apparent linear correlation between the tetragonal axial ratio and the T_c can be seen from fig 5-20. This linear correlation can be expected from the relation between the polarization and the temperature [$P \sim (T\text{-}T_c)^{\gamma}$], if similar correspondence between tetragonality and polarization is assumed.

It is further interesting to see the that there is hardly any frequency dispersion of the ε' observed in the frequency range of 50 kHz to 150 kHz for the samples where x is between 0.10 and 0.30. The data points for these ceramics at the three different frequencies are exactly on the top of each other and this makes NBT-BT ceramics distinguishable from typical compositionally disordered systems like relaxors [38–40] and doped quantum paraelectrics [41–43] which demonstrate strong frequency dispersion in dielectric constant in the frequency range of 0.1 kHz to 1 MHz. However, the sample with x = 0.05 has demonstrated relaxation before the ferroelectric phase transition along with large values of ε'', suggesting huge dielectric loss, in comparison with other compositions. This could be an effect of the conduction because of the presence of mobile charge carriers which essentially reduce the resistivity of the bulk ceramics. For the samples x = 0.35 and 0.40, a high frequency dispersion in the ε'' suggests the presence

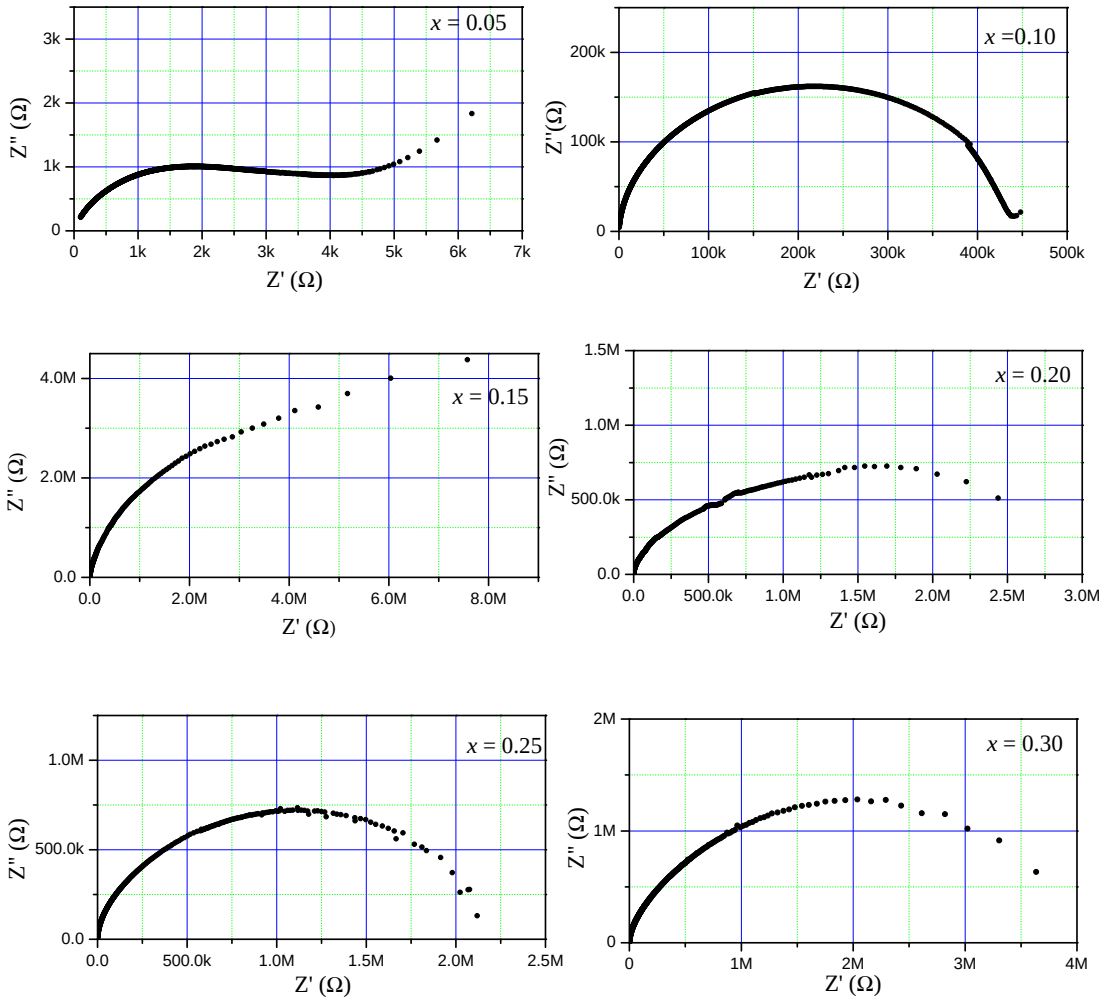

Figure 5-21 Cole-Cole plot for the NBT-BT ceramics suggesting the existence of a single relaxation process for all the composition except for x = 0.05 and 0.15.

of typical leakage current in the ceramics.

An estimate of the impedance was made for the samples with x = 0.05 and x = 0.10 (figure 5-21) using the following formulas:

$$Z' = G/(G^2 + \omega^2 C^2) \tag{5-5}$$

$$Z'' = \omega C/(G^2 + \omega^2 C^2) \tag{5-6}$$

Figure 5-21 shows the Z″ vs. Z′ plots which are commonly known as Cole-Cole plots and a single semicircle suggests the existence of a single relaxation process in the frequency-window at room-temperature. However distorted semicircles were seen for x = 0.05 and 0.15, suggesting again the presence of conduction in the samples [44].

The fall of the dielectric constant after the transition temperature in a ferroelectric

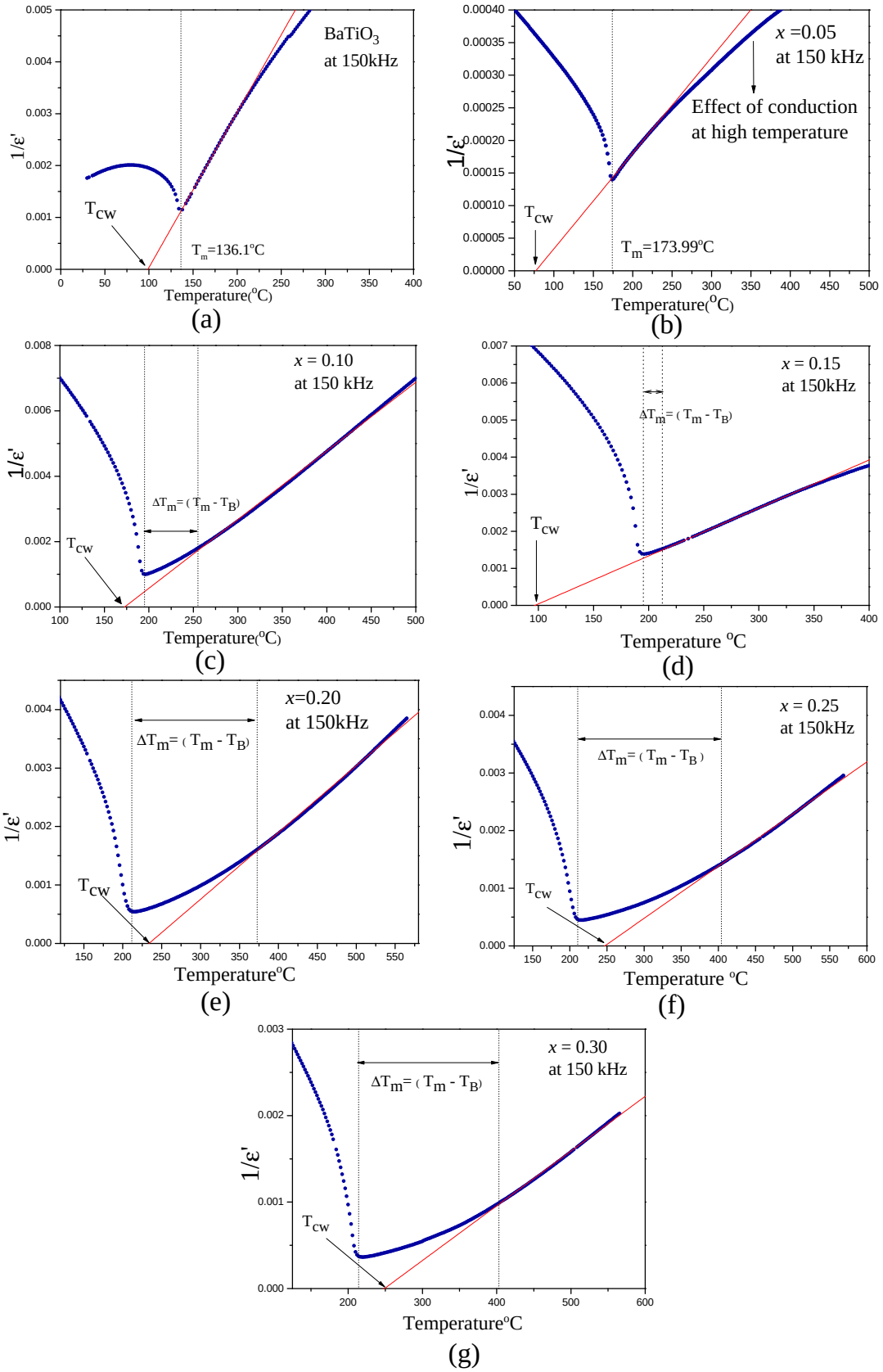

Figure 5-22 $1/\varepsilon'$ vs. temperature plot showing the deviation from classical Curie-Weiss behaviour with increasing x.

material generally follows the Curie-Weiss law:

$$\varepsilon' = C/(T - T_{CW}) \tag{5-7}$$

where C is the Curie-Weiss constant, and T_{CW} is called the Curie-Weiss temperature and generally refers to the ferroelectric transition temperature. To demonstrate the behaviour of the NBT-BT ceramics the reciprocal of ε' as a function of temperature at a constant frequency of 150 kHz has been plotted in figure 5-22 for different compositions. A relatively higher frequency was chosen to eliminate any parasitic contribution such as interfacial capacitance to the dielectric constant, which normally occurs at lower frequencies. The linear relationship between $1/\varepsilon'$ and temperature is valid for x = 0.0 and 0.05, however, the deviation from the Curie-Weiss law is evident for rest of the samples where $0.10 \leq x \leq 0.30$. The data where T >> T_m were fitted with a straight line and the Curie-Weiss temperature (T_{CW}) was estimated from the extrapolation of the fitted line. T_B refers approximately to the temperature below which $1/\varepsilon$ does not follow the temperature linearly. For relaxor ferroelectrics such as $PbMn_{1/3}Nb_{2/3}O_3$, T_B is commonly known as the Burns temperature and it is regarded as a signature of the crossover between soft-mode and order-disorder dynamics [45]. T_m is the temperature where the dielectric maximum occurs and ΔT_m, defined as T_m-T_B, is a measure of the extent of the deviation. It is evident from figure 5-22 that ΔT_m is zero for x = 0.0 and 0.05, confirming the validity of the Curie-Weiss law; however, ΔT_m is non-zero for $x \geq 0.10$ and it increases with the increase in NBT doping. This suggests the appearance of a kind of relaxation near the phase transition temperature upon doping which is responsible for flattening out the ε' - T peaks and the departure from classical Curie-Weiss behaviour. It is also evident that, as a consequence of the peak-broadening, T_{CW} becomes greater than T_m for the samples at x = 0.20, 0.25 and 0.30. For a typical first-order displacive type phase transition, this is incomprehensible. Theoretically for BT, T_{CW} is lower than T_m by about 8 - 10 °C [46].

Figure 5-23 demonstrates the variation of the difference between T_m and T_{CW} as a function of x. A crossover from a positive difference to a negative difference can be seen approximately at x = 0.19, suggesting a crossover from a first-order to a second-order phase transition.

Chemical substitution in the structure can be considered as a chemical analogue of pressure and the manner in which the phase transitions are modified can be compared

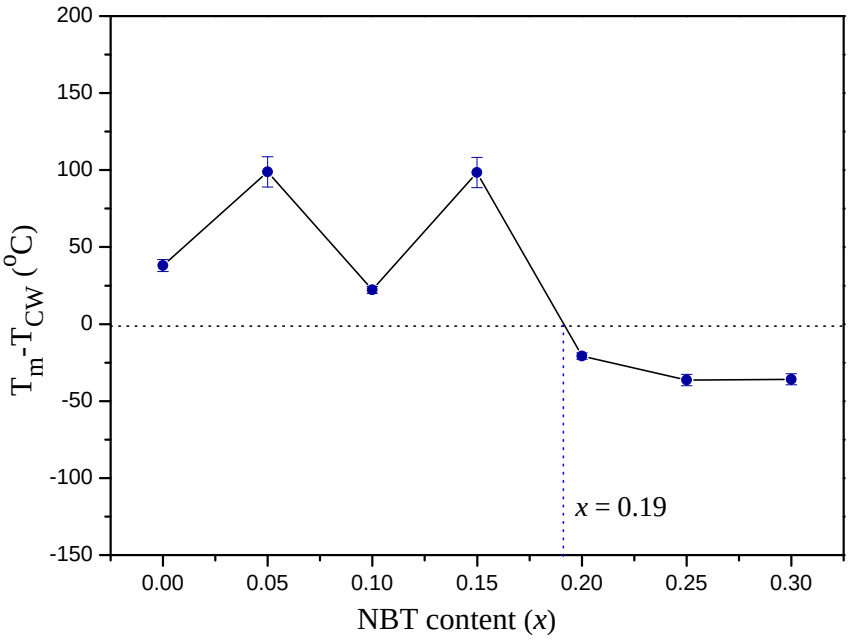

Figure 5-23 The variation of (T_m-T_{CW}) as a function of x. The crossover from positive difference to negative difference occurs at around x = 0.19

instructively with hydrostatic pressure. The dielectric properties of BT under high-pressure were studied by Samara [47] and Ishidate et al. [48] and both suggested the existence of a critical pressure between 4 - 8 GPa where the first-order type phase transition transforms into a second-order one. In addition, an elastic anomaly in BT under high pressure was reported [49] near the ferroelectric phase transition temperature, also suggesting a crossover from first-order to second-order behaviour. To find out more about the character of phase transition as a function of doping concentration, $\delta\varepsilon'/\delta$T vs. T has been plotted in figure 5-24 for different x. Since ε' is directly proportional to the order parameter polarization(P), the sudden inflection of ε' near T = T $_m$ provides a definitive signature of first-order behaviour for x = 0.0 and 0.05. However, as the x increases, the sudden inflection becomes more gradual suggesting a change from the first-order behaviour.

To model the temperature-dependence of the dielectric constant after the ferroelectric phase transition, a phenomenological modified Curie-Weiss law [50] was tested:

$$1/\varepsilon' - 1/\varepsilon'_m = (T - T_m)^\gamma / C \tag{5-8}$$

where, T_m is the temperature at dielectric maximum and ε'_m is the value of the ε' at T_m. γ is considered as a quantitative measure of diffuseness of the ferroelectric phase

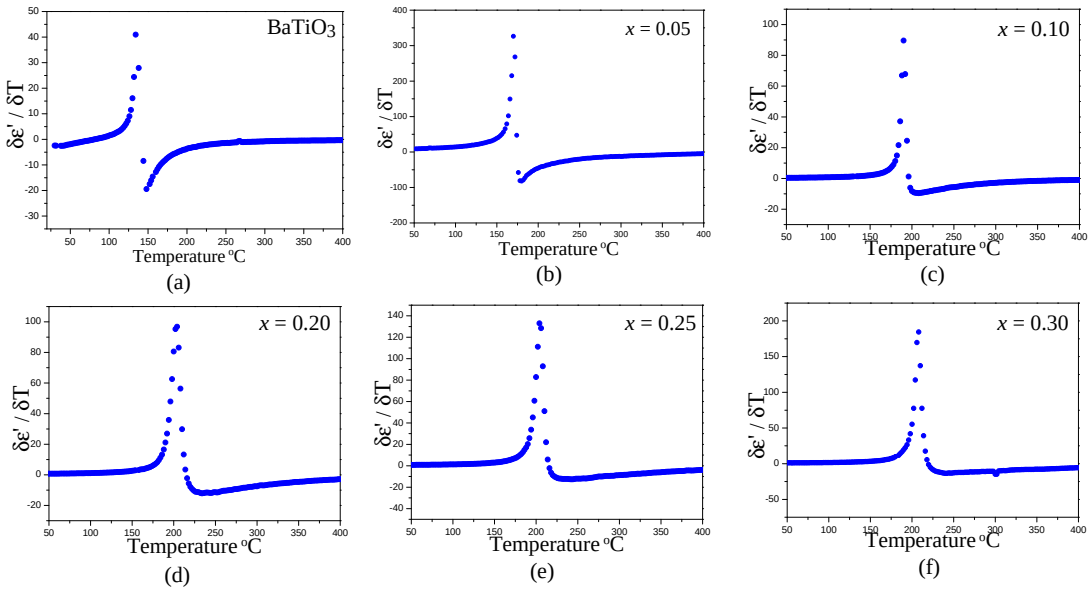

Figure 5-24 The variation of $\delta\varepsilon'/\delta T$ as a function of temperature for different compositions showing that the first-order behaviour of BT is gradually changing with x.

transition and it lies between 1 and 2. γ is 1.0 for normal ferroelectrics whereas γ is equal to 2 for ideal relaxor materials. In figure 5-25 $\log(1/\varepsilon' - 1/\varepsilon'_m)$ vs $\log(T - T_m)$ has been plotted for different values of x. The data were fitted with a straight line and the values of γ and log(C) were obtained from the slope and the intercept of the line, respectively. The values of γ and log(C) obtained from the fitting for different compositions are listed in Table 5-2. For BT, γ has turned out as 1.0 and the maximum value of γ was noted ~1.45 for $x = 0.30$. The values of γ and log(C) obtained from the fit are found to be independent of frequency, although they are sensitive to the range of the data chosen for the fitting. It should also be mentioned that for $x = 0.25$ and 0.30, the linear fit is not satisfactory near the phase transition temperature which suggests that the mechanism responsible for the diffuse phase transition in typical relaxor materials may not be the same for NBT-BT ceramics.

5.4 Discussions

The structure and the dielectric properties of xNBT - $(1 - x)$BT ceramics have been studied for $x \leq 0.40$ since this section of the phase diagram has not been studied in

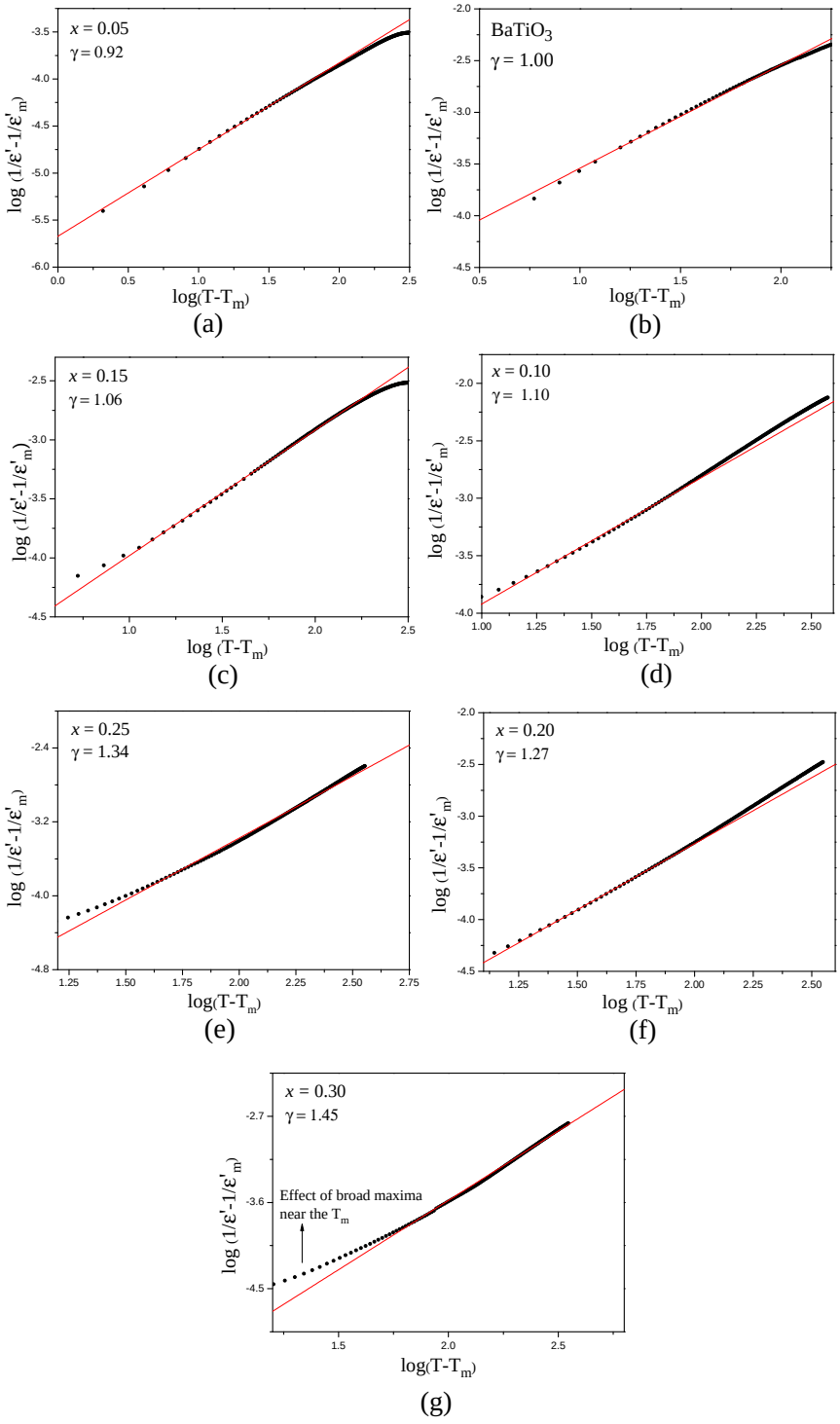

Figure 5-25 Fitting of the modified Curie-Weiss law in the paraelectric phases of NBT-BT ceramics.

Table 5-2 Parameters obtained from the fitting of the dielectric data of the NBT-BT ceramics as a function of composition.

Composition	$x = 0.0$	$x = 0.05$	$x = 0.10$	$x = 0.15$	$x = 0.20$	$x = 0.25$	$x = 0.30$
T_m(°C)	136.1	173.9	194.1	194.7	212.0	210.4	214.0
T_{CW}(°C)	98.1	75.1	171.8	96.31	232.8	246.3	249.9
ΔT_m(°C)	0.0	0.0	60.8	17.3	160.8	194.0	188.6
log(C)	4.54(1)	5.671(7)	5.02(2)	5.043(9)	5.82(1)	6.06(1)	6.47(1)
γ	1.001(7)	0.921(5)	1.10(1)	1.063(5)	1.277(4)	1.341(7)	1.448(6)

detail previously. To date, BT has been studied in many systems where either the A or B sites of the perovskite or both were substituted by isovalent or anisovalent ions. A few common substituents are Sr, Bi, La for the Ba and Zr, Sn, Ta, Nb for the Ti and in all these situations, there are tetragonal to pseudocubic phase transitions upon doping accompanied by a rapid decrease in the Curie temperature [51]. Therefore the enhancement in the tetragonality and increase in the Curie temperature in NBT-BT ceramics is an unusual phenomenon in binary lead-free BT-based solid solutions. Structural details including atomic co-ordinates and bond-lengths obtained from the Rietveld refinements suggest that an increase in tetragonality is not always accompanied by an increase in the polarity of the crystal structure.

xNBT-(1 − x)BT ceramics where $x \leq 0.30$ show dielectric properties and phase transition characteristics that are distinct from other more conventional BT-derived solid solutions assuming that there is no major effect from porosity in the samples. Non-ambient x-ray diffraction results have revealed that two out of three structural phase transitions as a function of temperature in BT are suppressed leaving only a single ferroelectric to paraelectric transition in all the doped samples. However, an increase in the ferroelectric transition temperature as a function of doping has been noted from both high-temperature diffraction and dielectric measurements. The temperature dependence of the dielectric constant has also demonstrated frequency-independent broad maxima near the transition temperatures, which suggests that the relaxation of the polarization is not the result of chemical inhomogeneities or polar nano-regions; rather it is strongly coupled with the strain induced by the doping. This has also caused negative values of $(T_m - T_{CW})$ for the samples with $x > 0.20$, which cannot be explained within the framework of Landau-Devonshire theory. The Curie constant (C) obtained from the fitting of the modified Curie-Weiss law is of the order of 10^5 to 10^6, which indicates

that the mechanism of the phase transition is not going towards the order-disorder type as a function of doping, as for order-disorder type phase transitions C is typically $\sim 10^2$ - 10^3 [52].

References

[1] L. Zhou, P. M. Vilarinho, and J. L. Bapista, J. Am. Ceram. Soc. **82**, 1064 (1999).

[2] F. Bahri, A. Simon, H. Khemakhem, and J. Ravez, Phys. Stat. Sol. **184**, 459 (2001).

[3] G. A. Smolenskii, V. A. Isupov, A. I. Agranovskaya, and N. N. Krainik, Sov.Phys.Solid State (Eng.Transl.) **2**, 2651 (1961).

[4] S. B. Vakhrushev, V. A. Isupov, B. E. Kvyatkovsky, N. M. Okuneva, I. P. Pronin, G. A. Smolensky, and P. P. Syrnikov, Ferroelectrics **63**, 153 (1985).

[5] G. O. Jones and P. A. Thomas, Acta Cryst. B **58**, 168 (2002).

[6] P. A. Thomas, S. Trujillo, M. Boudard, S. Gorfman, and J. Kreisel, Solid State Sci **12**, 311 (2010).

[7] K. Roleder, J. Suchanicz, and A. Kania, Ferroelectrics **89**, 1 (1989).

[8] I. G. Siny, T. A. Smirnova, and T. V. Kruzina, Ferroelectrics **124**, 207 (1991).

[9] C. S. Tu, I. G. Siny, and V. H. Schmidt, Ferroelectrics **152**, 403 (1994).

[10] J. Suchanicz, A. Jezowski, and R. Poprawski, Phys. Status Solidi a **169**, 209 (1998).

[11] M. Geday, J. Kreisel, A. M. Glazer, and K. Roleder, J. Appl. Crystallogr. **33**, 909 (2000).

[12] G. O. Jones and P. A. Thomas, Acta Cryst. B **55**, 426 (2000).

[13] M. Zeng, S. W. Or, and H. Chan, J. Appl. Phys. **107**, 043513 (2010).

[14] J. Yao, W. Ge, L. Luo, J. Li, D. Viehland, and H. Luo, Appl. Phys. Lett. **96**, 222905 (2010).

[15] V. A. Isupov, Ferroelectrics **315**, 123 (2005).

[16] K. Roleder, I. Franke1, A. M. Glazer, P. A. Thomas, S. Miga, and J. Suchanicz, J. Phys.: Condens. Matter **14**, 5399 (2002).

[17] T. Takenaka, H. Nagata, and Y. Hiruma, Jpn. J. Appl. Phys. **47**, 3787 (2008).

[18] T. Takenaka, K. Maruyama, and K. Sakata, Jpn. J. Appl. Phys. **30**, 2236 (1991).

[19] M. Chen, Q. Xu, B. H. Kim, B. K. Ahn, J. H. Ko, W. J. Kang, and O. J. Nam, J. Eur. Ceram. Soc **28**, 843 (2008).

[20] C. Xu, D. Lin, and K. W. Kwok, Solid State Sci. **10**, 934 (2008).

[21] D. Zhou, H. Li, S. Gong, Y. Hu, and K. Han, J. Am. Ceram. Soc. **91**, 2792 (2008).

[22] B. J. Chu, D. R. Chen, G. R. Li, and Q. R. Yin, J. Eur. Ceram. Soc. **22**, 2115 (2002).

[23] T. Oh and M. H. Kim, Mater. Sci. Eng. B **132**, 239 (2006).

[24] J. R. Gomah-Pettry, S. Said, P. Marchet, and J. P. Mercurio, J. Eur. Ceram. Soc. **24**, 1165 (2004).

[25] E. Dulkin, E. Mojaev, M. Roth, S. Greicius, and T. Granzow, Appl. Phys. Lett. **92**, 012904 (2008).

[26] L. Gao, Y. Huang, Y. Hu, and H. Du, Ceram. Int. **33**, 1041 (2007).

[27] J. Suchanicz, J. Kusz, H. Bohm, H. Duda, J. P.Mercurio, and K. Konieczny, J. Eur. Ceram. Soc. **23**, 1559 (2003).

[28] Y. F. Qu, D. Shan, and J. J. Song, Mater. Sci. Eng. B **121**, 148 (2005).

[29] Y. S. Sung, J. M. Kim, J. H. Cho, T. K. Song, M. H. Kim, and T. G. Park, Appl. Phys. Lett. **96**, 202901 (2010).

[30] A. Coelho, *Topas-academic v4.1*, `http://www.topas-academic.net/` (2007).

[31] G. H. Kwel, A. C. lawson, S. J. L. Billinge, and S. W. Cheong, J. Phys. Chem. **97**, 2368 (1993).

[32] H. Yokota, N. Zhang, A. E. Taylor, P. A. Thomas, and A. M. Glazer, Phys. Rev. B **80**, 104109 (2009).

[33] W. Zhong, D. Vanderbilt, and K. M. Rabe, Phys. Rev. Lett. **73**, 1861 (1994).

[34] G. Shirane and K. Suzuki, J. Phys. Soc. Japan **6**, 274 (1951).

[35] Y. Kuroiwa, S. Aoyagi, A. Sawada, J. Harada, E. Nishibori, M. Takata, and M. Sakata, Phys. Rev. Lett. **87**, 217601 (2001).

[36] R. E. Cohen, Nature **358**, 136 (1992).

[37] P. Baettig, C. F. Schelle, R. LeSar, U. V. Waghmare, and N. A. Spaldin, Chem. Mater. **17**, 1376 (2005).

[38] R. E. Cohen, Nature **441**, 941 (2006).

[39] A. A. Bokov and Z. G. Ye, J. Mater. Sci. **41**, 31 (2006).

[40] W. Kleeman, J. Mater. Sci. **41**, 129 (2006).

[41] J. Hemberger, M. Nicklas, R. Viana, P. Lunkenheimer, A. Loidl, and R. Bohmer, J. Phys: Condens. Matter. **8**, 4673 (1996).

[42] J. G. Bednorz and K. A. Müller, Phys. Rev. Lett. **52**, 2289 (1984).

[43] B. E. Vugmeister and M. D. Glinchuk, Rev. Mod. Phys. **62**, 993 (1990).

[44] R. Cohelo, *Physics of Dielectrics* (Elsevier, 1979).

[45] S. A. Prosandeev, S. B. Vakhrushev, N. M. Okuneva, P. A. Markovin, I. P. Raevski, I. N. Zaharchenko, and M. S. Prosandeeva (2005), `arXiv:cond-mat/0506132v1`.

[46] E. Fatuzzo and W. Merz, *Ferroelectricity* (North-Holland, Amsterdam, 1967).

[47] G. A. Samara, Phys. Rev. **151**, 378 (1966).

[48] T. Ishidate, S. Abe, H. Takahashi, and N. Môri, Phys. Rev. Lett. **78**, 2397 (1997).

[49] T. Ishidate and S. Sasaki, Phys. Rev. Lett. **62**, 67 (1989).

[50] K. Uchino and S. Nomura, Ferroelectr. Lett. Sect. **44**, 55 (1982).

[51] F. Jona and G. Shirane, *Ferroelectric crystals* (Pergamon, 1962).

[52] M. E. Lines and A. M. Glass, *Principles and Applications of Ferroelectrics and Related Materials* (Clarendon Press, Oxford, 1979).

Chapter 6

Summary and Suggestions for future study

6.1 Summary

The primary focus of this thesis has been to understand the structural changes occurring because of doping in three different solid solutions. To achieve this goal, both x-ray and neutron powder diffraction experiments were carried out on a series of samples with different compositions. Rietveld refinements were performed against high-resolution neutron powder diffraction data to extract detailed crystallographic information as a function of composition. Structural phase transitions as a function of temperature for different solid solutions were studied through x-ray powder diffraction and complemented by high-temperature dielectric measurements. Important results are summarized below :

- A structural investigation of the solid solution xBiScO$_3$-(1-x)PbTiO$_3$ (BS-PT) was carried out by neutron diffraction using the GEM diffractometer at ISIS facility in Oxford [1]. Atomic positions and thermal displacement parameters were determined by Rietveld refinement for a total of 14 different compositions of BS-PT in the range $0.10 \leq x \leq 0.40$. A gradual structural phase transition from a tetragonal phase with space group $P4mm$ to a rhombohedral phase with space group $R3m$ as a function of x was observed and the phase boundary was identified as a mixture of tetragonal and a monoclinic phases with space groups $P4mm$ and Cm, respectively. Coexistence of tetragonal and monoclinic phases were seen for $0.36 \leq x \leq 0.38$. The structures for $x \geq 0.39$ can be modelled by a single rhombohedral phase with space group $R3m$. However, the refined anisotropic thermal parameters in this region were found to be unrealistic for the average crystal struc-

ture and instead of a rhombohedral phase, a monoclinic phase (*Cm*) is suggested for $x \geq 0.39$. In addition, a possible correlation has been shown between the enhancement of the Curie temperature and the shift of the Ti/Sc ions in the tetragonal region of the phase diagram. Single crystals of BS-PT with composition $x = 0.36$ were grown and studied using high-resolution x-ray diffraction which revealed that the best model to describe the structure consisted of two primitive monoclinic structures [2].

- A lead-free analogue of the BS-PT system was developed by replacing Pb with Ba. The solid solutions of xBiScO$_3$-(1-x)BaTiO$_3$ were prepared through conventional solid-state synthesis route for $x \leq 0.35$. This system demonstrated an extended tetragonal-pseudocubic phase boundary at room temperature in the region $0.05 \leq x \leq 0.20$. Rietveld refinements were performed against the neutron powder diffraction data from the HRPD diffractometer at ISIS to obtain detailed crystallographic information across the phase diagram of this binary system. The best model to describe the phase boundary was found to be a mixture of tetragonal *P*4*mm* and strongly pseudocubic rhombohedral (*R*3*m*) phases [3]. It is evident that the structural phase transition driven by the composition in BS-BT systems is quite different from the BS-PT system. This reinforces the fact that the nature of electronic structure or bonding is crucial. In the case of the PbTiO$_3$-based solid solutions the bonding is dominated by the lone-pair characteristic of PbTiO$_3$. The incorporation of BS in BT also resulted in reducing T_c with increasing x and the low-temperature phase transitions (tetragonal to orthorhombic and orthorhombic to rhombohedral) of BT were suppressed.

- A structural investigation was carried out on another well-known perovskite-based solid solution of xNa$_{1/2}$Bi$_{1/2}$TiO$_3$-(1-x)BaTiO$_3$, where $x \leq 0.40$ [4]. The crystal structure remains tetragonal, with space group *P*4*mm*, for these compositions, but an enhancement of the tetragonality up to 0.9% of the unit cell was observed as a function of doping. Crystallographic details of the structural changes as a function of composition were obtained by performing Rietveld refinement against neutron powder diffraction data collected at HRPD of the ISIS spallation neutron source. Non-ambient x-ray diffraction together with dielectric data as a

function of temperature have demonstrated an enhancement in the ferroelectric to paraelectric transition temperature with the increase of NBT content, including inhibition of the low-temperature phase transitions of $BaTiO_3$. In addition, an anomalous dielectric response has been observed for samples with $x \geq 0.20$ suggesting a crossover from a first-order to a second-order phase transition.

6.2 Future Study

1. Further research is on-going in order to deepen our understanding of the various systems studied in this thesis and beyond. For example, the complex BS-PT system still remains a challenging subject in terms of determining the correct symmetry of the phases as a function of composition. It has been shown that the results from the powder and single crystal diffraction experiments provided different conclusions. Therefore more thorough and comprehensive investigations combining different complementary techniques are required to tackle this issue unambiguously. High quality single crystals are being grown across the entire phase diagram in order to determine the structural evolution as a function of x.

2. So far the study carried out has been confined to determine the structures as a function of composition. It is now therefore important to test these materials for various applications. Currently experiments are being carried out in our partner labs in Virginia Tech to determine piezoeletric figures of merit for the ceramic samples.

3. Similar to BS-BT systems, two new systems with In^{+3} and Yb^{+3} replacing Sc^{+3} have been developed as bulk ceramics and both x-ray and neutron powder diffraction data have been collected to establish the phase diagram of these novel lead-free materials. Neutron powder diffraction data were collected at ILL in France using the high resolution powder diffractometer [5, 6]. However, physical properties of these ceramics are yet to be measured to demonstrate the usefulness of these materials in various applications.

4. We have very recently synthesized solid solutions of $xK_{1/2}Bi_{1/2}TiO_3$ - (1-x)BT (KBT-BT) where $x \leq 0.30$. Figure 6-1 shows the room-temperature x-ray diffrac-

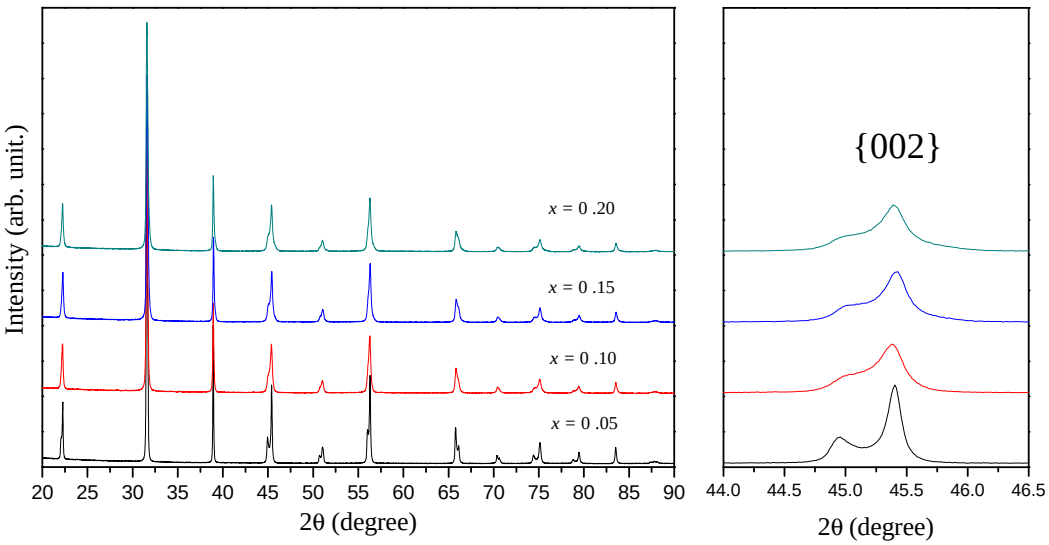

Figure 6-1 Room-temperature x-ray diffraction patterns for *x*KBT-(1-*x*)BT ceramics as a function of composition. Decrease in the separation of {002} peaks suggests the decrease in the tetragonality of the unit cell with increasing *x*.

tion patterns as a function of *x*. It is evident that with increasing KBT content the tetragonality is reduced and this feature is contrary to the effect in the case of the NBT-BT solid solutions. Further investigation is currently underway to determine details of the structural changes as a function of composition.

5. It is also suggested that Raman scattering experiments both at ambient and non-ambient conditions can be performed on the various systems investigated here in order to investigate structural phase transitions as a function of composition, temperature and pressure.

6. Finally, attempts can be made to grow single crystals from the powder samples of different systems investigated and in addition to diffraction experiments, some optical experiments, such as birefringence measurements can be performed on the ferroelectric crystals for domain-imaging and to investigate the ferroelectric phase transition as a function of temperature.

References

[1] K. Datta, D. Walker, and P. A. Thomas, Accepted for publication in Phys. Rev. B (August 2010).

[2] K.Datta, S. Gorfman, and P. A. Thomas, Appl. Phys. Lett. **95**, 251901 (2009).

[3] K. Datta and P. A. Thomas, J. Appl. Phys. **107**, 043516 (2010).

[4] K. Datta, K. Roleder, and P. A. Thomas, J. Appl. Phys. **106**, 123512 (2009).

[5] K.Datta, E. Suard, and P. A. Thomas, Appl. Phys. Lett. **96**, 221902 (2010).

[6] K.Datta, E. Suard, and P. A. Thomas, In preparation. (June 2010).

Appendix A

Publications

One of my publications is attached here, which has not been presented in the thesis.

[1] K.Datta, E. Suard and P. A. Thomas, "Compositionally driven ferroelectric phase transition in x$BiInO_3$-(1-x)$BaTiO_3$: a lead-free perovskite-based piezoelectric material", *Appl. Phys. Lett.* **96**, (2010), 221902.